WARWICK
THE UNIVERSITY OF WARWICK

A Thesis Submitted for the Degree of PhD at the University of Warwick

Permanent WRAP URL:

http://wrap.warwick.ac.uk/162579

Copyright and reuse:
This thesis is made available online and is protected by original copyright.
Please scroll down to view the document itself.
Please refer to the repository record for this item for information to help you to cite it.
Our policy information is available from the repository home page.

For more information, please contact the WRAP Team at: wrap@warwick.ac.uk

warwick.ac.uk/lib-publications

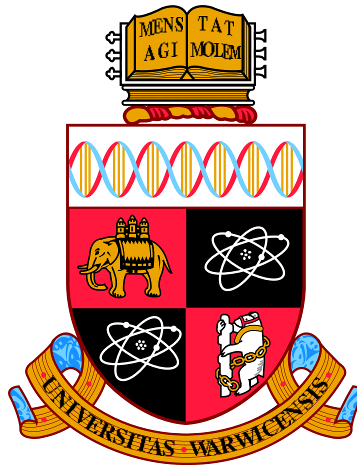

GaN-on-Si Pressure, Flow, and Thermal Conductivity Sensors for Harsh Environments

by

Geraint Rhys Jones

Thesis

Submitted to the University of Warwick

for the degree of

Doctor of Philosophy

School of Engineering

February 2021

Contents

List of Tables v

List of Figures vi

Acknowledgments xiv

Declarations xv

Abstract xvii

Chapter 1 Motivation and Introduction 1

1.1 Introduction 1

1.2 Thesis Outline 4

Chapter 2 Background 6

2.1 Flow Sensors 6

2.1.1 Non-Thermal Flow Sensors 6

2.1.2 Thermal Flow Sensors 10

2.1.3 Current State of the Art 20

2.2 Pressure Sensors 22

2.3 Gallium Nitride 26

2.3.1 AlGaN/GaN Heterostructure 27

2.3.2 The High Electron Mobility Transistor 28
2.3.3 GaN for Harsh Environments 32
2.3.4 GaN Sensors 35
2.3.5 GaN-on-Si as a Sensing Platform 37

Chapter 3 Modelling of GaN Devices and Sensors 41

3.1 Flow Chamber Modelling 41
3.1.1 Theory 42
3.1.2 Modelling 43
3.1.3 Model Outputs 44
3.2 Pressure 47
3.2.1 FEM Model 48
3.2.2 Analytical Model 56
3.2.3 Combined FEM and Analytical Model Results 59
3.3 Conclusion 60

Chapter 4 GaN on Silicon Flow Sensors - Fabrication and Testing 62

4.1 Thermoresistive Flow Sensors 62
4.1.1 Introduction 62
4.1.2 Design & Packaging 63
4.1.3 Experiment 66
4.1.4 Discussion 68
4.1.5 Conclusions 69
4.2 2DEG Flow Sensor 72
4.2.1 Introduction 72
4.2.2 Design 73

4.2.3 Experimental 73
4.2.4 Discussion 78
4.2.5 Conclusions 81
4.3 Comparison between devices 82
4.4 Conclusions 84

Chapter 5 GaN HEMT Pressure Sensor - Fabrication and Testing 85

5.1 Introduction 85
5.2 Design & Packaging 86
5.3 Experimental 88
5.3.1 Discussion 92
5.3.2 Conclusions 100

Chapter 6 Gas Detection with Calorimetric Flow Sensor 101

6.1 Introduction 101
6.2 Design & Fabrication 103
6.3 Automated Testing Station 106
6.3.1 Hardware 106
6.3.2 Control Software 107
6.4 Experimental 109
6.4.1 Data Pre-processing 110
6.4.2 Linear Prediction 110
6.4.3 Artificial Neural Network 112
6.4.4 Post Processing 114
6.5 Discussion 116
6.5.1 Sensor Output & Thermal Conductivity 116

6.5.2 Linear Statistical Model 122
6.5.3 Neural Network 123
6.5.4 Comparison between techniques 126
6.6 Conclusions 127

Chapter 7 Conclusions & Further Work 130

7.1 Summary 130
7.2 Conclusions 133
7.3 Further Work 134

List of Tables

2.1 Physical Properties of Substrates [1] [2] 26

2.2 Workfunctions for Schottky contact metals 30

2.3 Selected GaN sensors from literature 39

2.4 Selected flow sensors from literature 40

3.1 Elastic coefficients of materials in the model [2] 50

3.2 Lattice constants of materials where x is the fraction of Al in the alloy [2]. 58

5.1 HEMT Characterisation tests 90

5.2 Sensitivity and Power Consumption of the ring HEMT pressure sensor at various operational modes. 99

6.1 PLSR result 127

6.2 PCR result 127

6.3 ANN result 127

List of Figures

2.1 This shows the different physical transduction domains that can be used to detect flow [3]. 7

2.2 Some examples on non-thermal flow sensors. (a) Shows a deflecting beam design where the beam is placed in the flow with the lengths parallel to the flow direction. The lift force exerted on the beam causes it to deflect, which is picked up by piezoresistors on the beam [4]; (b) Shows a neuromast design, where the pillar is placed in the flow is used to cause a membrane or cantilever to deflect, which is then picked up by transducers on the structures. This design has less of an impact on the flow itself than the deflecting beam [5]; (c) Shows a shear wall design, where the pressure of the flow on the wall causes the wall to deflect, which is picked up by transducers on the base; (d) Shows an alternative version of the neuromast design, where the cross-section of the pillar is an over rather than a circle. This has the benefit of minimising localised eddies and further turbulence caused by the mast [6]. 8

2.3 Different thermal flow transduction techniques. (a) a single hot-wire configuration, (b) a time of flight, and (c) a calorimetric configuration. 11

2.4 GaN Wurtzite Crystal Structure with Gallium and Nitrogen atoms labelled. 27

2.5 Cross section of a typical AlGaN/GaN HEMT 29

2.6 GaN HEMT fabrication steps (Simplified). (a) Silicon wafer, (b) AlN Seed layer, (c) Graded AlGaN layer, (d) GaN layers, (e) AlGaN layer, (f) GaN cap, (g) Gold metallisation, (h) Passivation and membrane release 33

3.1 Velocity profile of fluid along the centre of the flow channel, i.e. 1 mm from the wall 45

3.2 Cross section of the velocity profile of fluid at the centre of the flow channel, i.e. 10 mm from the end. 46

3.3 Flow velocity at distances away from the sensor. This shows the 3 flow chamber lengths at a constant flow rate of 1 SLPM. 47

3.4 Velocity profile of fluid inside the flow chamber 48

3.5 Simulated simplified GaN stack structure 49

3.6 Membrane displacement at peak load (1 MPa), showing only the simulated quarter. The black wire frame shows the original position of the membrane 52

3.7 Membrane displacement at peak load (1 MPa). This uses symmetry to extrapolate the other 3 quarters not simulated. . . . 52

3.8 Membrane displacement vs applied pressure, showing the maximum displacement at the centre of the membrane, and the average displacement over the membrane taken as the integral of the membrane. 53

3.9 Von Mises stress in the membrane, simulated quarter of the device at peak load (1 MPa). 54

3.10 Membrane stress tensors in the x, y, and z directions vs applied pressure at the point of peak stress (25 µm from the edge). Orientation is shown on fig. 3.9. 55

3.11 Membrane strain in the x, y, and z directions vs applied pressure at the point of peak stress (25 µm from the edge). Orientation is shown on fig. 3.9. 56

3.12 Percentage change in total polarisation at the interface with pressure from 0 to 100 kPa. 60

4.1 Optical Image of the sensor chip, highlighting the main devices; the gold hot-wire, Au/2-Dimensional Electron Gas (2DEG) thermopiles, and mini-HEMT temperature sensors (not discussed in this thesis). 63

4.2 Die cavity in the interface PCB package 64

4.3 The flow channel of the upside-down lid 64

4.4 Packaged device with flow channel lid 65

4.5 Schematic Cross-section of the GaN-on-Si sensor 65

4.6 TCR Extraction (Resistance at hot-chuck temperature) 67

4.7 Heater power vs heater temperature 68

4.8 Gold sensor output operating in a constant current anemometric mode at various temperatures, where the temperature corresponds to constant current values of 87 mA, 95 mA, and 100 mA for zero flow temperatures of 150 °C, 200 °C, and 250 °C. 70

4.9 Gold sensor sensitivity operating in a constant current anemometric mode at various temperatures, where the temperature corresponds to constant current values of 87 mA, 95 mA, and 100 mA for zero flow temperatures of 150 °C, 200 °C, and 250 °C. 71

4.10 Schematic Cross-section of the GaN-on-Si flow sensor with a 2DEG hot-wire. 72

4.11 I-V characteristics of the 2DEG resistor at various chuck temperatures for the released (membrane) device 74

4.12 I-V characteristics of the 2DEG resistor at various chuck temperatures for the unreleased device 75

4.13 2DEG hot-wire resistance vs chuck temperature for the released and unreleased devices 76

4.14 TCR extraction (Resistance at hot-chuck temperature) 76

4.15 Power vs Temperature of the 2DEG hot-wire. Note the self-heating effect causing a fluctuation in the power consumption. 77

4.16 Sensor output vs flow rate up to 4 SLPM at various hot-wire currents. 79

4.17 Sensor sensitivity vs flow rate up to 4 SLPM at various hot-wire currents. 80

4.18 Hot-wire DC power consumption vs sensitivity. 80

4.19 Sensor output vs flow rate up to 1 SLPM at various hot-wire currents. 81

5.1 Top down schematic of the ring HEMT pressure sensor showing dimensions. 87

5.2 Device cross-section with HEMT structure highlighted. 88

5.3 Poor alignment on ring-HEMT device. 89

5.4 Transfer characteristics of the ring HEMT where the shading represents the range of the response of the devices tested. . . . 91

5.5 Output characteristics of the ring HEMT. 91

5.6 Gate Diode I-V characteristics of the ring HEMT where the shading represents the range of the response of the devices tested. 92

5.7 Current vs Pressure where $V_{GS} = 0V$ and V_{DS} set to various levels 93

5.8 Current vs Pressure where V_{DS} =+5V (saturation) and V_{GS} set to different levels 94

5.9 Current vs Pressure where V_{GS} =+1 V and V_{DS} set to different levels 95

5.10 Current vs Pressure where V_{GS} =-1 V and V_{DS} set to different levels 96

5.11 Sensors output peak sensitivity vs DC power consumption . . 97

6.1 Heater DC power consumption vs flow velocity for various gases as per equation 6.1. 103

6.2 Top down schematic view of the sensor die showing the thermopiles and heater structure. 104

6.3 Cross section view of a Au/2DEG thermocouple. 105

6.4 Schematic of the gas rig 107

6.5 Gas Rig GUI for rig controls (Microsoft Edge browser) 108

6.6 Gas Rig GUI for rig data display (Microsoft Edge browser) . . 108

6.7 Figure showing the mean squared error of the neural network versus the epoch number, up to 50,000 114

6.8 Neural Network Diagram with two processing layers 115

6.9 Sensor output voltage vs flow rate at different gas concentrations. (a) is the Hot-Wire output, and (b) and (c) show the upstream and downstream thermopile response (respectively). The fluid is a N_2-H_2 mixture, from 0% H_2 to 100%. 118

6.10 Sensor output voltage vs flow rate at different gas concentrations. (a) is the Hot-Wire output, and (b) and (c) show the upstream and downstream thermopile response (respectively). The fluid is a N_2-H_2 mixture, from 0% H_2 to 100%. 119

6.11 Sensor output voltage vs H_2 concentration (%) at different flow rates. (a) is the Hot-Wire output, and (b) and (c) show the upstream and downstream thermopile response (respectively). The fluid is a N_2-H_2 mixture, from 0% H_2 to 100%. 120

6.12 Sensor output voltage vs flow rate at different gas concentrations. (a) is the Hot-Wire output, and (b) and (c) show the upstream and downstream thermopile response (respectively). The fluid is a N_2-H_2 mixture, from 0% H_2 to 100%. 121

6.13 Sensor response compared with fitted response for both PLSR and PCR analysis for hydrogen concentration. 123

6.14 Sensor predicted flow rate with fitted response for both PLSR and PCR analysis against target flow rate. 124
6.15 Sensor response compared with fitted response from the trained neural network for hydrogen concentration. 125
6.16 Sensor predicted flow rate compared with fitted response from the trained neural network against target flow rate. 126

Acronyms

2DEG 2-Dimensional Electron Gas.

AlGaN/GaN AlGaN/GaN.

AlN Aluminium Nitride.

ANN Artificial Neural Network.

CC Constant Current.

CFD Computational Fluid Dynamics.

CMOS Complementary Metal Oxide Semiconductor.

CR Constant Resistance.

CT Constant Temperature.

CV Constant Voltage.

DRIE Deep Reactive-Ion Etching.

FEM Finite Element Method.

GaN Gallium Nitride.

GaN-on-Si Gallium Nitride on Silicon.

HEMT High-Electron Mobility Transistor.

HFET Hetrojunction Field Effect Transistor.

HVPE Hydride Vapor Phase Epitaxy.

IOT Internet of Things.

MBE Molecular Beam Epitaxy.

MEMS Micro Electromechanical System.

MFC mass flow controller.

MOCVD Metalorganic Chemical Vapour Deposition.

MOSFET Metal Oxide Semiconductor Field Effect Transistor.

MSE Mean Squared Error.

PCA Principal Components Analysis.

PCB Printed Circuit Board.

PCR Principal Components Regression.

PLSR Partial Least Squares Regression.

SiC Silicon Carbide.

SOI Silicon on Insulator.

TCR Temperature Coefficient of Resistivity.

Acknowledgments

I would like to first thank my supervisor Prof. Julian Gardner for his guidance, support, and knowledge throughout the course of this PhD, and for giving me the opportunity to lead the direction of this project. I acknowledge the EPSRC DTP for funding my studentship, and the Innovate UK GaN Sense project for providing devices. I would like to thank Flusso Cambridge Ltd. and specifically Dr Andrea De Luca for the thoughtful discussions and knowledge around all things flow sensors.

As I leave Warwick with my sanity largely intact, I have to thank the people that I have shared this experience with. My colleagues in the MBL past and present, and my *other* colleagues, Akira, the Sam's, Matt, Sarah, Lorenzo, Eleanor, Natalie, Punit, and Amy. Our CDWM experiences were certainly that. And after 8 years at Warwick, I can not leave without acknowledging my team mates at UWRFC and Warwick Snow.

Finally, I would like to thank my family for their support throughout my studies, especially my mother for your wiliness to listen and endless encouragement. Also to my later father, Emyr Wyn Jones, for laying the foundation of my curiosity and determination that I will take through life.

Declarations

This thesis is submitted to the University of Warwick in support of my application for the degree of Doctor of Philosophy. It has been composed by myself and has not been submitted in any previous application for any degree. All work presented was carried out by the author, except where otherwise indicated.

Parts of this work have been included in patent applications, published in the scientific literature and presented at international conferences, as listed below in chronological order.

Journals

Gardner E, Vincent T, **Jones G R**, Gardner J W, Coull J, De Luca A. and Udrea F, 2019, "MEMS Thermal Flow Sensors— An Accuracy Investigation", IEEE Sensors Journal, 19(8), pp.2991-2998.

Jones G R, Gardner J W. 2021, "GaN-on-Si calorimetric thermal-conductivity sensor", MDPI Sensors, (Submitted)

Conference Papers

Jones G R, Vincent T, De Luca A, Longobardi G, Eblabla A, Elgaid K, Wotherspoon T, Birch R, Udrea F, Gardner J W. "GaN-on-Si Thermoresistive

Flow Sensor with Gold Hot-wire", IEEE SENSORS CONFERENCE 2019 Oct 27. IEEE.

Gardner E L, De Luca A, Vincent T, **Jones G R**, Gardner J W, Udrea F. "Thermal Conductivity Sensor with Isolating Membrane Holes", IEEE SENSORS CONFERENCE 2019 Oct 27. IEEE.

Abstract

There is a growing number of applications that demand sensors and devices that can deal with harsh environments, which has led to new materials being used to realise these. One material that has demonstrated promise in high temperature, high radiation, chemically and mechanically harsh environments is Gallium Nitride (GaN). GaN on a silicon platform has advantages over other group III-N materials, in that a variety of Micro Electromechanical System (MEMS) fabrication techniques can be used, and Complementary Metal Oxide Semiconductor (CMOS) circuitry can be monolithically integrated on the same chip. Pressure, flow, and thermal conductivity sensors are of particular interest in harsh environments, and these have been investigated here.

A ring-HEMT pressure sensor is presented, that utilises a High-Electron Mobility Transistor (HEMT) embedded into the edge of a GaN membrane released from a silicon substrate. This device was tested in different bias conditions to find the best operating conditions for high sensitivity and low power consumption. This pressure sensor was modelled mechanically in an Finite Element Method (FEM) package, and the results fed into an analytical model to estimate the change in carrier concentration.

Two flow sensors are presented. The first is a hot-film device using gold metallisation to create a thermoresitive flow sensor. The second uses the 2DEG at an AlGaN/GaN heterojunction as the hot-wire heating element.

This work proved the operation of both sensors at flow rates up to 5 SLPM.

Finally, a thermal conductivity sensor is presented based on the gold hot-film device, using gold/2DEG thermocouples as temperature sensors upstream and downstream of the heating element. Simultaneous measuring of the flow rate and thermal conductivity was achieved using an artificial neural network to discriminate between the two fluid properties. Principal Components Regression (PCR) and Partial Least Squares Regression (PLSR) linear statistical methods were also explored for this discrimination, but with limited success.

Chapter 1

Motivation and Introduction

1.1 Introduction

Sensors are fundamental for providing the interface that gives insight into the physical phenomena that occurs in the real world. As modern data processing has grown, and with the advent of concepts such as the Internet of Things (IOT) and big data, there has been a growing demand for sensors that can measure more things, and in different ways. The global sensor market is expected to grow to $287 billion by 2025 [7]. Silicon is the market leader in terms of materials when it comes to MEMS, however, as demand grows for sensors to be placed in harsher environments, new materials need to be developed to overcome the physical limitations of the material. This has led to new materials and processes being developed that can survive these harshening conditions.

Harsh environments cover 4 physical domains, that can be identified as: (i) thermal - extreme temperatures (high or low); (ii) mechanical - forces such as vibration, pressure and shock; (iii) chemical - where materials can react to each-other, often presenting as corrosion; and (iv) electromagnetic - which covers environments with a presence of extreme radiation and electrostatic discharge. While the maximum and minimum extremes of each domain is important, consideration must be given to other effects, such as the cycling between highs and lows of each domain, not necessarily between the maximum

and minimum condition.

Silicon is the dominant material for the fabrication of MEMS devices, owing to its relatively low price, established processing techniques, and the ease of integrating the MEMS with other circuitry. However, devices made in a standard CMOS process have a thermal limit of around 200 °C, due to intrinsic carrier generation at elevated temperatures. Work has been done into using Silicon on Insulator (SOI) to fabricate devices that are more robust in harsh environments. SOI retains many of the benefits of standard CMOS in addition to being more robust against radiation and temperature. But even SOI can not be operated in environments above 300 °C [8]. It is for this reason that research into new materials for sensors is being carried out.

Of particular interest are wide band-gap semi conductors such as Silicon Carbide (SiC), Aluminium Nitride (AlN) and Gallium Nitride (GaN) [8, 9, 10]. This property is of benefit in creating devices for harsh environments, as it means the devices are less prone to many of the negative affects that silicon is, such as any unwanted optical or thermal generation of charge carriers. Equation 1.1 shows the relationship between intrinsic carrier concentration (n_i) of a material and its band gap, E_g , where N_C and N_V are the effective density of states for the conduction and valence band, k_B is Boltzmann's constant, and T is temperature. As an example, the intrinsic carrier concentration at room temperature of GaN is of the order of $10^{-10}/\text{cm}^3$ while for silicon it is $10^{10}/\text{cm}^3$ [8]. GaN is of particular interest, as in addition to the wide band gap, the strong bonding between the Ga and N atoms leads to superior performance in terms of mechanical, thermal, and chemical stability. This coupled with pronounced pyro and piezoelectric properties, and a high acoustic velocity enabling high bandwidths, makes GaN a desirable material for creating sensors. GaN heterostructures, using the appropriate alloy, have been shown to operate up to 1000 °C [11, 12].

$$n_i = \sqrt{N_C N_V} e^{-E_g/2k_B T} \tag{1.1}$$

Radiation effects semiconductor in a number of ways, but the property that is important for being resistant to ionizing radiation is the mean dis-

placement energy, that is, the energy required to displace an atom from the lattice. For GaN, this energy is much higher than that of silicon [13, 14, 15], making GaN a viable material for high radiation environments. All of these properties, coupled with the ability to monolithically integrate GaN sensors with silicon drive circuitry, give rise to several harsh environment applications for GaN sensors of various types [16]. Two of which are detailed below:

Automotive Systems

Modern motor vehicles are sensor dense and a major consumer of devices. The industry as a whole makes up 20% of the sensors market share [17], and includes devices to monitor a range of things such as engine temperature, battery performance, oil levels, and crash detection. While the current market for traditional combustion engines are on their way out, new challenges and opportunities arise in their electric and automated replacements [18].

Space Exploration

Sensors used in space exploration will need to survive all of the definitions of high environment. Devices will need to survive the harsh mechanical conditions, such as extreme vibrations, of launch; the extreme radiation exposure during interplanetary space flight. In this context, both the long-term background exposure and short high intensity bursts should be considered; Temperature variations are well known in space. Consideration needs to be given to the final destination, temperatures on the moon, for example, can vary from $127\,^{\circ}\mathrm{C}$ to $-272\,^{\circ}\mathrm{C}$ during the day and night cycle. Or on the surface of Venus, where there is a substantial investment in research by various space agencies, the temperature is $460\,^{\circ}\mathrm{C}$ and the pressure around $9\,\mathrm{MPa}$ [19, 20].

Radiation exposure is a big problem in space. This impacts electronics by changing the characteristics of the response of the device. For example, the threshold voltage of standard SOI CMOS Metal Oxide Semiconductor Field Effect Transistor (MOSFET) change by around a third after a total ionizing dose (TID) of 3.6kGy . By contrast, the change in an AlGaN/GaN HEMT is negligible after a dose of 2Mrad (20kGy) [21, 22].

As many aspects of space are being commercialised, the number of space craft to incorporate these devices are increasing. In addition to the angle of space research, there is also a need for sensors for structural health monitoring and failure detection, as reusable space craft become more mainstream. These sensors will have to be long-lasting and reliable in addition to just surviving the conditions, without the draw backs of extra shielding and refrigeration [23].

1.2 Thesis Outline

This thesis presents research into the use of Gallium Nitride on Silicon (GaN-on-Si) as a material for 3 types of sensing; pressure, flow, and thermal conductivity.

Chapter 2 presents the background to the research and includes a discussion of some of the fundamental theory behind this work and a review of the literature in the field.

Chapter 3 discusses the work done on modelling the sensors presented in this thesis. Electrothermal and electromechanical modelling was done using the FEM in the COMSOL Multiphysics 5.4 package. The modelling was done to predict the pressure sensor behaviour in response to pressure, and to simulate the fluid effects in designing test flow chambers.

Chapter 4 presents the GaN-on-Si flow sensor. There are two sensors discussed here. One uses a gold hot-wire and the other leverages the properties of the 2DEG to implement a thermoresistive hot-wire anemometer. Details of the fabrication, testing, and performance of these devices are presented.

Chapter 5 discusses a GaN-on-Si pressure sensor. This uses the strong piezoelectric properties of the AlGaN/GaN (AlGaN/GaN) to transduce pressure from the mechanical deformation of a membrane to the carrier concentration in the 2DEG channel of a ring-HEMT device. Details of the fabrication, testing, and performance of the device is discussed.

Chapter 6 uses the flow sensor presented in chapter 4 in a calorimetric configuration in order to simultaneously measure flow and thermal conductiv-

ity of that fluid. This chapter also compares different statistical techniques to predict each of these fluid properties.

Chapter 7 completes the thesis with some concluding remarks of the research presented and details some considerations for further work.

Chapter 2

Background

This chapter presents the background to this research, which includes a comprehensive literature review of the field and a detailed explanation of the theory behind GaN-on-Si devices, flow, pressure, and thermal conductivity sensors.

2.1 Flow Sensors

MEMS sensors have grown as the dominant form of sensors in recent years. MEMS devices can be made smaller, consume less power, and cheaper to fabricate than macro sized devices. Flow sensors can detect certain characteristics in the flow of a fluid, such as the wall shear stress and flow velocity. Various physical principles can be used to measure flow, including optical, thermodynamic, acoustic, hydrodynamic, mechanical. Figure 2.1 details these. Thermal flow sensors are by far the most popular type.

2.1.1 Non-Thermal Flow Sensors

There are a few common MEMS implementations for non-thermal flow sensors. As the work in this thesis focuses on thermal flow sensors, the discussion in this sub section provides only a high level overview of the sensing mechanisms available.

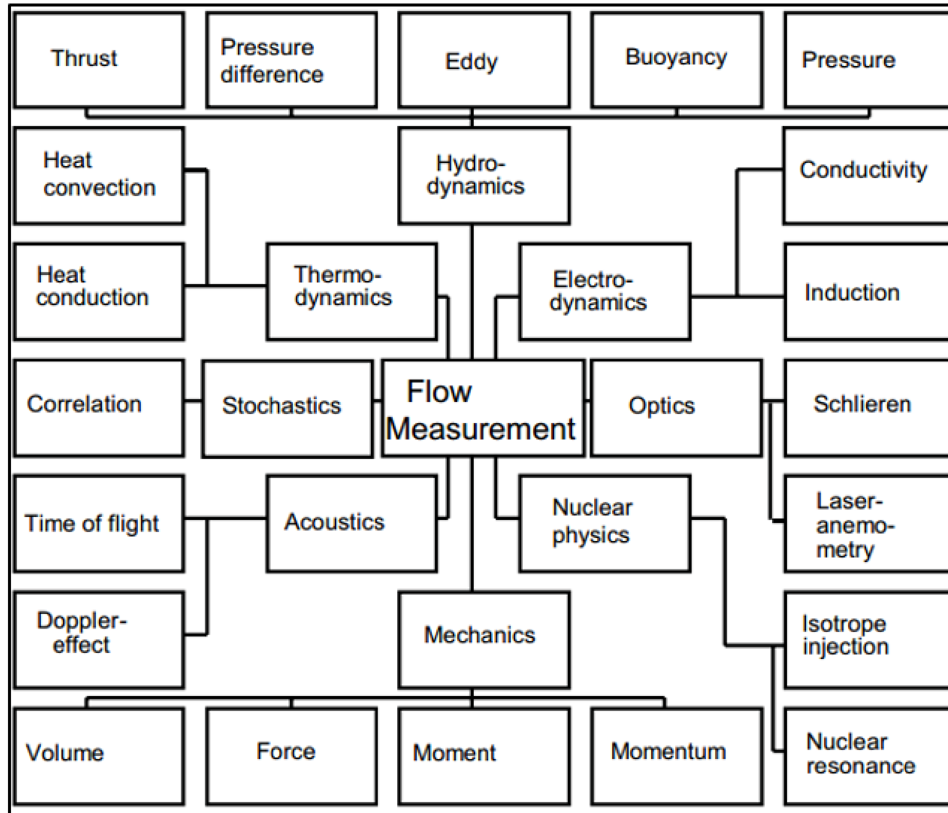

Figure 2.1: This shows the different physical transduction domains that can be used to detect flow [3].

Piezoresistive

Piezoresistive flow sensors rely on the piezoresistive effect to detect flow, where the resistivity of a material changes in relation to induced strain. Broadly, there are either diaphragm type or cantilever type of sensors. The cantilever type generally consist of a flat plate, that is placed directly into the flow. As fluid passes the beam, it causes deflection, which is then picked up by a piezoresistor implanted on the beam. These sensors detect flow velocity directly.

Early devices were based off a cantilever design placed into the flow, and due to the effects of lift (or drag depending on direction), the cantilever would deflect. This deflection would cause a strain on or near the clamped part of the beam, where a piezoresistor would be located to detect this strain [4, 24].

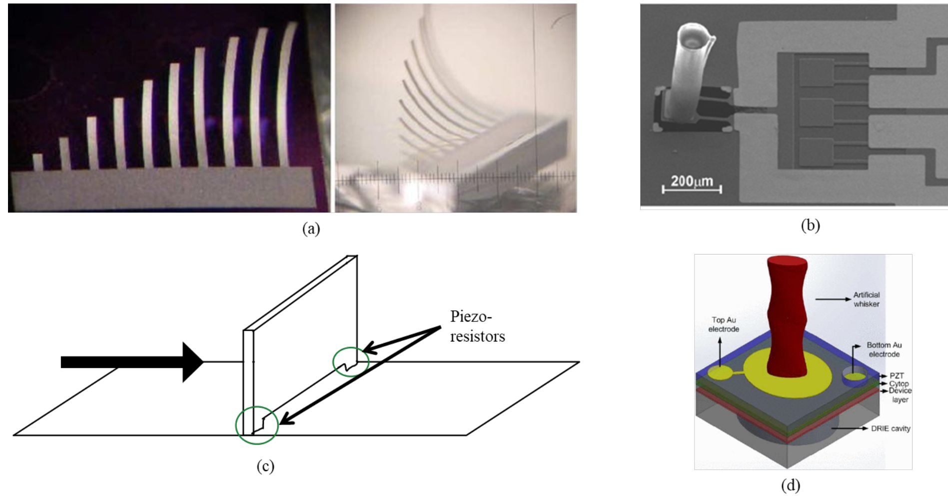

Figure 2.2: Some examples on non-thermal flow sensors. (a) Shows a deflecting beam design where the beam is placed in the flow with the lengths parallel to the flow direction. The lift force exerted on the beam causes it to deflect, which is picked up by piezoresistors on the beam [4]; (b) Shows a neuromast design, where the pillar is placed in the flow is used to cause a membrane or cantilever to deflect, which is then picked up by transducers on the structures. This design has less of an impact on the flow itself than the deflecting beam [5]; (c) Shows a shear wall design, where the pressure of the flow on the wall causes the wall to deflect, which is picked up by transducers on the base; (d) Shows an alternative version of the neuromast design, where the cross-section of the pillar is an over rather than a circle. This has the benefit of minimising localised eddies and further turbulence caused by the mast [6].

Silicon can be used as the material for a cantilever beam, which can be fabricated using a range of micro fabrication processes. Poly silicon resistors can be implanted directly on to the beam at the point of maximum strain (near to base of the beam), as in figure 2.2 (a) or (c). Variations on this design include several beams connected in a strain gauge configuration, which enables higher sensitivity and directional discrimination.

Materials used in these devices have ranged from micromachined silicon to SOI based, where a silicon piezoresistor is sandwiched between the SOI wafers [25]. Shapes have also been experimented with. Work by Tian [26] showed a numerical model of an inverted trapezoidal membrane cantilever beam array, which found the design to be more sensitive due to the additional stress generated by the shape [27].

Sensitivity and detection range of these devices vary from 20-40 m/s and 0.204x10^{-3} V/(m/s) [27] to low velocity devices at 0.01-0.03 m/s such as in [28].

Modern developments in piezoresistive flow sensors have led to the creation of diaphragm based devices. These take their inspiration from nature with a neuromast design, fabricated on top of a membrane. This is similar to the lateral line of the blind cavefish, which most designs are based off [5, 29, 30, 31]. This is shown in figure 2.2 (b) The high aspect ratio of the mast compared to the diaphragm it is attached to causes the pressure field of the surrounding fluid to defect the mast which in turn twists and bends the membrane, causing strain that is normally picked up by a whetstone bridge circuit. The types of materials used vary, but silicon is the most common for the membrane, due it its ease of fabrication, sensitivity, and cost [32, 33].

Piezoelectric flow sensors are popular due to their good intrinsic characteristics such as, bio compatibility, small size, low power and low cost [32, 34]. These devices do have their draw backs though, especially in the harsh environment range. Piezoresistivity is heavily influenced by temperature and humidity, where moisture absorption over time can lead to a degradation in performance and longevity of the device [35, 36].

Generally, the detection range is in the low flow velocity range (<10m/s), although as high as 30 m/s was reported by [37]. Sensitivity can be as high as 6.98 V/(m/s) as in [30], but are generally to the order of x10^{-3} [29, 38, 39].

Piezoelectric

Piezoelectricity is the phenomena by where materials develop an electric charge in response to mechanical loads, and the opposite, where the material deforms due to an applied electric charge [40]. Two such materials often used in piezoelectric flow sensors are the polymer, polyvinylidene fluoride (PVDF) and a ceramic such as lead zirconate titanate (PZT) [41, 42]. The down side of these devices is their large internal resistances, which increase power consumption.

A key benefit of these types of devices are that they are self-powered and do not need an external supply, and they are physically flexible. This has

made them useful in many remote applications [43], such as in [44] where a sensor was developed to monitor the blood flow rate during surgery.

As with the piezoresistive devices, there are several examples of devices taking inspiration from nature. [45] developed a sensor based on a hair cell, whose operation is similar to the neuromast but with the piezoelectric effect acting as the transduction mechanism rather than the piezoresistive. A further development of this concept is the artificial micro-whisker inspired by the whiskers of seals. Rather than the straight pillar design, with a circular cross section found in most neuromast devices, this has an elliptical cross section and wave-profiles along the axes. These have the benefit of minimising vortex induced vibrations, and hence reducing the noise present in the sensor [6, 46].

Other types of flow sensors exist, such as capacitive devices, ultrasonic, turbine style, to name a few. By far the most common type are the thermal flow sensors, which is the principal of operation of around 51.2% of all flow sensors reported in literature [47]. The thermal flow sensors are the focus of the work presented in this thesis.

2.1.2 Thermal Flow Sensors

This work focuses on flow sensors operating based on thermodynamic principles. Thermodynamic flow sensors are used in MEMS due to the ease in which they can be fabricated and the relatively low power consumption and ease of operation. Thermal flow sensors can be categorised further as hot film, hot wire, calorimetric and time-of-flight sensors. Depending on the configuration of the sensors, it is possible to detect other fluidic properties, such as its thermal conductivity or thermal diffusivity.

Thermal Flow Sensor Configurations

Thermal flow sensors use the ability of the fluid to affect thermal phenomenon by way of heat transfer, specifically, forced convection. Modern thermal flow sensors utilise heating elements, such as a resistive heater, and/or temperature sensors to measure the change in flow.

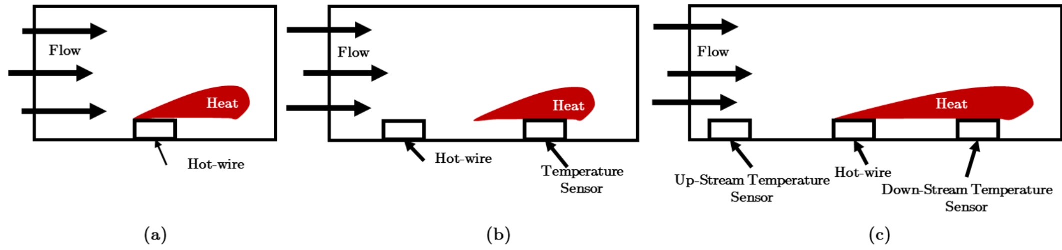

Figure 2.3: Different thermal flow transduction techniques. (a) a single hot-wire configuration, (b) a time of flight, and (c) a calorimetric configuration.

There are three main forms of thermal flow sensors; anemometric, calorimetric, and time-of-flight. These are shown in figure 2.3. These can be implemented on the wall of a fluid channel or placed directly into the fluid stream. Under ideal conditions, the heat transfer should only occur into the fluid. In reality, this is not the case, with several sources of heat loss, mainly into the chip substrate. This lowers the sensitivity and increases the power consumption of the device.

Hot-Wire/Hot-film anemometer

The Hot-Wire anemometer flow sensor is the simplest type of flow sensor to implement, shown in figure 2.3 (a). Here a hot-wire or hot-film transfers heat from a heated element into a cooler flowing fluid via forced convection. As fluid flow increases past the sensor, the convective heat loss increases, thus cooling the heater. This cooling can then be measured via a second temperature sensor, or by using the heater itself. In the case of using a resistive heater as the sensing element, the change in resistance due to the cooling is measured. The difference between a hot-film and hot-wire device is that the heating element in a hot-wire device is offset from the rest of the device, whereas for a hot-film device, the heating element is attached to the device substrate. Normally, this substrate would be etched away to release a membrane, in order to thermally isolate the heater from a large metal heat-sink.

King's Law can be used for hot-wire anemometry characterisation as it describes heat transfer from a cylinder in terms of the resulting voltage difference. King's Law can be expressed as:

$$\Delta V(v) = a + bv^n \tag{2.1}$$

where: ΔV is the flow induced voltage difference, v is the flow velocity, and a, b, n are constants based on the geometry and characteristics of the fluid.

The relationship between resistance and temperature is given by:

$$R(T) = R(T_0)[1 + \alpha(T - T_0)] \tag{2.2}$$

where $R(T)$ is the resistance at temperature T and α is the Temperature Coefficient of Resistivity (TCR) of the material. In essence, the higher the TCR the more sensitive the material is to temperature. The TCR can be determined experimentally by:

$$a_R = \frac{R(T) - R(T_0)}{R(T_0)} = \alpha(T - T_0) \tag{2.3}$$

$$\frac{\Delta R}{R} = \alpha \Delta T \tag{2.4}$$

where a_R is the resistance overheat ratio, which is determined by measuring the change in resistance of the material at two different temperatures. The TCR can be negative or positive where a negative value indicates a decrease in resistance with heating, such is the case with polysilicon. Both TCR and resistivity need to be considered when choosing the hot-wire material, since a high absolute resistance will experience a greater change in resistance for detection, which may be easier to detect by the drive circuitry, but will also increase the biasing voltage of the device, making it unsuitable for low voltage applications in some situations.

Typical materials for a hot-wire include gold, aluminium, tungsten, and polysilicon. Polysilicon is a popular choice in silicon or CMOS MEMS implementations. Polysilicon has the advantage that it is already a fabrication layer for most CMOS processes, and that its electrothermal properties can be fine-tuned using a combination of doping and grain size. The literature shows that the TCR of polysilicon can vary from -250x10^{-4} %/K to 10x10^{-4} %/K [48].

Choice of material is limited even further based on application. If we consider platinum, which has a relatively low TCR (39.2 x10^{-4} %/K), but is proven to be biocompatible, and so is a popular choice for biomedical applications. Additionally, packaging and fabrication process should be considered for materials. CMOS compatible materials have an advantage due to their ability to be used in MEMS applications [49, 50, 51, 52, 53].

Several operational modes are possible for hot-wire and hot-film sensors. The three most common are Constant Current (CC), where the current is set and change in voltage due to flow is monitored, Constant Voltage (CV), where the change in current is monitored and voltage kept constant, and Constant Temperature (CT) or Constant Resistance (CR), this is where feedback circuitry is used to keep the hot-wire/hot-film temperature constant and the power required to maintain this temperature is monitored. This is the most complex to implement but offers improved sensitivity and frequency response compared to the others.

Calorimetric

A calorimetric flow sensor uses an upstream and downstream temperature sensor in conjunction with a heating element to detect the temperature profile of the fluid around the heater. This type of sensor can also detect the asymmetry of the flow due to direction and so can be used to detect flow direction. At zero flow, the temperature profile is symmetric around the heater.

The heat transfer into the fluid depends on the thermal properties of said fluid. In the case of a calorimetric flow sensor, the difference in thermal properties (heat capacity and thermal conductivity) will change the temperature profile of the fluid independently from the heat transfer due to the shear stress. It is therefore necessary to calibrate the device depending on the fluid.

Section 2.1.2 discusses in more detail the different transduction principals for the flow sensors. The choice of temperature sensor can again impact on performance.

Time of Flight

A time-of-flight uses the transit time of a thermal pulse to measure the flow rate. A temperature sensor downstream of a heater is used to detect an increase in fluid temperature after the heater is pulsed. The difference in time between the heater pulse and the detection of the increase in temperature is related back to the flow rate. This type of implementation, like the calorimetric device, this too can detect flow direction and fluid properties.

Equation 2.5 shows an approximation for the thermal distribution of the pulse. This includes several factors that need to be accounted for in designing a time-of-flight sensor [54].

$$T(x,t) = \frac{q_0}{4\pi k t} e^{[-\frac{(x-vt)^2}{4at}]} \tag{2.5}$$

T represents the temperature distribution at time t at the distance, x from the heater. q_0 is the strength of the pulse signal, v the average flow velocity, and then the thermal properties, thermal conductivity k, and thermal diffusivity a. All of these factors affect the temperature profile of the fluid and the magnitude of heat detected by the downstream sensor.

The final average flow velocity can be calculated by equation 2.6 [54], where d is the distance from the heater to the downstream sensor. Driving the time of flight sensor requires some circuitry to synchronise the pulse with the time measurement. This type of sensor relies on good thermal isolation, less the heater pulse directly heats the downstream sensor through the substrate. Because of this, it is better that the temperature sensor is thermally unconnected to the heater. The devices presented in this thesis include the downstream temperature sensors on the same membrane as the heater and so the lack of proper thermal isolation makes it difficult to implement this configuration.

$$v = \frac{d}{t} \tag{2.6}$$

Shear Stress Sensor

While the devices outlined above can be implemented in flow, that is the heater and sensing devices are suspended in the fluid flow itself, they can also be implemented on the wall of a flow channel, as is done in this work. In this implementation, the main transduction mechanism is the shear stress induced on a solid boundary by a fluid flowing. In the case of this work, a section of the boundary wall is replaced by a sensor. In fluids, the no-slip condition dictates that the flow velocity at the boundary is zero and at some height away from the boundary the flow velocity equals the mean fluid flow velocity. This region where there is a velocity gradient from the zero at the wall to the mean flow velocity is named the boundary layer.

The shear stress at the wall (on the sensor) is given by [54, 55]:

$$\tau_w = \tau(y = 0) = \mu \frac{\delta u}{\delta y} \tag{2.7}$$

where τ is the shear stress, y the height above the boundary, u is the flow velocity, and μ is the dynamic viscosity of the fluid. Taken together, the term $\frac{\delta u}{\delta y}$ represents the velocity profile in the boundary layer.

The wall shear stress determines the rate of heat transfer from the hot-wire into the fluid flow. The mean wall shear stress can be measured using the modified version of King's Law:

$$p = I^2 R = [A(\rho \tau_w^{1/3} + B)]\Delta T \tag{2.8}$$

where P is the electrical power consumption of the sensor, I the current, R the resistance of the hot-wire on the hot-film, ΔT is the average temperature difference from a reference temperature. A is a constant that is determined from the fluid properties, where:

$$A \propto \frac{C_p^{1/3} k_T^{2/3}}{\mu^{1/3}} \tag{2.9}$$

B represents the heat transfer into the substrate under zero flow con-

ditions. Note that the relationship in equation 2.9 does not always hold true for micro-machined thermal flow sensors. In this case, the root of μ may not be cubic, in which case it needs to be determined experimentally.

Thermal Flow Sensor Transduction Principles

There are several different transduction principals that can be used to detect flow, depending on materials and transduction principals. The most basic are thermoresistive sensors that use resistors as the sensing elements. Thermoelectric utilise the thermoelectric effect to detect temperature change using thermopile sensors. Thermoelectric sensing uses active devices such as transistors and diodes. It is also possible to create devices that use the change in resonant frequency within mechanical structures to detect temperature changes.

Thermoresistive

These devices work by transferring heat away from a resistive heater. As the heater cools the change in current or voltage due to the change in resistance can be calibrated to the fluid flow. These are the most common type of thermal flow sensors due to the ease in which they can be fabricated and operated [54].

Thermoelectric

These devices use thermopiles made up of several thermocouples as the temperature sensing element which are located upstream and downstream of a heating element in the calorimetric sensors. These devices allow the measurement of the temperature profile of the fluid. The fabrication is more complicated than the thermoresistive devices, but thermocouples can be fabricated in many processes, including a standard CMOS processes. This enables these devices to be fabricated at a low cost and at scale. The sensitivity of the devices is based on the Seebeck effect [54].

The output voltage of a thermocouple is given by:

$$V_{ab} = \alpha_{ab}\Delta T_{hot-cold} = (\alpha_a - \alpha_b)(T_{hot} - T_{cold}) \tag{2.10}$$

where α is the Seebeck coefficients of the junction materials, a and b, and T is the temperature at the junctions. When a number of thermocouples are connected in series, the output due to thermal change increases thus making them more sensitive. This does come with a penalty in increased Johnson noise, and the thermal conduction between junctions increases, hence lowering the difference in temperature between the hot and cold junctions. Thus, the number of thermocouples needs to be optimised to account for these penalties when increasing sensitivity.

Thermopile materials can be of any combination. A figure of merit for a particular combination can be used to optimise the materials used. Semiconductor materials, such as polysilicon or doped silicon are good candidates for creating thermopiles due to their higher Seebeck coefficients which lead to more sensitive devices. But with the semiconductor devices, the Seebeck coefficients are also temperature dependent, which adds an additional layer of complexity to the operation [54].

In the same way as the doped silicon areas are used in silicon based devices, some work has been done into GaN based thermocouples, where the 2DEG region is used on of the junction materials.

Thermoelectronic

Thermoelectronic sensors utilise the temperature dependence on the junctions of transistors and diodes to detect temperature. In silicon devices, the I-V relationship of the p-n homojunction is described by [54]:

$$I = I_r(e^{V/nV_T} - 1) \tag{2.11}$$

where I_r is the reverse saturation current, n is the ideality factor of the material and V_T is the thermal energy (kT/q). Alternatively, the diode can be biased in a constant current configuration, where the change in voltage with

respect to the change in temperature becomes:

$$\frac{dV}{dT} = \frac{V - (V_g + mnV_T)}{T} \tag{2.12}$$

Equation 2.12 includes the forbidden-gap energy (V_g) and the factor m, where m is 1.5 for Si. Empirically, $\frac{dV}{dT}$ can be determined to be $-2.5\,\mathrm{mV/K}$ for silicon.

Thermoelectronic flow sensors have the benefit that they can be fabricated in a CMOS compatible process, and can therefore be integrated with drive circuitry on the same package. It is also possible to fabricate devices, such as was done by De Luca [56], where diodes are placed underneath the hot-wire in an anemometric configuration to do the temperature measurement. This resulted in a more sensitive device compared to operating in just thermoresistive mode with a singular heater and sensor.

Fluid Mechanic Principals of Thermal Flow Sensors

The main mechanism of heat transfer is forced convection. In addition to the flow rate, the heat transfer from the thermal flow sensor into the fluid is also based on other factors including the thermal conductivity (k), specific heat capacity (c_p), density (ρ), viscosity (μ), and the geometry of sensing package influences some of these. The geometry specifically influences the flow regime of the fluid. That is, whether the fluid is laminar or turbulent. Laminar flow is characterised as being consistent and smooth where as turbulent flow is more random and variable. This randomness can lead to localised changes and differences in the fluid properties, such as the density, which impacts the heat transfer, and thus, thermal flow sensors can not generally be used to detect turbulent flow.

To understand how some of these properties interact with the thermal type sensors described above, there are some common fluid mechanic and thermodynamic principals to know. Ultimately, the heating power, P, of an anemometric flow sensor is given by [3]:

$$P = \frac{NukA_H\Delta T}{L} \tag{2.13}$$

where k is the thermal conductivity of the fluid, A_H is the heated area, ΔT is the difference in temperature between the heated body and the fluid, L is the length of the body and Nu is the Nusselt number. This is a dimensionless number that represents the thermal properties and fluid dynamic properties of the fluid. For flat planes and wires, the Nusselt number can be expressed as [3]:

$$Nu = 0.664\sqrt{Re^3}\sqrt{Pr} \tag{2.14}$$

where Pr is the Prandtl number, which represents the thermal characteristics, and Re represents the Reynolds number, which represents the fluid dynamic properties. The Prandtl number is defined as the ratio of momentum diffusivity (or kinematic viscosity, v) to thermal diffusivity, which is expressed as [3]:

$$Pr = \frac{c_p\mu}{k} \tag{2.15}$$

where c_p it the specific heat capacity of the fluid and μ is its dynamic viscosity. The Prandtl number is therefore unique to each fluid and hence response of the anemometer differs depending on the fluid and so needs to be calibrated accordingly [3].

The Reynolds number is the ratio of inertial to viscous force within the fluid. In this context the Reynolds number is important as it is related to the fluid velocity and hence flow rate via [57, 58]:

$$Re = \frac{\rho uL}{\eta} = \frac{uL}{v} \tag{2.16}$$

Note, L can also be expressed as hydraulic diameter D_h when discussing flow in non-circular channels. When discussing pipe flow, the hydraulic diameter can be made equal to the pipe diameter, and for flow in a square duct,

it is equal to the length of the side of the cross section. The result of the Reynolds number indicates whether the flow is lamina or turbulent. These have implications on the performance of thermal sensors. Laminar flow is where a fluid flows in parallel layers with no disruption between said layers. They are consistent and generally, one can assume that the density and velocity is consistent. Any flow with a Reynolds number of $1 < Re < 2000$ can be described as laminar. Above 4000, the flow is considered turbulent. Turbulent flow can be considered random and chaotic, where there are local unpredictable fluctuations in the fluid parameters such as density and velocity, that would make measurements inconsistent. It is not possible to measure a turbulent flow using a thermal flow sensor. Chapter 3 of this thesis discusses the implications of this and the modelling used to ensure that this will not affect the characterisation and calibration of the devices [3, 57].

2.1.3 Current State of the Art

Thermal flow sensors have several advantages over other mechanical type devices. Using heat transfer principals to determine flow velocity, a sensor that has high sensitivity, is highly accurate, and with a low output drift can be realised, without any moving mechanical parts as in the piezo devices [47]. There are challenges in realising these benefits though. Thermal flow sensors are not ideal for measuring low flow velocities [59], and maintaining the temperature of the heating element is difficult [60]. In addition, heaters made from certain materials have a high heat capacity and therefore suffer from a poor frequency response.

Silicon has been the dominant material for the fabrication of hot-wire/hot-film devices. This is due to its well-known electrothermal properties and the maturity of fabrication. Silicon devices can realise the heating element in either metal or in polysilicon. The benefit of a polysilicon heater is the ability to fine tune its properties by varying the dopant concentration and type [61, 62]. Fabricating devices in a CMOS compatible silicon process enables the drive circuitry to be monolithically incorporated onto the same chip as the sensor itself, thus enabling a complete device in one small, low power package [63, 64].

While the thermoresistive type of transduction is most common for the hot-film device, an alternative is to place thermoelectric/electronic temperature sensing elements underneath the heater. This allows more accurate reading and control of the heater temperature, but at the expense of higher power consumption [65, 66].

Metals are also good materials for fabricating the heating elements of hot-wire/hot-film flow sensors, due to their relatively high TCR and low resistivity. Devices in the literature generally use tungsten, copper, gold, platinum and nickel as the material to fabricate these devices for those reasons [67, 68]. Choice of metal is further restricted by application [54], with platinum and gold considered as bio safe for such applications.

Hot-film sensors are mechanically more robust than their hot-wire counterparts. This does however, come at the expense of increased heat transfer into the membrane, leading to an increase in power consumption and a decrease in sensitivity. Efforts have been made to overcome this issue. Silicon nitride and other polymers have been used as passivation layers. A device made by Gardner *et al.* [69] used isolating membrane holes to achieve an improvement in sensitivity without sacrificing structural robustness. Sensitivity to measuring CO_2 percentage improved by 39.2%. Also in the same group, De Luca *et al.* developed a thermoelectric version, incorporating five tungsten hot-wires in a dielectric membrane of Si_3N_4, making a highly sensitive device [56].

Calorimetric devices, in contrast to the hot-wire/hot-film devices, are highly sensitive to low flow rate, but saturate at higher rates, limiting the sensing range [54]. Devices can be fabricated with semiconductor elements, such as polysilicon thermoresistors or diodes, or metals, or a combination, such as thermocouple temperature sensors. These devices are also capable of detecting flow direction, and with further processing, the thermal conductivity of the fluid [69, 70, 71].

A device by Dijkstra *et al.* was demonstrated in [72] for its low flow rate detection characteristics. The sensor was capable of detecting flow rates as low as 300 nL/min with a sensitivity of 218 µV/(µL/min). Calorimetric flow sensors can be used to detect wall shear stress, which is useful for detecting

when a turbulent boundary layer is larger than the laminar [73, 74]. Although the magnitudes involved in most aero applications are larger than the dynamic range of the devices.

Various materials are used for the various elements in the calorimetric sensor, all of which have an effect on the sensitivity and dynamic range of the sensor. A device reported by [75] which uses a W/Ti heater in conjunction with a P-doped polysilicon thermopile achieved a sensitivity as high as 3.04×10^{-2} V/(m/s) over a range of 0-50 m/s using zero air as the fluid. [70] reported a device with a polysilicon micro heater and an Al/polysilicon thermocouple with a sensitivity of 230 V/(m/s)/W over a smaller range of 0-11 m/s.

Thermal flow sensors are by far the most popular type of flow sensors for a number of reasons, including; low-cost, reliability, high accuracy, ability to monitor flow velocity, direction, and thermal conductivity. Because of these benefits, there is a growing demand to place these devices in harsher environments, and the current generation of devices, are susceptible to extreme temperature, corrosiveness, and radiation. Some work has been done in the area of harsh environment flow sensing. [76] shows a flow sensor protected by a SiC layer for this purpose.

2.2 Pressure Sensors

Pressure is one of the most influential physical parameters in many processes such as medical equipment, industrial hydraulics. This has created a large market for sensors to measure this parameter. There are several approaches to creating MEMS pressure sensors. Pressure sensors can be divided into categories based on the transduction principle, such as piezoresistive, capacitive, resonant, piezoelectric. Most MEMS pressure sensors have some part that deflects based on the applied load such as a membrane, with extra components embedded on the membrane to detect the deflection.

The capacitive based sensor typically includes two parallel plates, where the distance between said plates varies according to the applied pressure. These plates can be electrodes attached to a membrane structure with a metal-

lic base, or film based electrode over a cavity. Equation 2.17 [77] shows the capacitance equation where S is the surface area of the plates and D is the distance between them.

$$C = \varepsilon_0 \varepsilon_r \frac{S}{D} \tag{2.17}$$

Piezoresisitvie devices typically use a deflecting membrane or diaphragm above a cavity. When pressure is applied to the membrane, it deflects and generates strain. This strain can then be measured by piezoresistive devices implanted on the membrane. These devices are usually placed near to the edge to maximise the strain. When using piezoresistors, a Wheatstone bridge can be constructed for the sensing. A number of materials can be used to create the piezo devices including, single crystal silicon, polysilicon and graphene. The use of doped silicon resistors over metal has allowed the size of these devices to be shrunk into the millimetre range [78]. Silicon doped piezoresistors have been shown to have a gauge factor 100 time that of metals, depending on the doping level [79]. Crystallographic orientation of the wafer is a key consideration when maximising the gauge factor (ratio between change in resistivity and strain) of the piezoresistive devices. In silicon processes, the best orientation to use is $< 100 >$. Choice of material is influenced by the application (does it need to be bio safe? or operate at high temperature?), in addition to the sensitivity required [80].

The cavity of these devices needs to be sealed away from the pressure generating environment, as the pressure measured on the top of the membrane can be said to be relative to the pressure below. Controlling the pressure in this cavity is important. If the cavity is sealed as a vacuum, then the device can measure absolute pressure. Alternatively, the cavity can be left open so that the gauge pressure is measured. Wafer-to-wafer bonding is often used to achieve this, and can be of various methods such as anodic, fusion glass bonding or eutectic and solder bonding [81, 82, 83]. The devices reported in this work are of the gauge type, where a hole in the underside of the PCB package equalises the pressure to the general surroundings.

The cavity can be formed using various techniques such as surface micro-

machining or etching. Deep Reactive-Ion Etching (DRIE) is typically used to create membrane type cavities due to the ability to create steep sharp edges which aids in minimising the size of the device. In a silicon process, the etch stop will typically be p-type silicon or a buried oxide layer. GaN-on-Si has an advantage here, as the silicon substrate can be etched away using standard silicon etching techniques, and use the GaN stack as the etch stop, thus avoiding an extra processing step.

While there is an established body of work on silicon pressure sensors, these devices are generally rated to a maximum of 125 °C. New materials have been explored for use in harsh environments. Devices fabricated in SOI, SiC, and GaN have been reported in the literature. [84] demonstrates an SOI piezoresistive pressure sensor that could work up to 600°C, with an active silicon layer. [85] demonstrates a SiC device with an increased sensitivity between 400°C and 800°C.

GaN has several advantages over these materials and others. Both GaN and SOI can be grown on silicon substrates to lower the cost, but GaN, as with other III-N devices, can be monolithically integrated with drive circuitry. In addition, GaN has HEMTs with have much higher mobilities [86, 87], a higher critical breakdown field [88, 86], lower on-resistance [88], and higher switching speed than SiC [87, 89].

While it is less mature, there are already examples of GaN pressure sensors in literature, which vary through transduction principals and with alloy materials. AlGaN/GaN devices have been shown in [90, 91, 92], where the formation of the 2DEG quantum well is a result of piezoelectric polarisation, caused by strain. This relationship has been exploited by using the 2DEG as a strain gauge in itself, and through the use of HEMTs, the shape of which can be like traditional rectangular channels, or as a circular HEMT (also known as a ring HEMT) embedded around the edge of the membrane [93, 94, 95, 96, 97, 98].

In addition to just the strain, the biasing conditions of the HEMT play a part in its sensitivity to pressure. A suspended membrane based AlGaN/GaN HEMT presented by [91] studies the pressure sensing performance with the HEMT operating in different regimes. They found that setting the gate voltage

so that the devices were operating in the weak inversion scheme enhanced the sensitivity of the drain current. Coupled with a carefully selected drain-source voltage, the response achieved was found to be 170 times larger than for the strong inversion regime.

A unique take on the ring-HEMT design was reported by [99] where the membrane includes a Si bulk pillar in the middle. This work showed that the saturation current is 14% lower for the membrane based device compared to the Si pillar.

Vanco in [100] presents a multitude of C-HEMT structures for stress detection. In that work, a GaN on SiC structure is presented, and various operation configurations of the heterojunction are reported. The work reported an unbiased Schottky diode, a 2DEG resistor, and a C-HEMT structure. The work found that all three were effective at measuring stress. The 2DEG resistor design is improved by applying a gate bias, near to the pinch off, and the Schottky diode showed good linearity and sensitivity that was independent of frequency. An AlGaN/GaN Schottky diode pressure sensor was demonstrate by [101] up to 36 kPa with a frequency independent sensitivity of 4.4 pC/kPa.

A less explored variation of the GaN platform uses an InAlN/GaN hetrojunction. These have the advantage over AlGaN/GaN based devices in that the peak operating temperature can be as high as 1000°C, as the issues caused by lattice mismatch between the alloy and the GaN that are a limiting factor in AlGaN/GaN do not occur in the InAlN devices. [102] demonstrated an InAlN/GaN on Si ring-HEMT membrane pressure sensor. The peak sensitivity measured was 0.64 %/psig up to 196.5kPa. The work compared released and unreleased devices up to 300°C, which showed the released device is less conductive than the solid-state device for all bias conditions. This is caused by a reduction in the thin film stress in the released device. The limiting factor in high temperature operation of this device was the packaging used [12]. This is a common theme across many harsh environment devices, in that the lack of suitable packaging is the limiting factor in high temperature operation, rather than the semiconductor architecture itself [103].

2.3 Gallium Nitride

Gallium Nitride is a wide band-gap semiconductor. GaN allows the fabrication of HEMT, which is a type of heterogeneous field effect transistor. GaN based HEMTs outperform silicon based devices in electrical terms such as power density, low on-state resistance, high switching speed, and in mechanical terms such as thermal stability and radiation hardness. The conduction channel of the HEMT is formed of a 2DEG region at the heterojunction between the GaN crystal and some other alloy (such as AlGaN or InAlN).

GaN layers can be grown using various methods such as Molecular Beam Epitaxy (MBE), Hydride Vapor Phase Epitaxy (HVPE), or Metalorganic Chemical Vapour Deposition (MOCVD). A major obstacle in the fabrication of GaN is the lack of a suitable lattice match and a thermally compatible substrate. To combat this, a seed layer is normally used between the substrate (silicon in our case) and the GaN layers. This layer is usually Aluminium Nitride or AlGaN, and is followed by a graded AlGaN buffer. This aids in limiting damaged caused by the different thermal expansions of the GaN and Silicon. Ideally, one would grow devices using a GaN-on-GaN structure, however there are several issues with this, including the high cost of a GaN wafer, its small size, and number of impurities. Thus it is desirable to use a process which develops the GaN layers on top of a substrate of a different material. Silicon is an excellent candidate for this due to its low cost, established fabrication process, and the ability to effectively manage thermal mismatching.

Table 2.1: Physical Properties of Substrates [1] [2]

Substrate	AlN	GaN	Al_2O_3	SiC	Si
Bandgap [eV]	6.28	3.47	7.0-7.6	2.4-3.2	1.1
Thermal Conductivity [W/cmK]	3.3	1.3	0.5	3.0-3.8	1-1.5
Thermal expansion [10^{-6}/K]	5.27	5.6	8.1-8.4	2.9-3.3	2.6
Lattice mismatch [%]	-2.4	-	-16	+3.5	-17
Resistivity	high	high	high	high	medium
Cost	high	high	low	high	low
Wafer size [inch]	small	small	6	6	12

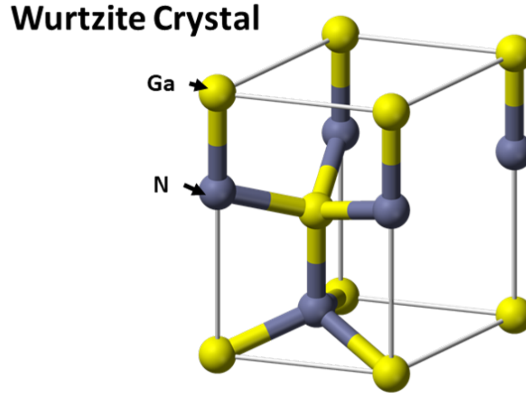

Figure 2.4: GaN Wurtzite Crystal Structure with Gallium and Nitrogen atoms labelled.

2.3.1 AlGaN/GaN Heterostructure

The area of interest in using GaN as a material for sensors rests in the properties and characteristics of the heterostructure. The heterostructure, which includes the heterojunction is formed between two semiconductors with different energy band-gaps (E_g), permittivities (ϵ_s), work functions ($q\phi_s$), and electron affinities (χ_s). The discontinuity in the conduction band creates a triangular quantum well, which leads to the formation of the 2DEG at the boundary of the materials. While for most conventional III-V semiconductors the 2DEG is achieved with a doped layer, in AlGaN/GaN heterostructures, the channel is created by the piezoelectric polarisation at the boundary of each material. The 2DEG region is not in reality two-dimensional but has a thickness in the order of angstroms, which means that it can be described as such in most practical applications [104].

GaN has a wurtzite crystal (fig. 2.4), which is tetrahedrally coordinated and lacks symmetry in the z-direction. This lack of symmetry, along with the large ionicity of the covalent bond, causes a large polarisation to occur along the z-axis ($P_{pz,z}$). This gives AlGaN/GaN based devices the ability to achieve carrier concentrations $n_s(x)$ well above $10^{13} cm^{-2}$ without intentional doping. This is in excess of anything achievable with other III-V materials.

The piezoelectric polarisation is defined as

$$P_{pz,z} = e_{33}\varepsilon_z + e_{31}(\varepsilon_x + \varepsilon_y) \tag{2.18}$$

where e_{ij} represents the piezoelectric constants and ε_i represents the strain in various directions [104]. The total polarisation in the structure is composed of the difference in spontaneous polarisation and the difference in piezoelectric polarisation between the GaN and the barrier layer (AlGaN in this work), as is given by

$$P_{tot} = (P_{sp}^{GaN} + P_{pz}^{GaN}) - (P_{sp}^{AlGaN} + P_{pz}^{AlGaN}) \tag{2.19}$$

The spontaneous polarisation of the barrier layer is calculated via linear interpolation and bow factor. Lattice strain only affects the barrier layer and so P_{pz}^{GaN} can be assumed to be zero in unstrained structures. Strain caused by external forces (such as pressure), affect both the GaN and AlGaN layers.

With the piezoelectric polarisation, the carrier concentration can be calculated using

$$n_s(\varepsilon) = \frac{P_{tot}(\varepsilon)}{q} - (\frac{\epsilon_0 \epsilon_{AlGaN}}{q^2 d_{AlGaN}})[\phi_B(\varepsilon) - (E_f - E_c)_{int}^{\gamma} - \Delta E_C(\varepsilon)] \tag{2.20}$$

where q is the element charge, ε_0 is the vacuum permittivity, ε_{AlGaN} is the relative permittivity of the barrier layer, d_{AlGaN} is the thickness of the barrier layer, ϕ_B is the Schottky barrier height, $(E_f - E_c)_{int}^{\gamma}$ is the Fermi level with respect to the GaN production band energy, and $\Delta E_C(\varepsilon)$ is the difference in the conduction band offset at the AlGaN/GaN interface [104].

2.3.2 The High Electron Mobility Transistor

A number of transduction methods exist for AlGaN/GaN sensor structures. The main one is the HEMT, also known as the Hetrojunction Field Effect Transistor (HFET). HEMTs exhibit benefits over other types of transistors in modern applications such as higher carrier concentrations and superior electron mobility. This superior mobility is a product of the 2DEG that forms at the heterojunction [105]. Unlike conventional transistors, such as MOSFETs,

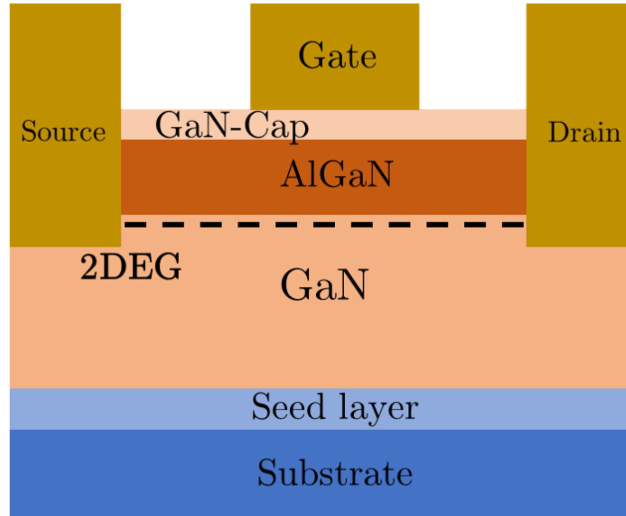

Figure 2.5: Cross section of a typical AlGaN/GaN HEMT

the 2DEG channel does not contain any doped impurities, and so there are less impure atoms for electrons to collide with and slow them down, meaning a lower on resistance [105]. Figure 2.5 shows the cross-section of a typical AlGaN/GaN HEMT. Most conventional HEMTs are depletion mode devices, meaning that they are normally on when there is no gate bias, and thus a DC supply is required to bias the device into the off-state. There are enhancement mode, normally off, devices which have come to market more recently in the last 10 years. These devices require some DC bias at the gate to turn on, which would increase the power consumption. The work in this thesis uses depletion mode devices as the mechanical transduction principles of the HEMT can be used without the need to bias the gate.

On the gate terminal, a Schottky contact is formed with the underlying semiconductor layer. The choice of material for this contact is important as the work function of the metal influences the barrier height. Generally, a metal with a high workfunction should be used for GaN based devices. Table 2.2 shows the workfunctions of common metals used to form the Schottky contact. In sensing applications, the choice of material can also influence the response of the HEMT to various substances, such as in [106], where a HEMT with a Pt gate is used as a hydrogen detector [107, 108, 109]. The process used in this work uses gold metallisation.

Table 2.2: Workfunctions for Schottky contact metals

Metal	Workfunction (eV)
Ag	4.26
Al	4.28
Ti	4.33
Mo	4.60
Au	5.10
Ni	5.15
Pt	5.65

For the ohmic contact, the aim is to achieve a low resistance connection to the semiconductor material. This is done by minimising the barrier height. For most processes, the ohmic contacts are based on Ti/Au metallisation schemes. For the process used in this work, the metal stack consists of Ti/Al/Mo/Au, which is then annealed at 800 °C Each metal has a specific purpose in achieving the low resistance contact. The Ti acts as an adhesion layer to provide mechanical stability, dissolves the oxide present on the surface of the AlGaN, and reacts to form TiN in the AlGaN, which dopes the surface, allowing electrons to tunnel through the metal-semiconductor barrier, which reduces the contact resistance. The Al prevents the Ti from oxidising. Mo prevents mixing of the Au and Al layers, which can form a highly resistive layer. Finally, Au is used to improve conductivity.

Fabrication

Individual processes will have their fabrication steps fine tuned to the specifics of the application and the proprieties of the HEMT structure. The general process is the same. For a GaN-on-Si process, epitaxy layers are built up on a silicon wafer via MOCVD, with layers optimised to manage issues such as thermal expansion mismatch, defect destiny, and lattice strain. An overview of a generic process similar to the one used in this work is detailed below.

MEMS devices require certain extra steps than standard power devices, in order to create mechanical structures. This is a challenge for GaN devices, as its inherit chemical stability means that directly etching the GaN is difficult

[110]. A key advantage of the silicon substrate is that while the GaN itself may not be etched easily, the silicon can. Hence a number of techniques have been used to etch only the silicon parts leaving complex structures made from the GaN stack [111, 112]. Figure 2.6 shows the fabrication steps discussed below.

1. Si substrate. Fabrication begins with the Si substrate. This is typically a $< 111 >$ orientated wafer with a thickness of 1 mm. The thicker wafer provides a lower final bow and has better mechanical resilience than a thinner one. The substrate is normally high resistance p-type silicon, fig. 2.6 (a).

2. AlN Nucleation layer. This layer reduces some of the lattice mismatch strain between the Si substrate and the GaN layers. This layer also prevents meltback etching of the substrate by the Ga faces in later layers. The oxide layer on top of the Si is removed prior to AlN growth by annealing in a H_2 atmosphere and an amonia predose fig. 2.6 (b).

3. AlGaN buffer. This is a graded AlGaN buffer layer, whose primary function is strain management. The lattice mismatch between the AlN and GaN is of a compressive nature, which balances the tensile stress from the lattice and thermal expansion mismatch between the Si GaN stack. Some fine tuning of the parameters of this layer are done to minimise leakage through the buffer (Fe doping for example), and the grade at the top is fixed to prevent injection carriers into the buffer fig. 2.6 (c).

4. GaN buffer. This is a buffer layer that separates the active GaN from the AlGaN graded buffer. This reduces the defect density in the active GaN and contributes to strain management.

5. GaN Channel. This is the main active layer of the GaN HEMT which forms the 2DEG heterojunction. The parameters of this layer are optimised for the electrical performance of the HEMT. An AlN layer between this layer and the previous one acts as an etch stop when releasing the membrane fig. 2.6 (d).

6. AlGaN barrier. This is the wider bandgap component of the heterojunction that forms the 2DEG fig. 2.6 (e).
7. GaN cap. A 2nm thick layer that protects the AlGaN barrier in further processing fig. 2.6 [113] (f).
8. Metallisation. Openings are made in the AlGaN layer to form the ohmic contacts. See the previous section for contact stack fabrication. Gold metallisation is used for the metal tracks fig. 2.6 (g).
9. Passivation. A standard Si_3N_4 passivation layer with openings where the metallic pads are.
10. Membrane release. The Si substrate and the graded barrier are etched away with a DRIE process, using the AlN between the GaN layers as the etch stop fig. 2.6 (g).

2.3.3 GaN for Harsh Environments

GaN, along with other wide band-gap semiconductors has become a material of interest in harsh environment sensor applications [114]. Progress has been made in materials such as diamond and SiC for both sensor and power electronics applications, and now mature fabrication methods are available to create reliable devices.

Both GaN and SOI can be grown on silicon substrates to lower the cost, and both, as well as other III-N devices, can be monolithically integrated with drive circuitry. Specifically for GaN devices, these can be monolithically integrated with high-frequency circuits to create a remote sensing system. In addition, GaN has HEMTs with have much higher mobilities [86, 87], a higher critical breakdown field [88, 86], lower on-resistance [88], and higher switching speed than SiC [87, 89].

While GaN has been proven to be an effective material for survival in harsh environments, there are still some considerations that need to be accounted for. While using the 2DEG in a high temperature environment, there are three limiting mechanisms which affect performance of the devices.

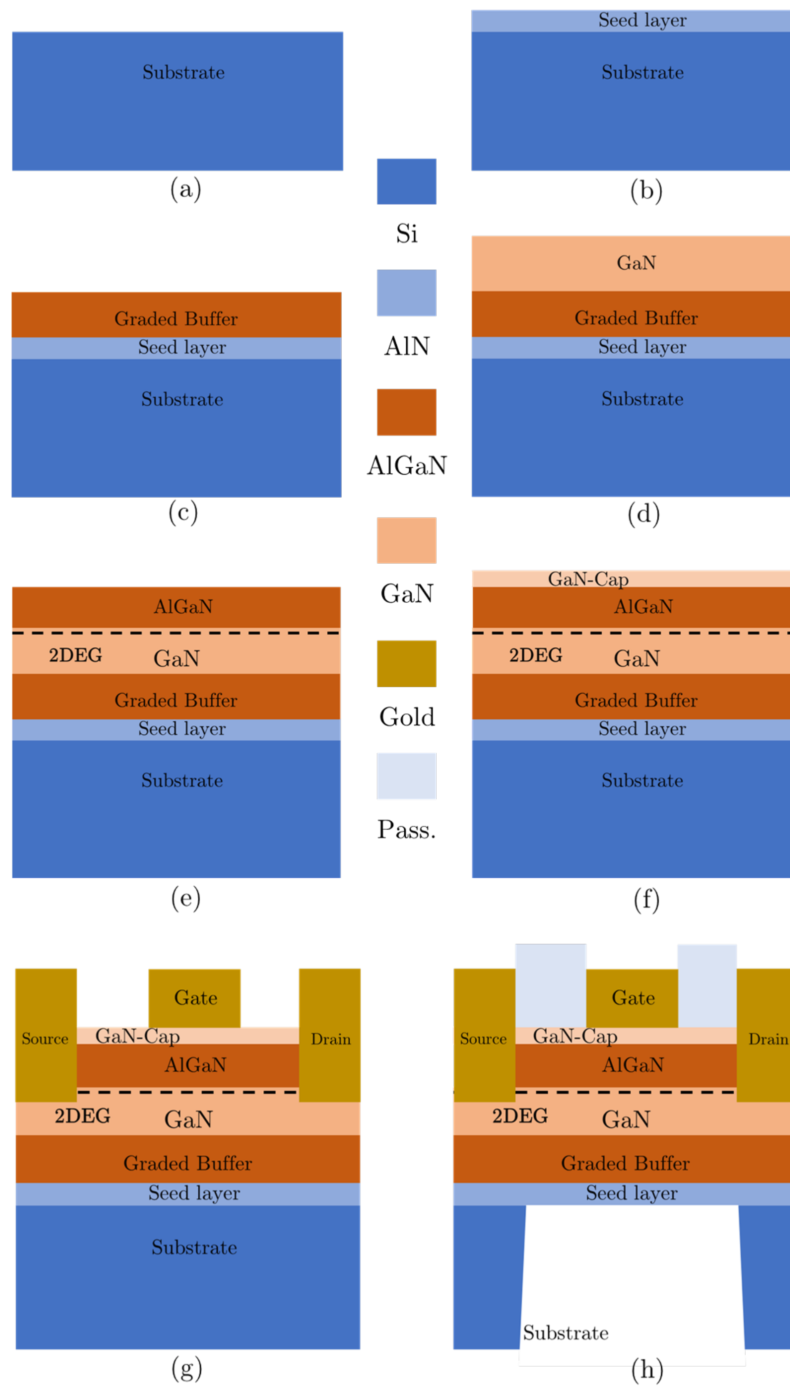

Figure 2.6: GaN HEMT fabrication steps (Simplified). (a) Silicon wafer, (b) AlN Seed layer, (c) Graded AlGaN layer, (d) GaN layers, (e) AlGaN layer, (f) GaN cap, (g) Gold metallisation, (h) Passivation and membrane release

First is the decline in mobility, that is, the velocity of the carriers through the materials' electric field. There are 3 primary scattering mechanisms that impact the mobility of the carrier in the 2DEG. These are:

Phonon scattering - This includes 3 types of phonon scattering, acoustic, piezoelectric acoustic, and polar optical. The phonons are essentially vibration energy of the atoms in the crystal structure [115, 116, 117]. In the 2DEG, the acoustic scattering is considered more prevalent at room temperature, while the optical scattering tends to dominate at elevated temperatures.

Coulomb scattering - This is due to interface charges, dopants, and ionized impurities. Ionized impurities in the GaN layer are the main contributor of this type of scattering [116].

Alloy disorder scattering - This is where electrons in the 2DEG penetrate into the AlGaN layer. This can be mitigated with an AlN barrier layer between the GaN and AlGaN, and is dependent on the carrier concentration [117, 116].

These scattering forms are also related to the 2DEG sheet density, where certain types of scattering, such as the ionized impurity and optical phonon scanning, are filtered by the electrons in the 2DEG, thus a higher carrier concentration is more desirable [118]. On the other hand, the alloy disorder scattering increases with 2DEG carrier concentration [119]. Consideration should be given to the temperature dependencies of the scattering, as certain scattering, the optical polar, are highly temperature dependent [120, 116].

Work done in the literature shows that AlGaN/GaN 2DEG have an electron mobility in the range of 1500 to 2500 $cm^2\,s/V$. After accounting for the temperature dependence, this is around 4 to 8 times lower at 300°C [121, 122].

Second is the change in 2DEG carrier concentration. Studies have been done into both the effects of strain and temperature on the 2DEG. When under high temperatures, AlGaN/GaN devices can experience strain relaxation. This is where some of the strain the crystals are relieved by defects caused by the build up of strain [118]. This decrease in strain leads to a decrease in the carrier concentration of the 2DEG, thus giving a theoretical upper limit to its

conduction.

Third is the degradation of the ohmic contact over time. This could be down to thermal cycling or the high temperature operation itself.

All of these factors need to be considered when assessing the performance and longevity of GaN devices that aim for a harsh environment application.

2.3.4 GaN Sensors

There are multiple types of sensors reported in the literature that are fabricated in a GaN process. Table 2.3 shows a number of highlights that were found in the literature, although this list is not exhaustive of the types of devices available. These devices can be used for multiple sensing applications, such as chemical, gas, biological, pressure, temperature. These have come out of a drive to develop sensors that can take measurements in harsh environments in addition to taking advantage of the unique properties and dependencies of the heterostructures.

AlGaN/GaN Heterostructures

This chapter has already covered pressure sensors, but there are other types of physical sensors that can be made.

Chemical sensors

By adjusting the gate material on the HEMT Schottky contact, it is possible to make the device sensitive to a variety of chemical phenomena. pH sensors are popular in GaN as the chemical stability of the stack reduces the long-term degradation of the device. Several of these have been reported in literature with different dielectrics on the gate such as Sc_2O_3 in [123] or in other cases with an open gate device. This means that the AlGaN material above the gate is exposed, and the acids polarise the device through this gap in the passivation [124, 125, 126].

Chu *et al.* reported a wireless pH and glucose AlGaN/GaN HEMT sensor in [127] for breath analysis. This work used Sc_2O_3 as the gate dielectric material for the pH sensor, and grew an array of zinc oxide (ZnO) nanorods on top of the gate surface for the glucose sensor. Both devices here work together to decouple the affects of pH on the activity of the glucose oxidase enzyme (GO_x) [128].

Similar sensors can be made to detect any substance that is polar in nature. These types of substances change the surface charges in the gate region, which changes the surface potential at the interface [129]. Devices have been reported for ion detection of ammonium [130], mercury [131], potassium [130], acetone, methanol, and propanol [129], to name a few.

Biosensors

By using biocompatible materials with the GaN structure, it is possible to create devices that can detect several different biological substances such as biomarkers and enzymes [132]. Work has been done on the detection of the prostate specific antigen (PSA) using AlGaN/GaN heterostructure, the earliest reported by [133], where an Au gated HEMT is used. The PSA was attached to the gate by forming ester bonds with thioglycolic acid at the gate. This device could detect concentrations from 1 µg/ml to 10 pg/ml. More recent devices have been reported by [134] and [135], where a HEMT with a disposable sensing chamber is connected to the gate that incubates the PSA.

In addition to prostate cancer, devices have been shown, through a similar approach, to be able to detect other markers, such as kidney injury molecule-1 (KIM-1) for kidney disease [136], and the c-erb-2 antigen for breast cancer [137]. These devices similarly use binding solutions to attach the relevant molecule to the HEMT gate.

Gas

Work has been done to use the properties of the GaN heterostructure to detect various gases using both a HEMT and Schottky diode configuration. The

primary gas discussed in literature is hydrogen, where the presence of hydrogen causes a change in the current of the Schottky diode. This is down to the hydrogen molecules lowering the effective barrier height as they catalytically crack the metal gate. The hydrogen molecules then diffuse into the metal, typically platinum, and to the GaN interface where they change the effective surface charge [129]. A similar phenomenon occurs in HEMTs. The magnitude of the current change induced by the effect can be increased significantly by having a native oxide between the GaN layers and the gate metal [138].

Thermal conductivity gas sensors using micro-hotplates are used in conventional silicon devices for high sensitivity and high bandwidth detection. Some limited work has been to bring these benefits to GaN and other wide bandgap semiconductors.[139] presents a micro-hotplate using the 2DEG region of an AlGaN/GaN structure as the heating element, with the purpose of elevating the temperature of sensing environments to enhance the sensitivity of other devices. They achieved a hot-plate temperature or 600 °C, with a bias of 40 V. [140] presents a comparison of micromachined hot-plates made in GaN, GaAs, and silicon. This work showed that the electrothermal efficiency of the GaN devices was similar to that of the silicon, but a higher operating temperature was possible.

2.3.5 GaN-on-Si as a Sensing Platform

This work is focused on the development of GaN-on-Si as a sensing platform. Silicon is a popular substrate for fabricating GaN structures due to its low cost and the ability to use silicon based MEMS processing steps for sensor applications. The ultimate goal is to produce a single chip that is capable of detecting flow, temperature, pressure, and gas thermal conductivity fabricated in GaN technology [141].

This review of the literature has identified certain capabilities that need to be developed to achieve this goal. The search of the literature has shown that a GaN thermal flow sensor has never been achieved in any form. This work herein looks to develop such a device in different implementations. Firstly, a relatively simple device will be fabricated using a metal hot-wire as the heat

source of the device. Secondly, this work will use the unique temperature dependent properties of the 2DEG to realise a thermal flow sensor using the 2DEG as the heating and sensing element. The flow sensor will be expanded to operate in a calorimetric configuration to detect the thermal conductivity of fluid. using this design, some statistical processing will be done to realise for the first time, a GaN-on-Si flow sensor that simultaneously discriminates between flow rate and gas concentration.

The ultimate goal of this research would be to fabricate a GaN-on-Si combo-chip that is capable of sensing pressure, flow, thermal conductivity, and temperature on one die, which could be integrated with an ASIC with circuitry in a system in a package or system on a chip configuration. While there already is a body of work on the ring-HEMT pressure sensor, its integration on a combo chip has not been done before and this work will develop the capability to fabricate such a device in the specific process.

Table 2.3: Selected GaN sensors from literature

Domain	Measured	Principle	Sensitivity	Range	Ref
Magnetic	Magnetic Field	Hall Effect	55 V/AT		[142]
Magnetic	Magnetic Field	Hall Effect	0.35 G/(Hz)$^{1/2}$	0-0.5 T	[143]
Magnetic	Magnetic Field	Hall Effect	80 V/AT		[144]
Magnetic	Magnetic Field	Hall Effect	60 V/AT		[145]
Mechanical	Pressure	Capacitive	0.86 pF/bar	-0.5 - +1 bar	[146]
Mechanical	Pressure	Ring-HEMT Piezo	4.4 pC/kPa	0 - 36 kPa	[147], [148]
Mechanical	Pressure	Canilever HEMT Piezo			[149]
Mechanical	Pressure	Conductance	170 nVfm^{-1}		[150]
Mechanical	Stress	Ring-HEMT	0.64%/psig	0 - 28.5 psig	[151]
Mechanical	Stress	Ring-HEMT			[152]
Mechanical	Temperature	2DEG Resistor		3-1000 K	[153]
Mechanical	Temperature	HEMT	-6.5 mV/°C	25-250°C	[154]
Mechanical	Temperature	SAW			[155]
Mechanical	Temperature	PTAT	0.35 mV/°C	25 - 275 °C	[156]
Chemical	pH	ISFET	58.3 mV/pH	2-12 pH	[157] [158]
Chemical	Hydrogen	Diode	0.3 V	0 - 1% Hydrogen	[159] [160]
Chemical	H_2, NO_2, NH_3, CO_2 (Air quality)	HEMT	various		[161]
Chemical	VOC	HEMT	50 ppm		[162] [163]
Biological	Glucose	HEMT			[164]

Table 2.4: Selected flow sensors from literature

Configuration	Material	Fluid	Sensitivity	Range	Power	Ref
Calorimetric	Ni	Nitrogen	40mV/SLM	0-20sccm to 8 SLPM	-	[165]
Hot-film	Ni	Air	-	0-20 m/s	50 mW	[166]
Hot-film	W/Ti/Pt	DI Water	25.1-3.92e4 µV/(µl min)	0-400 µl/min	3.3-23.5 mW	[167]
Calorimetric	Parylene	DI Water	25.1-3.92e4 µV/(µl min)	0-400 µl/min	3.3-23.5 mW	[167]
Time-of-Flight	-	DI Water	25.1-3.92e4 µV/(µl min)	0-400 µl/min	3.3-23.5 mW	[167]
Calorimetric	Si	Water	-	0-10 ml/min	600 mW	[168]
Calorimetric	Si3N4	Nitrogen	-	0-10 ml/min	600 mW	[168]
Hot-film	Polysilicon	Air	-	0-30 m/s	-	[55]
Hot-film	Pt	CO2	-	0-20 m/s	14 mW	[169]
Hot-film	Pyrex	CO2	-	0-20 m/s	14 mW	[169]
Hot-film	Au	N2	-	0-200 ml/min	-	[170]
Hot-film	Polymide	Water	-	3-167 µl/min	-	[170]
Hot-film	Ti/Pt	Air	7.98 mV/(m s)	0-11m/s	45.1 mW (I=12.96 mA)	[171]
Hot-film	Ti/Pt	Air	27.35 mV/(m s)	0-11m/s	45.1 mW (I=23.08 mA)	[171]
Calorimetric	Germanium	Air	12.99-232.77 V/(m s)	0-5 m/s	0.25-5.8 mW	[172]
Harsh Environment						
Calorimetric	Pt	Nitrogen	-	0-4 m/s	2-20 mW	[173]
Calorimetric	Yttria Zirconia	Nitrogen	0.15 mΩ/sccm	0-40 sccm	2W	[174]
Hot-wire	Poly-Si	Helium/Nitrogen	0.34 mΩ/ppm	0-700 ppm	4.3 mW	[175]
Pseudo-calorimetric	Poly-Si/Al	Nitrogen	-	0-200 SCCM	-	[176]
Hot-wire	Ti (SOI)	Air	-1.3 mV/°C	0-0.7 SLPM	17.99 mW	[177]
Calorimetric	Poly-Si/Al (SOI)	Nitrogen	-	0-8m/s	30 mW	[178]

Chapter 3

Modelling of GaN Devices and Sensors

The physical mechanisms in pressure and flow sensors can be expressed by partial differential equations (PDEs). Using the finite element method (FEM), a problem can be computed by subdividing a domain into several smaller elements which are connected by nodes. The PDEs are then solved for each element before being put back together to show a solution for the whole domain. This chapter discusses the use, and presents the result of FEM modelling of the pressure and flow sensor. The modelling for the flow sensor focuses on determining the length of the flow channel, which the theoretical upper limit of the flow rate detection is based on, due to the turbulence cause by entry effects. Secondly, the modelling of the pressure sensor aims to find the location on the membrane with the maximum strain so as to implant the strain detecting HEMT at that location.

3.1 Flow Chamber Modelling

Given the fundamental heat transfer principle in flow is based on the heat capacity and thermal conductivity of the fluid, the mass and density of the fluid plays an important role in the stable operation of the sensors. Under ideal conditions, the flow would be entirely laminar and so would have a consistent

density across the whole flow channel. There are however several factors which would cause the flow to be somewhat turbulent.

A full sized wind tunnel consists of several sections including the test section, where the flow is most developed and testing occurs, a contraction area which increases the velocity of the flow going into the test section, a laminariser, to make the incoming flow laminar, a diffuser, to draw the fluid out of the test section, and a fan to actively pull the fluid through the system. A flow chamber consisting of all of these components would require an entire room, which would render the use of MEMS to be pointless.

In order to meet the minimisation objective of the sensors discussed in this thesis, a flow chamber geometry was designed that would be small but also able to produce a regular laminar flow needed for a reliable sensor response. This chapter simulates flow chamber geometries to verify laminar flow at various flow rates to inform a theoretical upper limit for the flow rate. The cross section, length of chamber, and flow rate all impact the Reynolds number, which is the main indicator of flow state. This means that all these factors need to be optimised to produce a constant laminar flow.

3.1.1 Theory

A flow can be described as either internal or external. The difference being that internal flow is considered bounded by walls, such as in a pipe or duct [1], and external being unbounded. Depending on this flow type different characteristics and features need to be accounted for to ensure laminar flow. A key consideration is the entrance region. As flow enters a duct, it will take some distance (known as the entrance length, L_e) for the boundary layers to merge and become fully developed (laminar), meaning that the axial velocity is constant in relation to the location in the duct (x) but varies only with the distance from the wall ($u \approx u(r)$). If the boundary layers have not merged, then the flow is turbulent, meaning the velocity profile of the fluid is unstable. Using dimensional analysis, it is possible to show that the entrance length is

[1]Definitions: A pipe is a flow channel with a circular cross section, while a duct is rectangular.

only affected by the Reynolds number and the duct hydraulic diameter, as in equation 3.1 below [57]. As presented in the previous chapter, the Reynolds number is itself related to the flow velocity.

$$\frac{L_e}{d} = g\left(\frac{\rho V d}{\mu}\right) = g(Re_d) \tag{3.1}$$

In the case of laminar flow, the accepted correlation is [2]:

$$\frac{L_e}{d} \approx 0.06 Re_d \tag{3.2}$$

What this equation shows is that with a higher Reynolds number (which is a result of a higher flow rate), the length of the chamber entrance needs to be longer to maintain the laminar flow conditions necessary for the correct function of a thermal flow sensor.

3.1.2 Modelling

There are many software packages available that have the capability to perform Computational Fluid Dynamics (CFD) studies. All these different packages rely fundamentally on the same Navier-Stokes equations. COMSOL Multiphysics 5.4 was used in this work because of the ability to add additional physics interfaces in addition to simple flow.

The duct is to be placed on top of a packaged Printed Circuit Board (PCB) with fixed dimensions. Additionally, the width of the duct is defined by the width of the sensor surface, which in this case was fixed at 2 mm. For simplicity, the height of the duct is also set to be 2 mm to create a square cross-section. Therefore, this simulation work varies the length of the duct. The sensor is assumed to be located in the exact centre of the flow channel in the simulation work. This ensures that the flow characteristics on the sensor are not influenced any more by the outlet than the inlet. For the inlets and outlets, 2 circular vertical tubes were added to represent the barbs connecting the flow channel to the gas rig. The vertical entry would enable the flow to

[2] This holds true up to $Re_d = 2,300$ so the maximum $L_e = 138d$

recombine easier when going through the channel.

The geometry was created in the COMSOL Multiphysics software using a parametrised approach, where the channel length could be adjusted programmatically. The boundary conditions at the inlet were set as a volumetric flow source, while the outlet boundary was set as a zero pressure outlet. All other flow boundaries were set as wall with no slip. This was done using the laminar flow interface. The model was run for three different channel lengths at five different flow rates (twenty five unique combinations) considering only the steady state.

Turbulence effects were not included in this study. The reason being that simulation turbulence in the same way as one would simulate a laminar flow would result in a simulation that would take years to compute. Therefore, a simplified turbulence model is normally applied. These models vary in accuracy and complexity, and often only for limited types of turbulence at any time. Given the expected low Reynolds number of the fluid, and the extra layer of complexity that may not have yielded any useful information. It was decided to only simulate a laminar flow, and look for inconsistencies in the outputs that may show non-laminar behaviour. If the flow is indeed laminar, then the flow velocity profile between the two walls of the chamber will be in the shape of a parabola, otherwise, it will follow a more trapezoidal shape. Most turbulence models are applied on top of a similar study.

3.1.3 Model Outputs

Figure 3.1 shows the velocity profile of the 20 mm flow channel from right to left along the centre line of the channel. This figure matches the theory as the flow profile appear to be more laminar as it progresses through the channel. As the flow transitions from the vertical inlet to the horizontal channel, the flow is forced towards the bottom of the channel before rebounding upwards and distributing more evenly as it progresses through. At the outlet, there appears to be a minimal change in the velocity profile at the direction change from the horizontal channel to the vertical outlet shaft, indicating that the outlet does not have a major impact on the fluid flow over the sensor at the

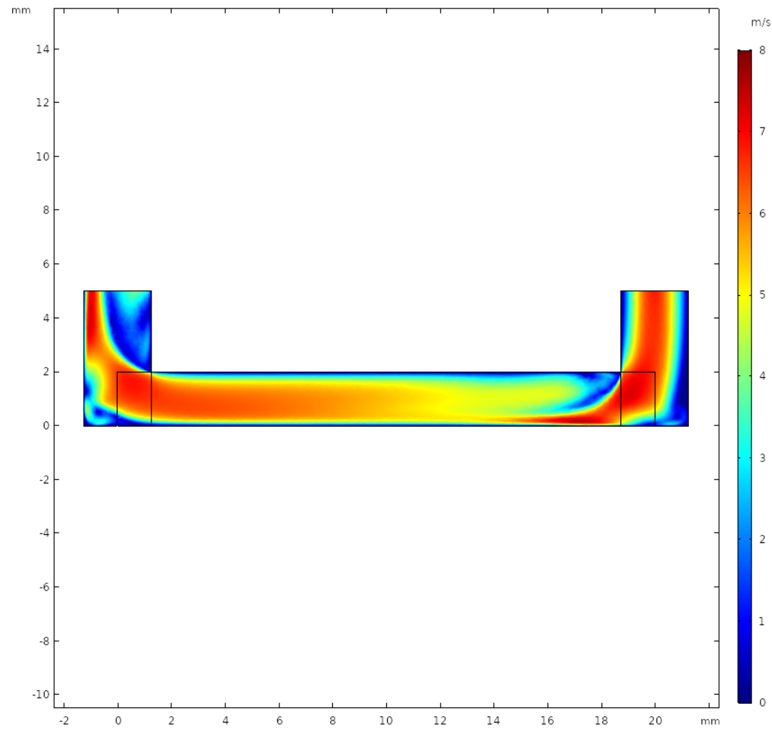

Figure 3.1: Velocity profile of fluid along the centre of the flow channel, i.e. 1 mm from the wall

middle of this channel.

Figure 3.2 shows the velocity profile at the cross section of this channel at the midpoint, where the sensor will be located. The requirement is that this area has a well-defined boundary layer and free from turbulence to generate a reliable and consistent heat transfer from the sensor. While the top of the channel shows that the boundaries have not merged by that point, the bottom of the channel shows a more consistent boundary, indicating that the flow here is indeed laminar.

Figures 3.3 and 3.4 show the 1D plots of the velocity profile, vertically along the centre line of the flow channel. In figure 3.3, the volumetric flow rate is fixed at 1 SLPM while the size of the channel is varied. The largest 2 channels show the parabolic profile expected from a laminar flow, while for the smallest channel, the shape is more trapezoidal. The distance immediately above the sensor does however show some consistency with the larger channels. This suggests that the flow may be beginning to transition at this flow rate.

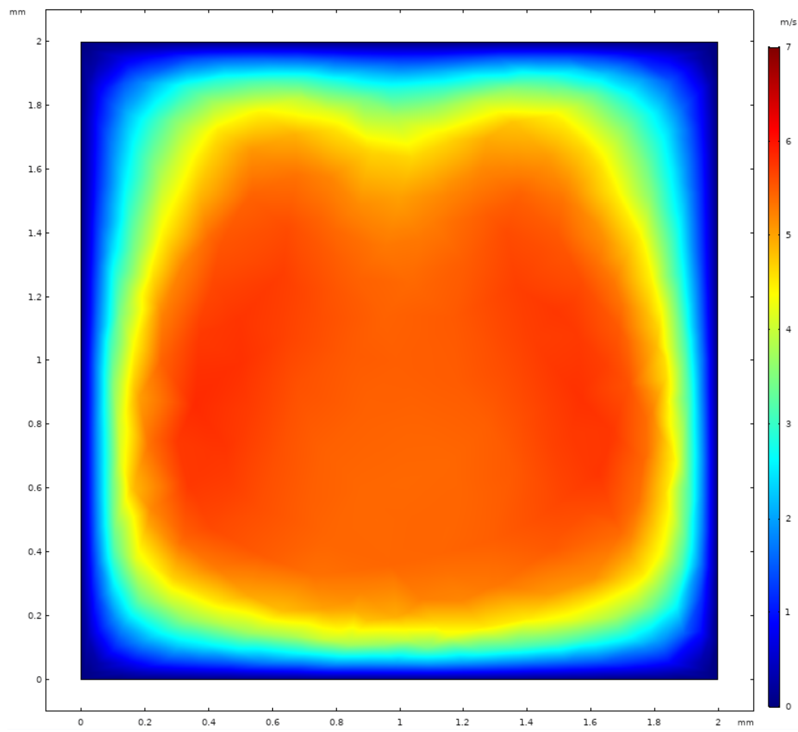

Figure 3.2: Cross section of the velocity profile of fluid at the centre of the flow channel, i.e. 10 mm from the end.

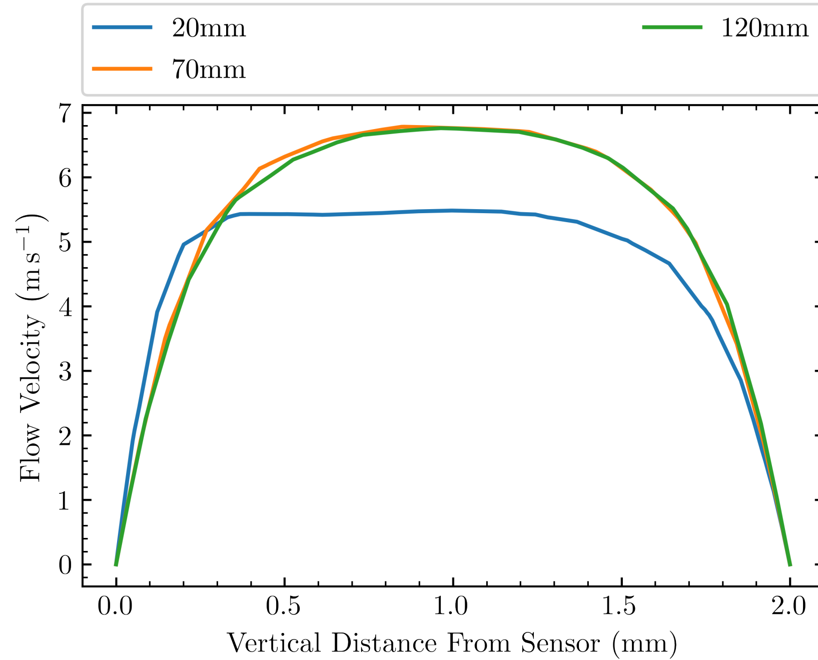

Figure 3.3: Flow velocity at distances away from the sensor. This shows the 3 flow chamber lengths at a constant flow rate of 1 SLPM.

On this basis, and because of specifications with other component suppliers, the 20 mm channel was chosen as sufficient for flow rates up to 1 SLPM. The simulation was run again for just the 20mm channel, varying the flow rate up to 2 SLPM. The channel is valid for flow rates at least up to 1 SLPM. The boundary at 2 SLPM does not suggest that the flow is sufficiently laminar to get a linear relationship up to 2 SLPM. The data suggests that the flow begins to enter the transition region between 1.5 and 2 SLPM. The exact point can be determined experimentally. This and higher rates will we tested experimentally, to see if the sensor output does behave consistently.

3.2 Pressure

The ring-HEMT pressure sensor was modelled in two parts. Firstly, an FEM model was developed in COMSOL Multiphysics, then the outputs of the FEM model used in an analytical model. In COMSOL, a mechanical model was

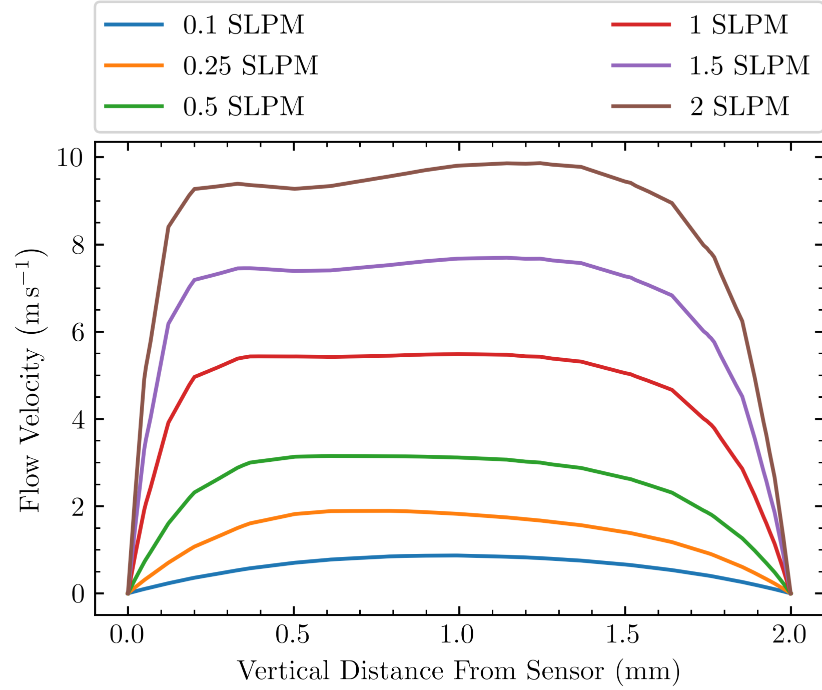

Figure 3.4: Velocity profile of fluid inside the flow chamber

developed that enabled the extraction of the stress and strain parameters of the membrane to be used in the analytical model, that calculates the carrier concentration of the 2DEG in the HEMT. This section discusses the model development and the theoretical basis.

3.2.1 FEM Model

Geometry

The geometry consists of the bulk silicon with the GaN stack on top. The membrane is circular with a radius of 510 µm with air filling the cavity beneath this. In order to save on computation time, the model only simulates a quarter of the device and utilises symmetry to extrapolate the results over the whole geometry. Certain layers of the GaN stack are also ignored. The thin AlGaN epitaxial layer is assumed to take on the bulk properties of the much thicker GaN layer and is thus ignored, as is the GaN cap, which is considered as one

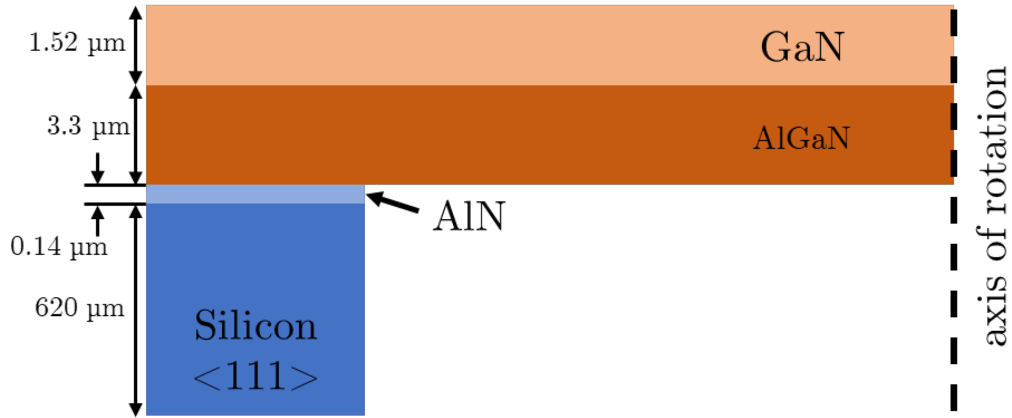

Figure 3.5: Simulated simplified GaN stack structure

continuous GaN layer. This cuts down on computation time. Figure 3.5 shows the simulated stack with the silicon substrate, the AlN seed layer, the graded AlGaN buffer, and finally the GaN layer.

The geometry is meshed with a free triangular structure applied to the bottom boundaries of the GaN stack (where the boundaries are next to the silicon bulk and the air) which is then swept upwards through the structure. A free tetrahedral mesh is used for the larger bulk silicon and air domains. To detect the deflection of the membrane, a moving mesh is applied to the air domain. Generally, the more elements in a model the more accurate the model, however this comes at the expense of computation time. Instead the mesh is optimised for mesh quality, which is a measure based on the mean difference of a measure between adjacent mesh elements.

Material Properties

The model assumes that the materials are anisotropic linear elastic, and as such the stiffness matrix takes on the form shown in (3.3).

$$\begin{bmatrix} C_{11} & C_{12} & C_{13} & 0 & 0 & 0 \\ C_{12} & C_{11} & C_{13} & 0 & 0 & 0 \\ C_{13} & C_{13} & C_{33} & 0 & 0 & 0 \\ 0 & 0 & 0 & C_{44} & 0 & 0 \\ 0 & 0 & 0 & 0 & C_{44} & 0 \\ 0 & 0 & 0 & 0 & 0 & \frac{C_{11}-C_{12}}{2} \end{bmatrix} \tag{3.3}$$

A search of the literature gives a wide range of values for the elastic properties of the materials. The variation in the reported values of these constants at 300K is greater than the variation in the values at various temperatures between 200 K and 500 K, and so this was not accounted for in this model [98]. The values used in this model are shown in table 3.1. Note that the elasticity matrix of silicon does not follow the same form as that of the GaN and AlGaN.

Table 3.1: Elastic coefficients of materials in the model [2]

Crystal Property (GPa)	GaN	AlN	AlGaN	Si
C_{11}	367	396	374.25	165.7
C_{12}	135	137	135.5	63.9
C_{13}	103	108	104.25	C_{12}
C_{33}	405	373	397	C_{11}
C_{44}	95	90	93.75	79.6

Model Specification

The theoretical basis for this model is Hooke's law, which enables the deformation of a crystal due to a stress to be calculated. The solid mechanics interface of COMSOL enables this to be done for the geometry.

Some boundaries were specified. These include; the symmetry axes for the internal boundaries of the chip, a fixed constraint at the bottom of the device to specify a force to act against, and the applied boundary load that represents the pressure, which was applied to the whole of the top of the device.

A parameter sweep was performed of the applied pressure. This went

from 1 Pa to 1 MPa in logarithmic steps, with 5 pressure values per decade, in addition to a 0 Pa base case. The simulation then calculates the displacement and strain on the model.

Model Outputs

Figure 3.6 shows the completed geometry of the sensor, having been simulated with the displacement results shown in COMSOL. Using the symmetry boundary, the re-constructed whole device is shown in figure 3.7. Both of these figures show the device at the point of maximum pressure (1 MPa). Maximum displacement occurs at the centre of the membrane. This maximum displacement was measured as 27.8 µm where the pressure is 1 MPa.

Figure 3.8 shows both the maximum and average displacement of the membrane over the range of pressures simulated. The average membrane displacement was calculated within COMSOL by applying an integration function to the displacement of the top membrane boundary. This figure shows the non-linearity between applied pressure and the displacement, and the range of displacements at various sections of the membrane. The peak average displacement was measured as 6.8 µm. Nano indentation tests were performed on the fabricated membranes[3]. These test were of a point load on the centre of the membrane where a force is applied and the deflection measured. With a point load of 50 mN, the test showed a displacement of 24 µm. 50 mN is the equivalent of 63 kPa based on the geometry of the device. This FEM model shows that at the same pressure the maximum displacement (ie at the centre of the membrane) is around 22 µm. Which, after accounting for the difference between a point load and a uniform pressure, shows a good match. Catastrophic destruction occurs just before a deflection of 30 µm.

On a crystal level, the model outputs contain information about the stress and strain in the membrane. Figure 3.9 shows the Von Mises stress in the device. As expected the region of peak stress is located near the edge of the membrane, this is the best region to implant the 2DEG to get the maximum sensitivity of the HEMT device to the change in pressure.

[3]Nano-indentation test performed by Bogdan Spiridon at University of Cambridge

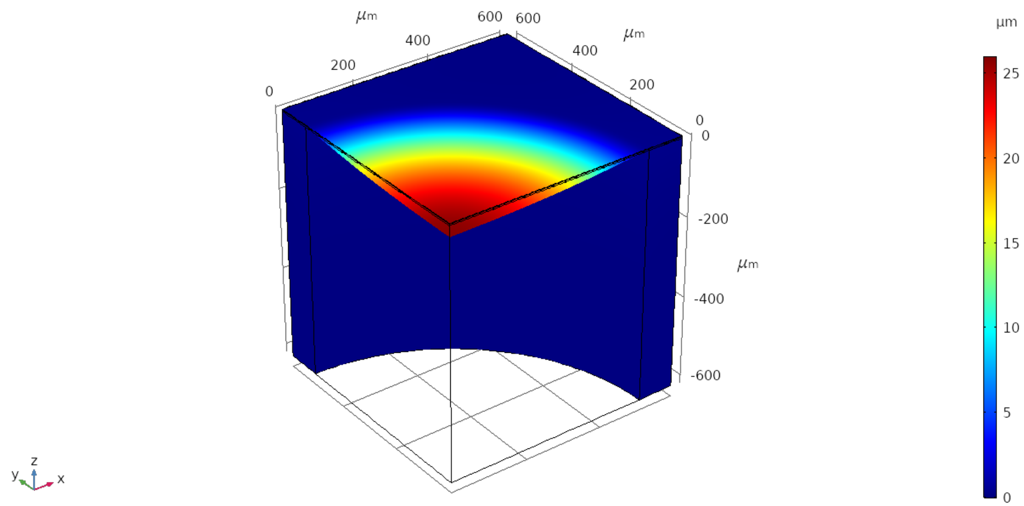

Figure 3.6: Membrane displacement at peak load (1 MPa), showing only the simulated quarter. The black wire frame shows the original position of the membrane

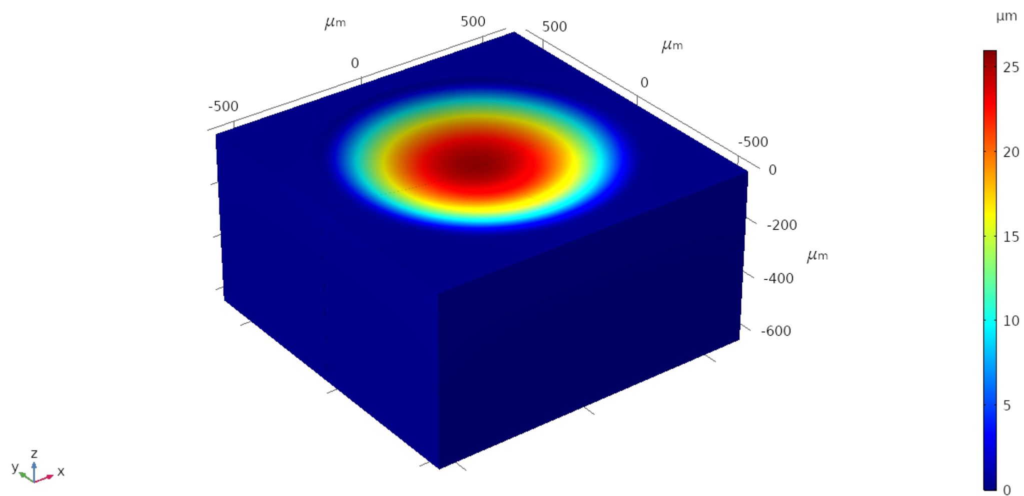

Figure 3.7: Membrane displacement at peak load (1 MPa). This uses symmetry to extrapolate the other 3 quarters not simulated.

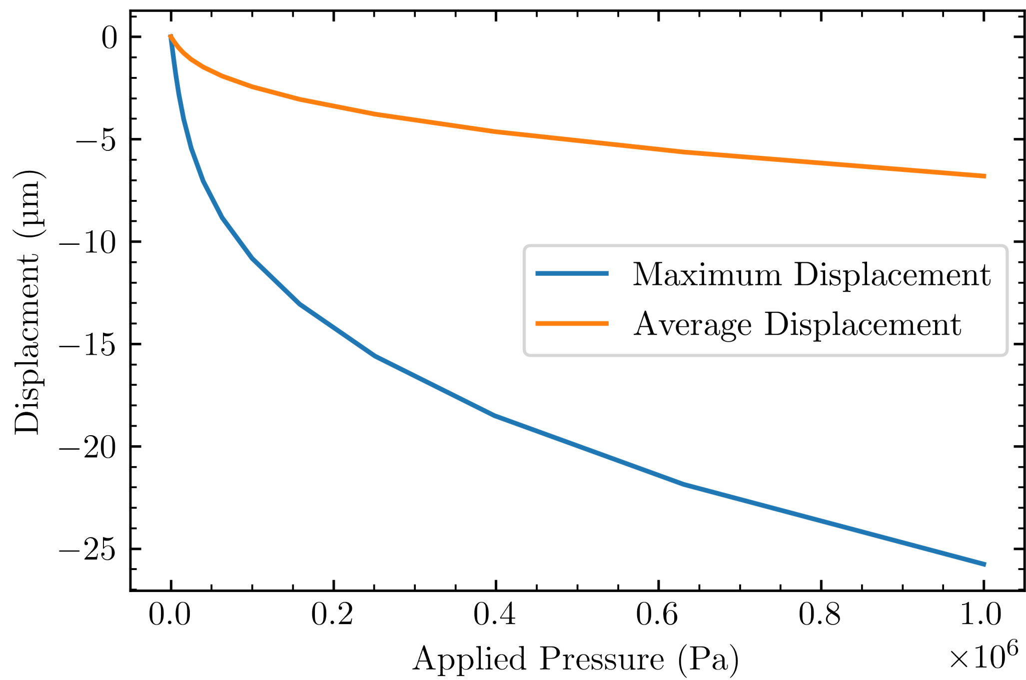

Figure 3.8: Membrane displacement vs applied pressure, showing the maximum displacement at the centre of the membrane, and the average displacement over the membrane taken as the integral of the membrane.

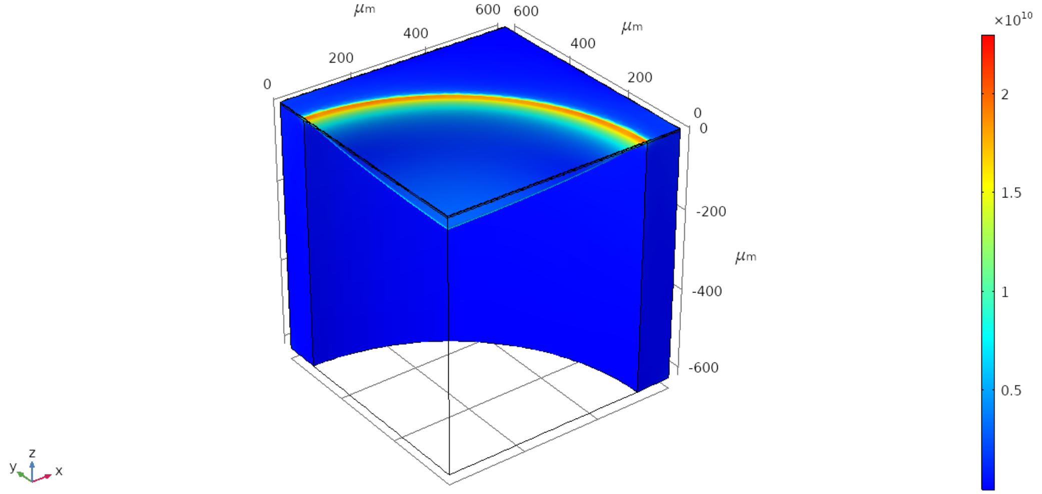

Figure 3.9: Von Mises stress in the membrane, simulated quarter of the device at peak load (1 MPa).

Figure 3.10 shows the stress vs swept pressure values. These data are generated from a cut-point located at the AlGaN/GaN interface, 25 µm into the membrane along the yz. This is the centre of the fabricated 2DEG channel. Note that the orientation of the stresses in this figure match the orientation axes in figure 3.9. As expected, the stress in the z, vertical direction (out of plane) is almost zero. Along the radial direction (x) the stress is minimal. The dominant stress is in the y direction; that is, the stress in the direction to the edge of the membrane. Note the x and y stresses would be swapped over if the cut point was at the edge of the xz plane.

Using the results obtained for the applied stress in the membrane, the stress can be calculated using a modified form of Hooke's law:

$$\sigma_i = \sum_j C_{ij} \varepsilon_i i \tag{3.4}$$

where C_{ij} represents the elastic coefficient matrix of the wurtzite crystal, ϵ_i is the strain, and σ is the stress. Due to the nature of the wurtzite crystal, only the strain tensors in the x,y, and z directions are relevant, and all others are zero.

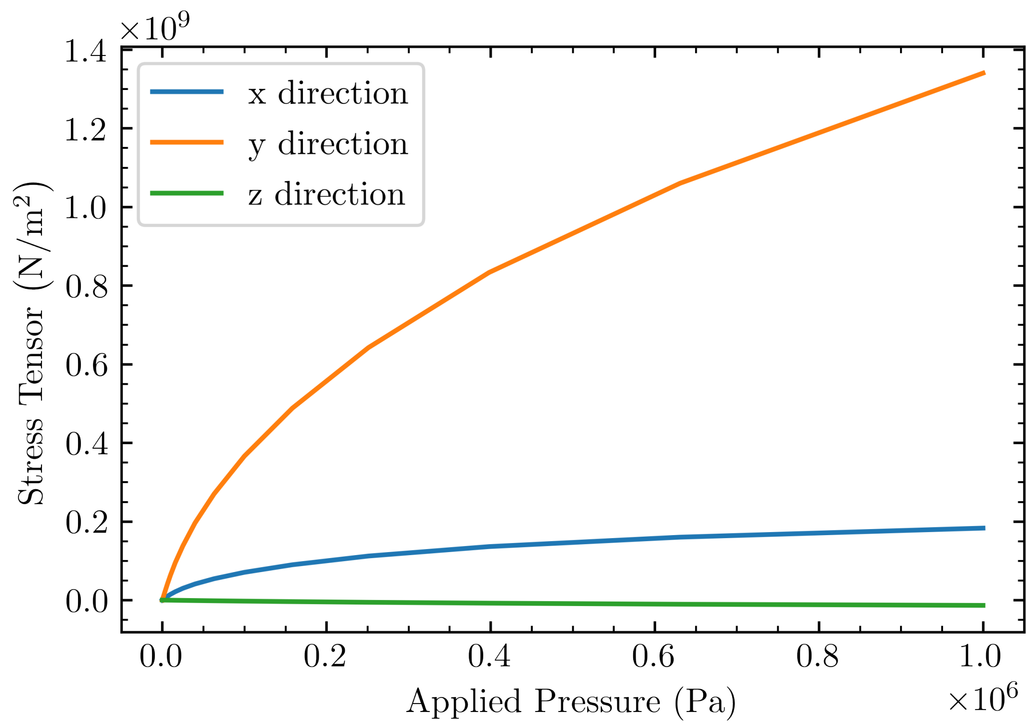

Figure 3.10: Membrane stress tensors in the x, y, and z directions vs applied pressure at the point of peak stress (25 µm from the edge). Orientation is shown on fig. 3.9.

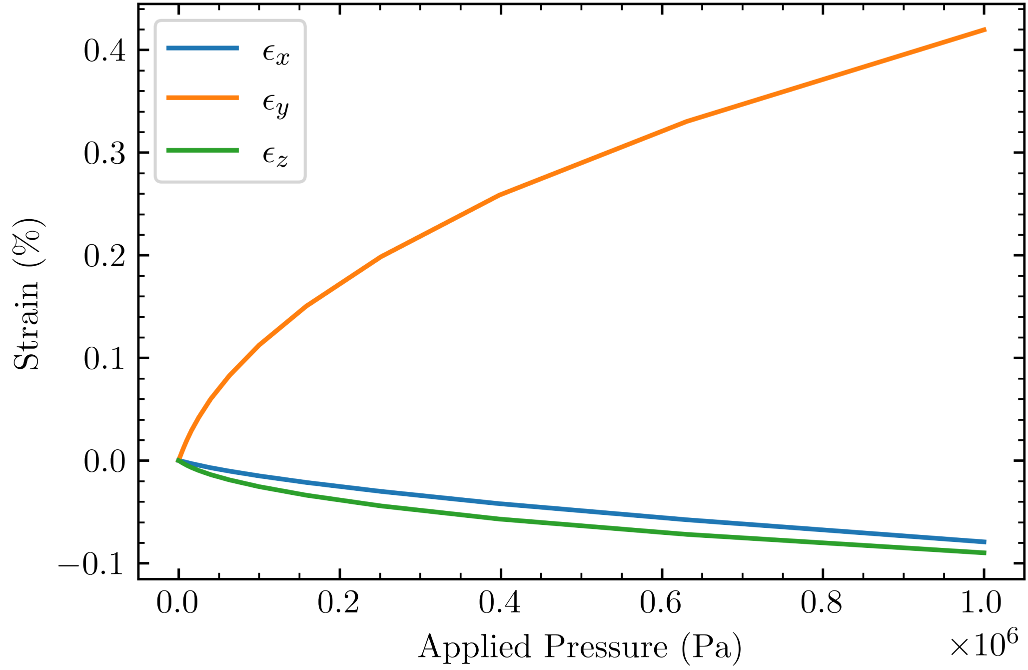

Figure 3.11: Membrane strain in the x, y, and z directions vs applied pressure at the point of peak stress (25 µm from the edge). Orientation is shown on fig. 3.9.

Applying this calculation, gives the strain shown in figure 3.11. This shows that the main direction of strain is in the radial direction (y in the data sets presented here). This strain also behaves in a non-linear fashion after around 20 kPa. According to the literature, cracking can occur in suspended GaN membranes with an applied strain of around 0.2%. This would mean that the membrane could get damaged above 0.25 MPa. Caution should be used when applying this model at strains above this.

With the solid mechanics outputs obtained from the FEM model, further analytical calculations can be performed to understand the electrical behaviour of the device.

3.2.2 Analytical Model

The pressure sensor model is fundamentally based on equation 3.5 below (repeated from chapter 2) where the strain in the 2DEG is related to the output

current via the carrier concentration [2, 98]. It is the P_{tot} term that is relevant to this modelling. This term, as described in chapter 2, includes the spontaneous and piezoelectric polarisations at the AlGaN/GaN interface.

$$n_s(\varepsilon) = \frac{P_{tot}(\varepsilon)}{q} - (\frac{\epsilon_0 \epsilon_{AlGaN}}{q^2 d_{AlGaN}})[\phi_B(AlGaN) - (E_f - E_c)^{\gamma}_{int} - \Delta E_C(\varepsilon)] \quad (3.5)$$

Piezoelectric polarisation of the materials can be calculated with equation 3.6, where $P_{pz,3}$ is the piezoelectric polarisation in the 3 direction (radial), e_{ij} are the piezoelectric coefficients of the material, and ε_i represents the strain in the crystal structure in the x, y, z directions.

$$P_{pz,3} = e_{33}\varepsilon_z + e_{31}(\varepsilon_x + \varepsilon_y) \quad (3.6)$$

There are three principal sources of strain in the HEMT 2DEG: lattice mismatch strain, residual thermal strain, and the applied strain from an external force. All of these sources can be defined as follows.

Lattice Mismatch Strain

As the AlGaN and GaN layers grow, a lattice mismatch strain (ε_1) develops in the hetrostructure. This is true for any alloy grown, such as InAlN or InGaN.

The AlGaN is grown as an epitaxial layer on the GaN layer, which is fully relaxed at the 2DEG interface. The AlGaN on the other hand develops a biaxial lattice mismatch stress, where $\sigma_1 = \sigma_2$, and $\sigma_3 = 0$ [98]. The strains from the lattice mismatch that are developed in the AlGaN layer can be described as:

$$\varepsilon_1^{AlGaN} = \varepsilon_2^{AlGaN} = \frac{a_{GaN} - a_{AlGaN}}{a_{AlGaN}}, \quad \varepsilon_3^{AlGaN} = -2\frac{C_{13}^{AlGaN}}{C_{33}^{AlGaN}}\varepsilon_1^{AlGaN} \quad (3.7)$$

where a_{GaN} and a_{AlGaN} represent the lattice constants for GaN and AlGaN in the 1- and 2- directions (the basal pane). The values of a used in

this model are shown in table 3.2.

Table 3.2: Lattice constants of materials where x is the fraction of Al in the alloy [2].

Property	GaN	AlN	AlGaN
a	3.199	3.110	$3.1986 - 0.086x$
c	5.224	5.079	$5.2262 - 0.2323x$

Residual Thermal Strain

During the fabrication of the AlGaN/GaN device, layers are grown at an elevated temperature, typically around 1300 K in the MOCVD process. Given the difference in the thermal expansion coefficients of the alloy material and the GaN, the layers expand at different rates but when deposited are of the same length. When the wafer is cooled from the growth temperature, T_g, to the ambient, the layers contract at a different rate due to the different thermal expansions. This causes a residual strain in the materials, called the residual thermal strain [98]. The strain at the 2DEG due to the in-plane thermal expansion are:

$$\varepsilon_{1,a}(T) = \varepsilon_{2,a}(T) = \pm \left| \frac{(a^{T_g}_{AlGaN} - a^{T}_{AlGaN}) - (a^{T_g}_{GaN} - a^{T}_{GaN})}{1 + (a^{T_g}_{AlGaN} - a^{T}_{AlGaN})} \right|, \varepsilon_{1,a}(T) = -2\frac{C_{13}}{C_{33}}\varepsilon_{1,a} \tag{3.8}$$

The lattice constants at different temperatures are approximated from experimental data. The lattice constants of AlGaN are smaller than those of GaN, which means that the in-plane strain in the GaN is tensile (positive) and compressive (negative) for the AlGaN [98]. The out of plane (3- direction) residual thermal strain is given by:

$$\varepsilon_{1,c} = \varepsilon_{1,c} = 0, \varepsilon_{1,c}(T) = \frac{c^{T} - c^{T_{ref}}}{c^{T_{ref}}} \tag{3.9}$$

where $T_{ref} = 0$ K and c are the temperature dependent lattice constants of the metals in the 3-direction. The total residual thermal strain is the sum of

the in-plane and out-of-plane components in each material for each direction.

This strain is assumed to be independent of lattice and applied [98].

Applied Strain

This is the strain that comes from external sources, which in the case of this pressure sensor, is the pressure itself. The applied strains in the 2DEG can be described as:

$$\varepsilon_{1,a} = \varepsilon_{2,a} = applied\ biaxial\ strain, \quad \varepsilon_{3,a} = -2\frac{C_{13}}{C_{33}}\varepsilon_{1,a} \tag{3.10}$$

The total strain can be found by summing each of the three components for each direction [98]. This can then be fed into equation 3.5 above view equation 3.6 to get the change in carrier concentration of the 2DEG and thus, the sensor output.

3.2.3 Combined FEM and Analytical Model Results

The stress data obtained from the FEM model were used with the calculations from the analytical model to determine the relative change in the total polarisation due to strain. The data presented in figure 3.11 is inputed to equation 3.10, which is then combined with the other strain sources. This is inputted to equation 3.6 to get the piezoelectric polarisation. This, combined with other strains and the spontaneous polarisation gives the total polarisation at the AlGaN/GaN interface, and is thus related to the 2DEG carrier concentration. Figure 3.12 shows the percentage change in total polarisation with respect to the applied pressure, up to 100 kPa. This degree of change is consistent with other work in the literature on the subject of modelling carrier concentration with respect to pressure [100, 102]. The trend visible here also follows the same trend as the fabricated device in chapter 5.

To go from the change in total carrier concentration to the drain current of the HEMT is not trivial and other factors must be accounted for. This

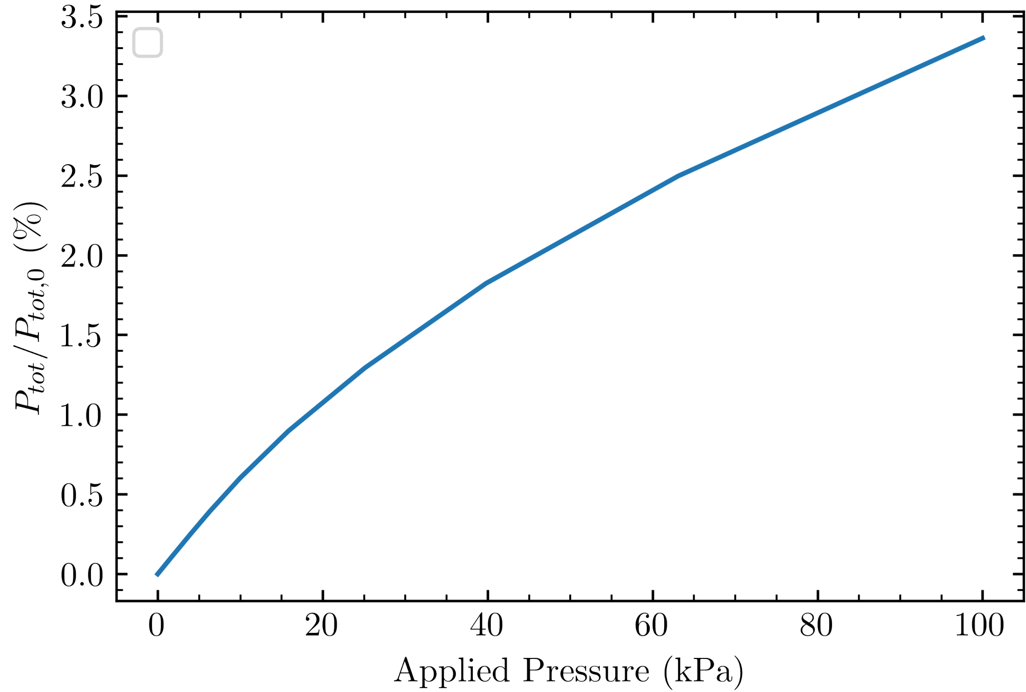

Figure 3.12: Percentage change in total polarisation at the interface with pressure from 0 to 100 kPa.

work does not consider these factors. The drain current can be calculated as in equation 3.11, which introduces the electron drift velocity, $v(r)$, the device width, W, all at a position r in the channel.

$$I_d(r) = qn_s(r)Wv(r) \tag{3.11}$$

The I_d term here is dependent on other factors not captured, such as the gate voltage and changes in the saturation velocity due to the pressure. In addition, work by [2] has shown that the change in the piezoelectric polarisation can impact on factors such as the Schottky barrier height.

3.3 Conclusion

This chapter has discussed the modelling of the devices presented in the remainder of this thesis. The modelling showed that the miniature flow channel

sized at 20 mm will provide a laminar flow certainly up to 1 SLPM and potentially up to a flow rate of 2 SLPM. After this point, the flow profile appears consistent but not necessarily laminar. It may be possible to measure the flow rate above this level, however the flow regime may transition and so it is possible that the sensor output will show a different flow vs output trend during the turbulence regime, not following King's law.

The ring HEMT pressure sensor has been modelled using a combination of FEM and analytical calculations. The FEM model implemented in COMSOL multiphysics determined the stress and strain in the membrane, while the analytical model takes this result and expresses the relationship between pressure and carrier concentration in relative terms.

Chapter 4

GaN on Silicon Flow Sensors - Fabrication and Testing

This chapter presents the novel GaN-on-Si flow sensors. The chapter is split into 2 sections. The first covers a thermoresistive flow sensor with a gold hot-wire, the second presents a novel GaN-on-Si thermoresisitive flow sensor that utilises the 2DEG channel of the AlGaN/GaN heterostructure.

4.1 Thermoresistive Flow Sensors

This section describes a novel thermoresistive GaN-on-Si thermal wall shear stress sensor. Two sensors are reported here, one with a hot-wire made from gold and a second with a hot-wire made from the 2DEG region of the semiconductor. The sensors were fabricated at an academic foundry (Cardiff University). The sensor is tested with a custom 3D printed lid which incorporates a flow chamber, the design of which was discussed in chapter 3.

4.1.1 Introduction

Numerous materials used as the heating or sensing element for anemometric thermal flow sensors have been explored, as well has different methods of achieving thermal isolation of said heater. To the best of the authors knowl-

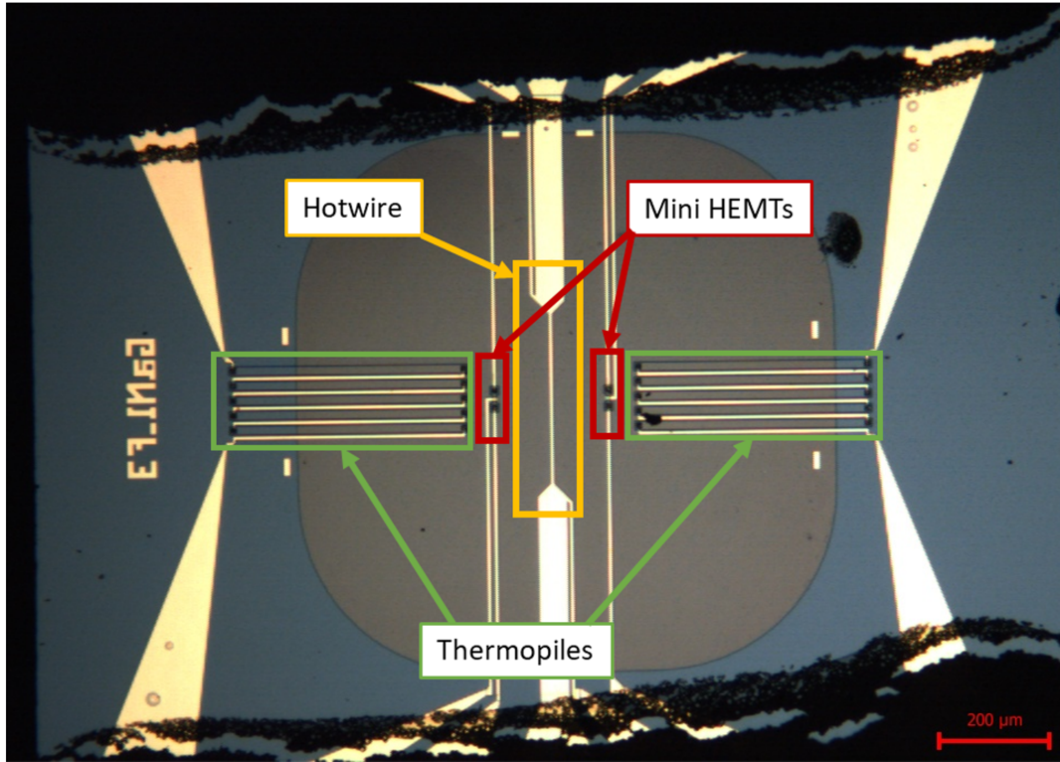

Figure 4.1: Optical Image of the sensor chip, highlighting the main devices; the gold hot-wire, Au/2DEG thermopiles, and mini-HEMT temperature sensors (not discussed in this thesis).

edge, this has never been reported in a GaN process of any kind.

This section proposes a novel thermoresistive anemometric GaN-on-Si thermal flow sensor, with a gold hot-wire and a DRIE membrane release process. Presented here is extensive electro-thermal characterisation and sensor performance to air flow.

4.1.2 Design & Packaging

The sensor was designed with Cadence Virtuoso IC 5.1 layout editor. The chip, includes one 5 µm x 300 µm hot-wire with 4-wire connections along with 2 sets of 2DEG/Au thermopiles, each comprising of 5 2DEG/Au thermocouples in series, as can be seen in figure 4.1. Each thermocouple element is 410 µm in length and 15 µm wide. The hot junction of the thermocouples is located

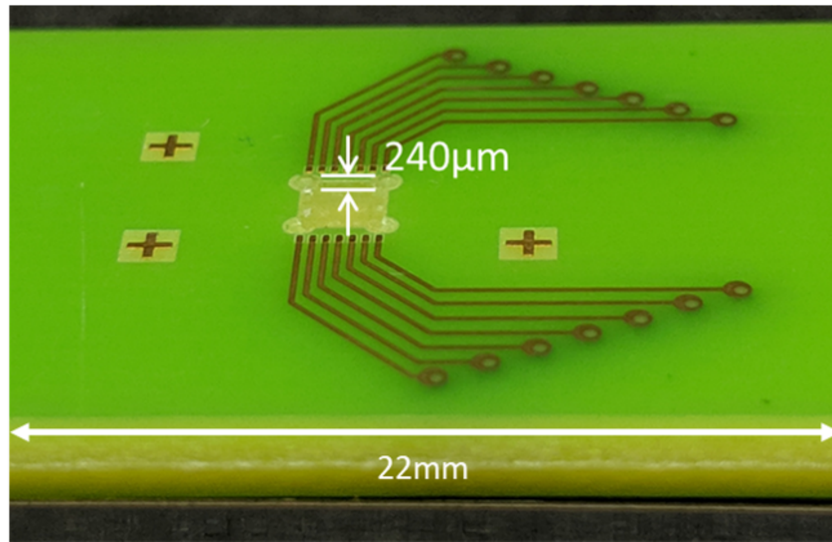

Figure 4.2: Die cavity in the interface PCB package

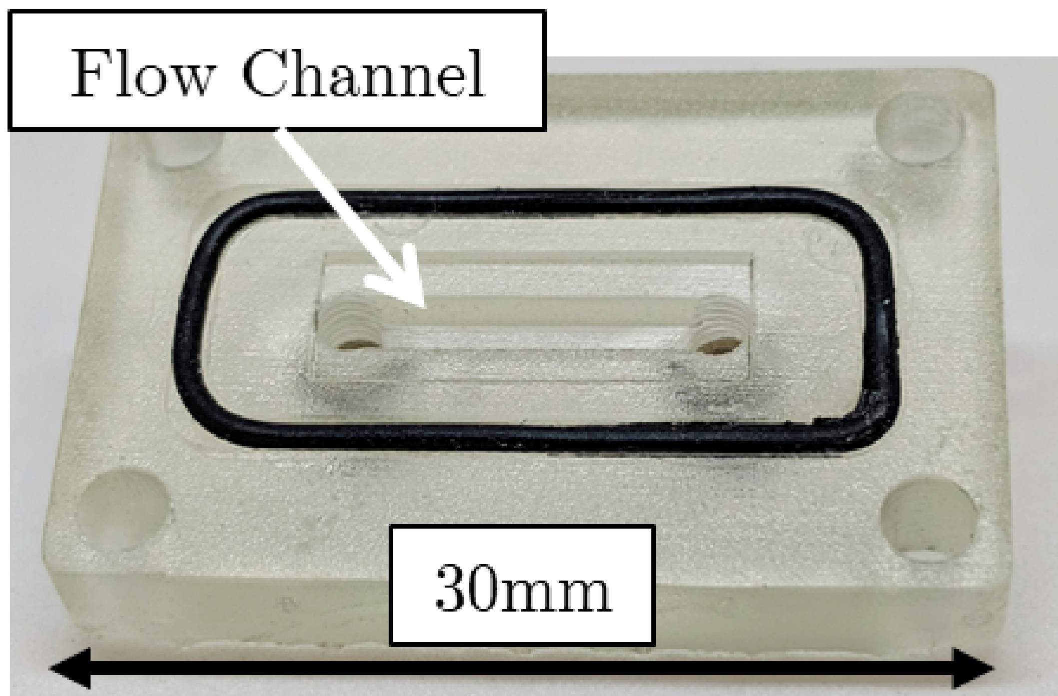

Figure 4.3: The flow channel of the upside-down lid

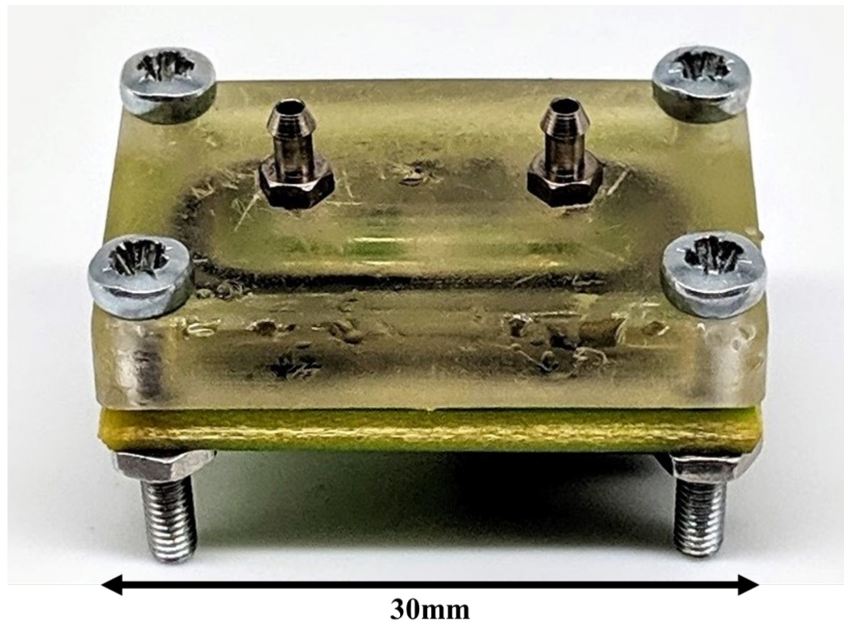

Figure 4.4: Packaged device with flow channel lid

Figure 4.5: Schematic Cross-section of the GaN-on-Si sensor

on the membrane and the reference junction (also known as cold junction) is located on the substrate. The chip also contains HEMT structures in order to use the device in a thermoelectronic configuration. Due to problems with fabrication, these are not presented or tested here. The sensor die is placed and bonded into an engraved cavity on a custom PCB (fig. 4.2). On top of this, a custom 3D printed lid is attached to the PCB which has a duct flow channel with a cross sectional area of 2 mm x 2 mm (fig. 4.3). The hot-wire and thermopiles were connected to bond pads with gold tracks. The hot-wire includes 2 additional tracks in order to measure the resistance more accurately in a 4-wire, Kelvin measurement configuration. The bond pads and bond wires were covered by a cement like material to minimise interference with the flow. The packaged device is shown in figure 4.4

The GaN structure was fabricated on top of a silicon substrate using MOCVD. The membrane was released by DRIE to allow near vertical side-wall's to be achieved, thus reducing chip size. The superior properties of the GaN stack against corrosion meant that the GaN stack itself acts as the etch stop, guaranteeing the etch depth. The device cross-section is shown in figure 4.5. Gold metallization was used. 2" wafers were diced by Disco commercial dicing house and then wedge wire-bonded onto the custom PCBs. The custom PCBs have a cavity to hold the sensor chip which allows the surface of the die is flush to the surface of the PCB. This has the effect of minimising turbulences that would otherwise affect the sensor reading.

4.1.3 Experiment

The initial electro-thermal characteristics of the hot-wire were determined. First, the temperature coefficients of resistance of the hot-wire was extracted using the Cascode Microtech Sumit 12000 Probe station fitted with a thermal chuck (heating and cooling) between 25 and 125. A Keithley 2651A SMU was used to sweep the voltage across the hot-wire while simultaneously measuring the current. Figure 4.6 shows the hot-wire resistance vs chuck temperature. The first order TCR (α) was calculated to be 0.00302 $\%/K$ using $R(T) = R(T_0)[1 + \alpha(T - T_0)]$. This is consistent with the value usually quoted for

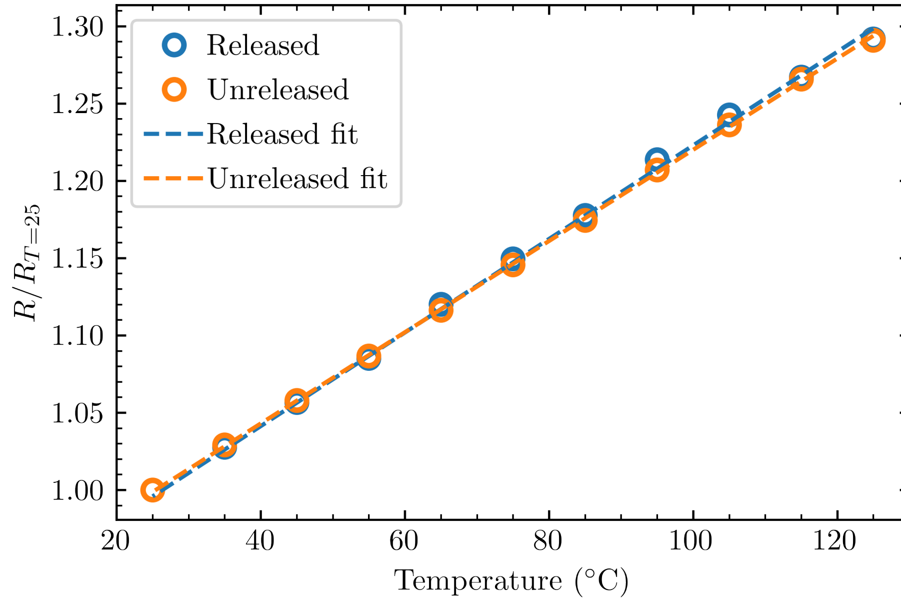

Figure 4.6: TCR Extraction (Resistance at hot-chuck temperature)

gold in a variety of sources. The cold resistance of the gold heater resistor was typically 7.66Ω.

Figure 4.7 shows the mean hot-wire temperature vs its DC power dissipation. The gradient of this is the electrothermal efficiency of the heater, which was measured to be 1.04 K/mW for the membrane device. The same figure shows this for a chip where the membrane has not been released, and the electro-thermal efficiency is 0.21 K/mW. This shows that releasing the membrane improves the electrothermal efficiency by a factor of approximately 5 times.

The PCB with the integrated sensor chip was then packaged with the 3D printed flow channel above. The inlet and outlet of the channel were connected to an automated gas rig, which uses an Alicat MC-5SLPM-D mass flow controller to control the flow rate into the channel and a mass flow meter at the outlet to check for leaks. The Alicat controllers and meters were controlled using a custom Python based software running as a flask server on a Raspberry Pi 3. A Keithley 2621B SMU was used to: (i) drive the hot-wire current, (ii)

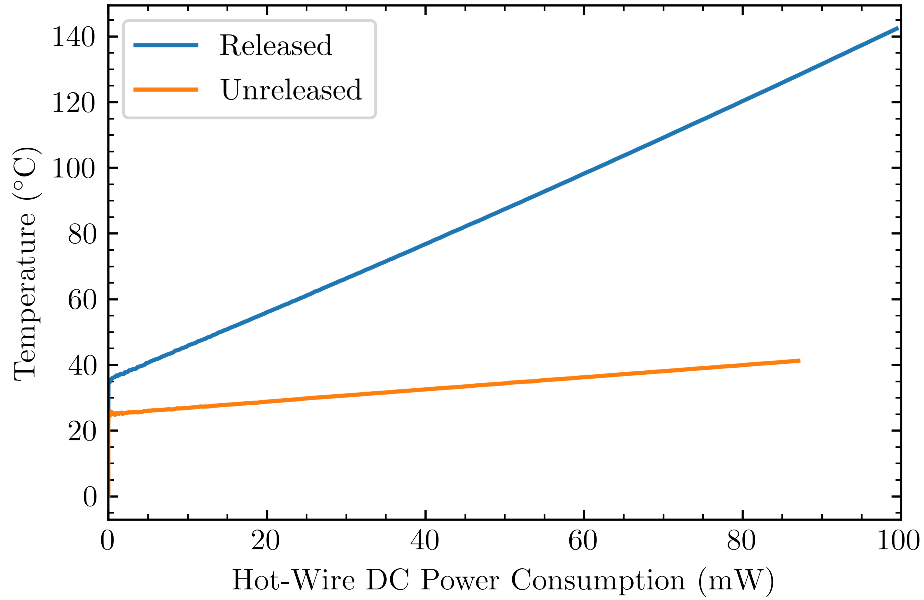

Figure 4.7: Heater power vs heater temperature

measure the voltage drop across the hot-wire in a 4-wire configuration.

The flow rates were increased in steps of 0.1 SLPM from 0 to 4 SLPM and allowed to settle for 60s each step. Data were acquired for each flow rate step at a sampling rate of 5Hz then averaged. The experiment was run with 3 different current values, 87 mA, 95 mA, and 100 mA. These values correspond to the hot-wire temperature in stagnant flow of 150 °C, 200 °C, and 250 °C. Anemometric theory predicts that the sensitivity of the how-wire to flow rate will increase at higher temperatures, at the expense of power consumption. In each case, the sensor output is presented as the change in voltage $V - V_0$ where V is the voltage across the hot-wire and V_0 is the voltage at zero flow.

4.1.4 Discussion

In this section, the aim to investigate the feasibility and the performance the GaN-on-Si flow sensor with a gold hot-wire as a thermoresistor using the anemometric principle. Figure 4.8 shows the sensor output for flow rates from

0 SLPM to 4 SLPM for the 3 different constant current values. This shows that the output response can be improved by increasing the current, however this comes with downsides such as higher DC power consumption and lower reliability due to an electromigration effect. It can be seen that there is a fluidic artefact present at approximately 1.7 SLPM, likely to be an eddy of turbulent air. This indicates that the cooling effect of the forced convection is less at this point. Since this artefact is present for all current values, it can be concluded that it is not the result of sensor itself and due to turbulence in the channel, as is suggested by the modelling in chapter 3. The presence of an eddy at this point could lead to a localised decrease in density of the fluid above the heater, thus the amount of forced convection is lower. This hypothesis is supported by the evidence that the trend of the output changes before this point follows standard anemometer theory and changes afterwards. Despite this, the repeatability of this effect does show that the sensor output can give a reliable indication of the flow rate.

Figure 4.9 shows the sensitivity of the sensor. At the lower flow rates, the non-linearity of the response yields in a high sensitivity of 110 mV/SLPM (T_{HW} = 250 °C). This is a 205 % increase in peak sensitivity compared to the 36 mV/SLPM peak for T_{HW} = 150 °C. This improvement comes with a power penalty, where the peak DC power dissipation of the higher current is 64% higher than that of the lowest current (133 mW and 81 mW, respectively).

4.1.5 Conclusions

In this section, the design, fabrication, packaging, electro-thermal characterisation, and flow sensing calibration of a thermoresistive anenometric GaN-on-Si flow sensor with a gold hot-wire has been presented. The sensor output is valid up to a flow rate of 1.7 SLPM with the 20 mm channel. This proof of concept shows that GaN is a viable material for the fabrication of MEMS shear stress flow sensors, that can be explored further to investigate its feasibility in sensing flow in a harsh environment.

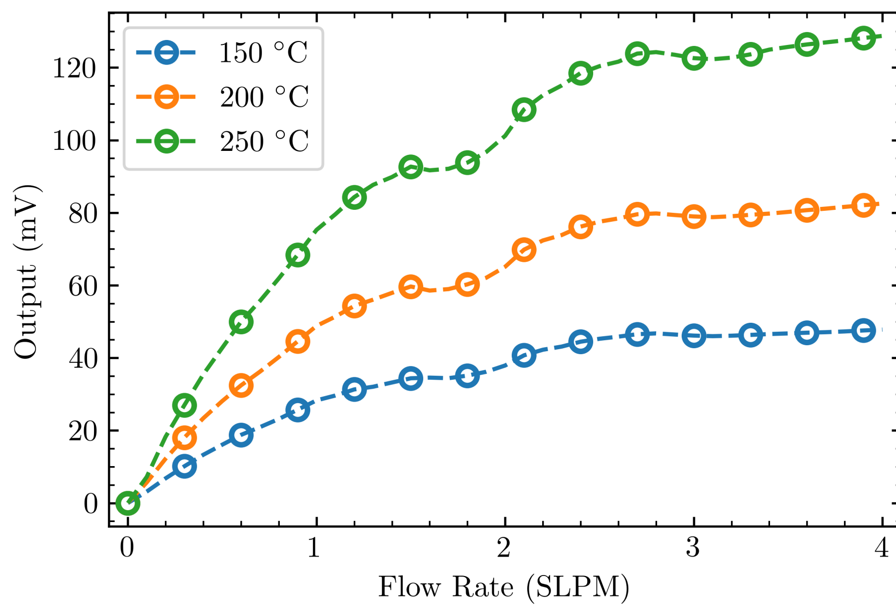

Figure 4.8: Gold sensor output operating in a constant current anemometric mode at various temperatures, where the temperature corresponds to constant current values of 87 mA, 95 mA, and 100 mA for zero flow temperatures of 150 °C, 200 °C, and 250 °C.

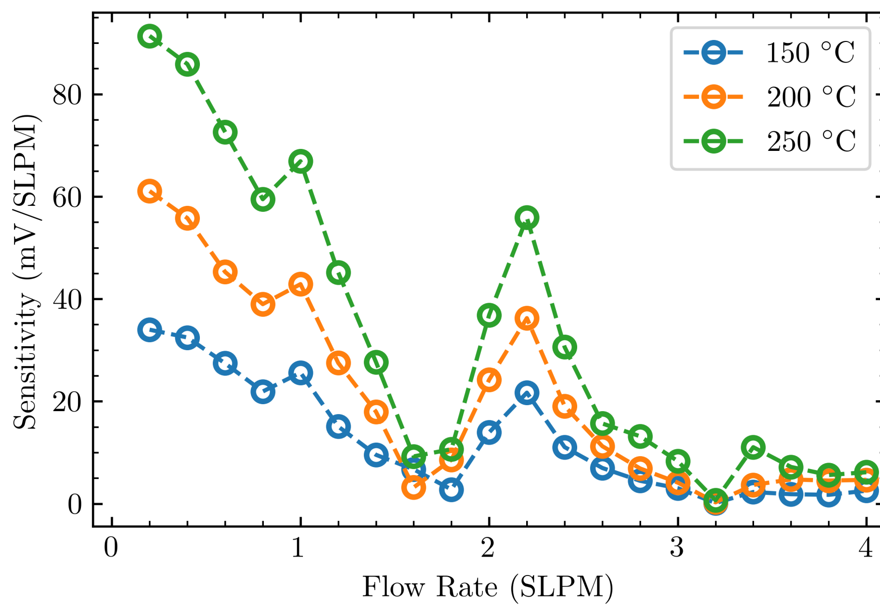

Figure 4.9: Gold sensor sensitivity operating in a constant current anemometric mode at various temperatures, where the temperature corresponds to constant current values of 87 mA, 95 mA, and 100 mA for zero flow temperatures of 150 °C, 200 °C, and 250 °C.

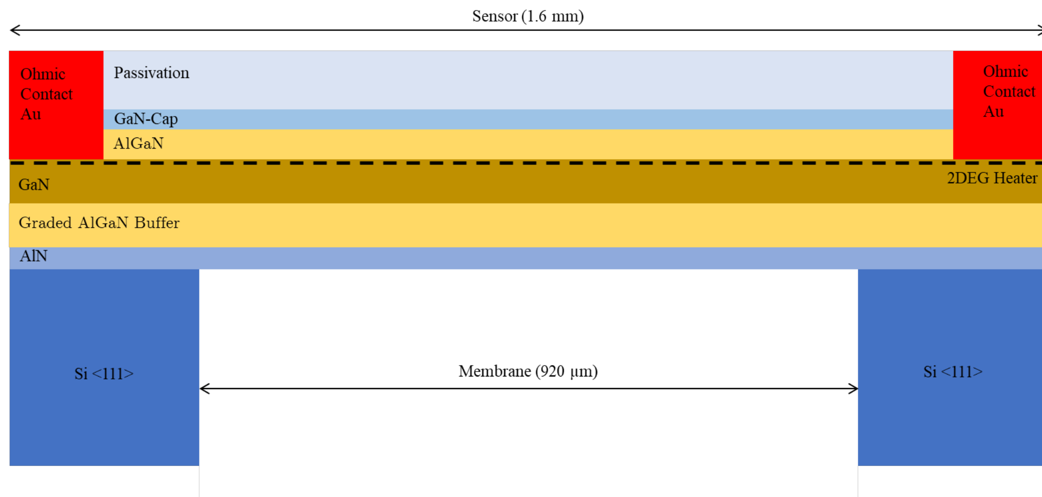

Figure 4.10: Schematic Cross-section of the GaN-on-Si flow sensor with a 2DEG hot-wire.

4.2 2DEG Flow Sensor

This section presents a novel GaN-on-Si thermal wall shear stress sensor that utilises the unique properties of the AlGaN/GaN heterostructure to create a hot-wire of the 2DEG channel.

4.2.1 Introduction

As discussed previously, it is possible to create heterogeneous devices using GaN. In the specific process where a AlGaN/GaN structure is used a 2DEG region is formed. It is known that the mobility of the electrons in the 2DEG vary with temperature and thus, so does the channel resistance. This section presents an anemometric flow sensor that utilizes this property of the 2DEG, and treats it as a hot-wire of increased sensitivity and lower power consumption compared to the gold version. This section discusses the initial electro-thermal characterisation in addition to the performance of the sensor in response to flow.

4.2.2 Design

The sensor was designed with Cadence Virtuoso layout editor. The basic design of the sensor chip is identical to that presented earlier in this chapter. This differs in the hot-wire material. Two version of the 2DEG hot-wire chip were fabricated: (i) a full 2DEG version where all the tracks from the pads and the hot-wire itself are formed as a 2DEG, and (ii) a partial 2DEG design where just the 5 µm x 300 µm hot-wire is made of the 2DEG and ohmic contacts connect the wire to the gold tracks. Issues during fabrication meant that a Schottky contact was formed at the ohmic contact that meant it was not possible to characterise the partial 2DEG devices. The remainder of this section will discuss only the full 2DEG version.

An ohmic contact connects to the 2DEG channel from an extension at the edge of the pads. This 2DEG track continues to a thinner section (5 µm) where the hot-wire resistance is located.

The sensor die was packaged in a custom PCB with a cavity to house the die so that the surface of the die is flush with the surface of the PCB enabling laminar flow. The 3D printed lid with incorporated 2mm x 2mm flow channel was fixed on top of the PCB. The hot-wire was wedge bonded to the PCB and the bonds covered with a ceramic material to protect them from the flow.

The GaN structure was fabricated on top of the silicon substrate using MOCVD and the membrane released with DRIE. The device cross section is shown in figure 4.10. The 2" wafers were diced at a commercial dicing house before packaging.

4.2.3 Experimental

Electrothermal Characterisation

Initially, the electro-thermal characteristics of the hot-wire were discovered. These experiments were done both pre and post dicing. This would determine if the increase in strain present in the full wafer would increase the momentum

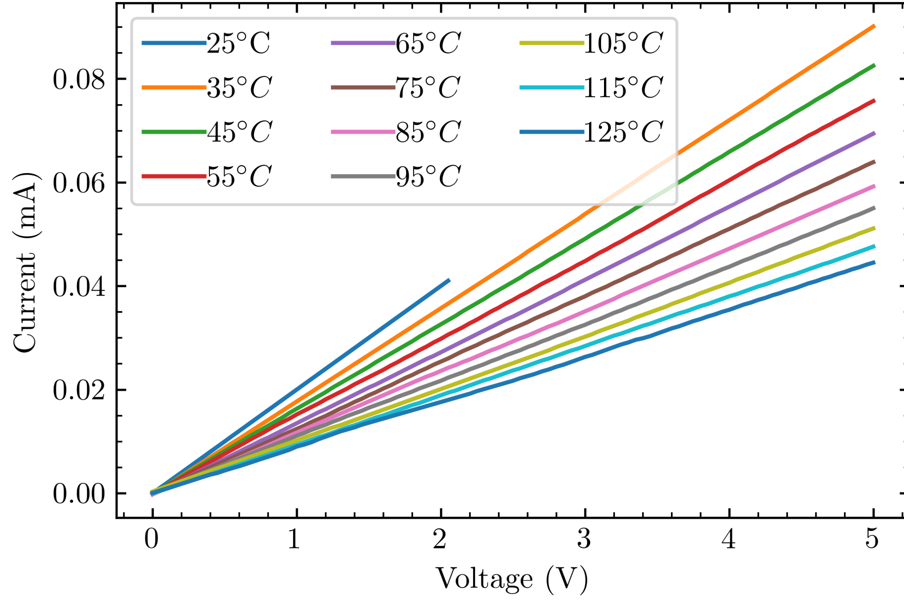

Figure 4.11: I-V characteristics of the 2DEG resistor at various chuck temperatures for the released (membrane) device

of phonons scattering and thus alter the characteristics of the devices.

The temperature coefficients of resistance of the 2DEG were extracted using the Cascode Microtech Sumit 12000 Probe station fitted with a thermal chuck (heating and cooling) between 25 and 125. A Keithley 2651A SMU was used to sweep the voltage and simultaneously measure current. The gradient of the slope of these IV curves gives the 2DEG resistance. This resistance at the different temperatures was plotted and the TCRs determined. Both a linear and second order set of TCRs were obtained. Equation 4.1 shows the second order relationship between resistance and temperature, where α is the first coefficient and β the second. The other terms are the same as in the linear approximation of this relationship.

$$R = R_0[1 + \alpha\Delta T + \beta\Delta T^2] \tag{4.1}$$

Figure 4.13 shows the 2DEG channel resistance vs temperature in absolute terms and figure 4.14 shows the ratio between the resistance at $T = 298$K

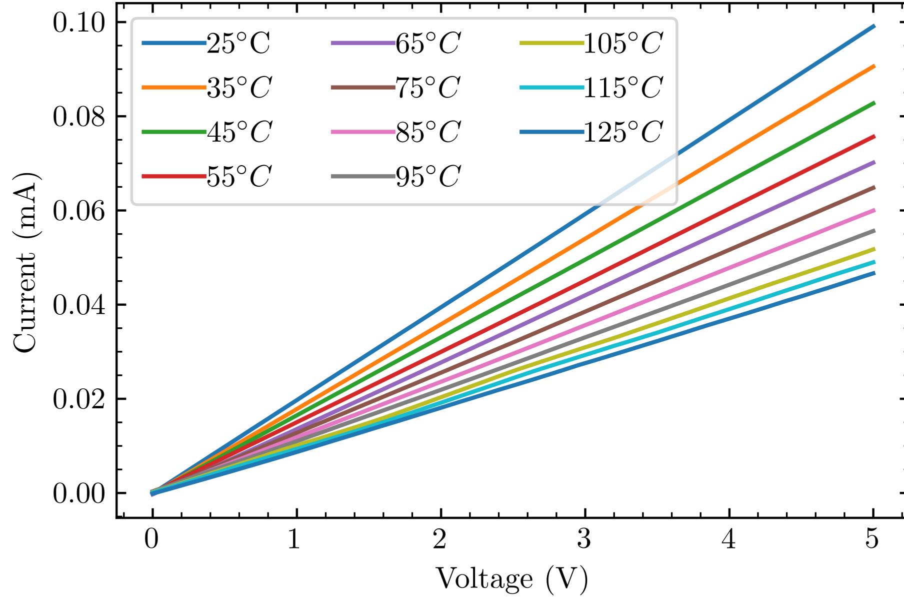

Figure 4.12: I-V characteristics of the 2DEG resistor at various chuck temperatures for the unreleased device

and at the temperature, T. The gradient of this second figure gives us the TCRs. The first order TCR is 0.0114 1/K with an R^2 of 0.996. This shows that the linear approach to calculating resistance from temperature would yield an accurate result. The second order coefficients α and β are 0.00855 and 30x10^{-6}, respectively. While the relationship between 2DEG resistance and temperature is of a second order nature, over the temperature range in this work, the linear approximation is appropriate [103]. Compared to gold, the 2DEG resistor is 2.75 times more sensitive to changes in temperature. This is beneficial for several reasons. First, the 2DEG hot-wire does not need to be driven at as high of a temperature for the same sensitivity as the gold, thus there is less stress from cyclical thermal expansion and less effects from electron migration, thus the life span of the device is improved. Additionally, running at a lower temperature means that the power consumption will be lower for the same sensitivity. Hence there is strong indication that the 2DEG flow sensor will have superior performance to its gold counterpart.

Figure 4.15 shows the hot-wire temperature vs the hot-wire DC power

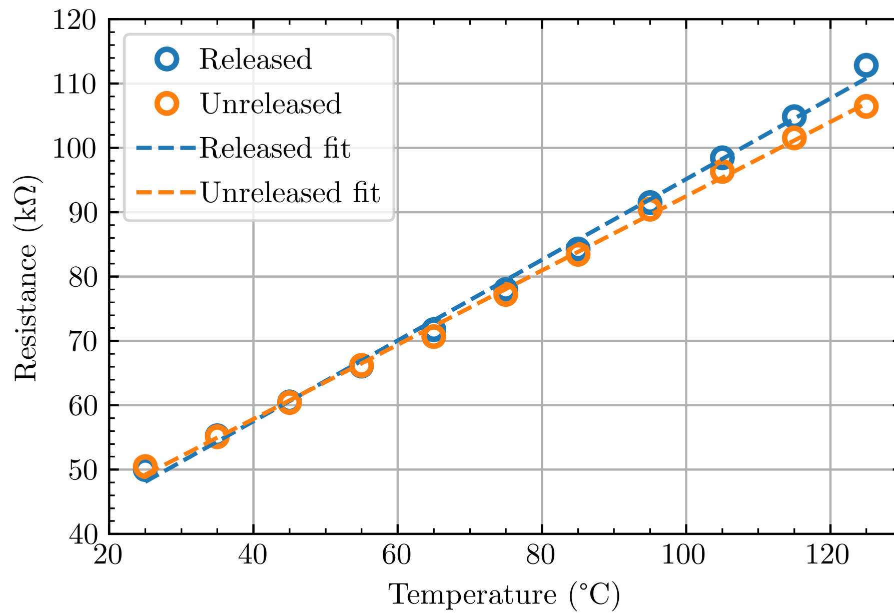

Figure 4.13: 2DEG hot-wire resistance vs chuck temperature for the released and unreleased devices

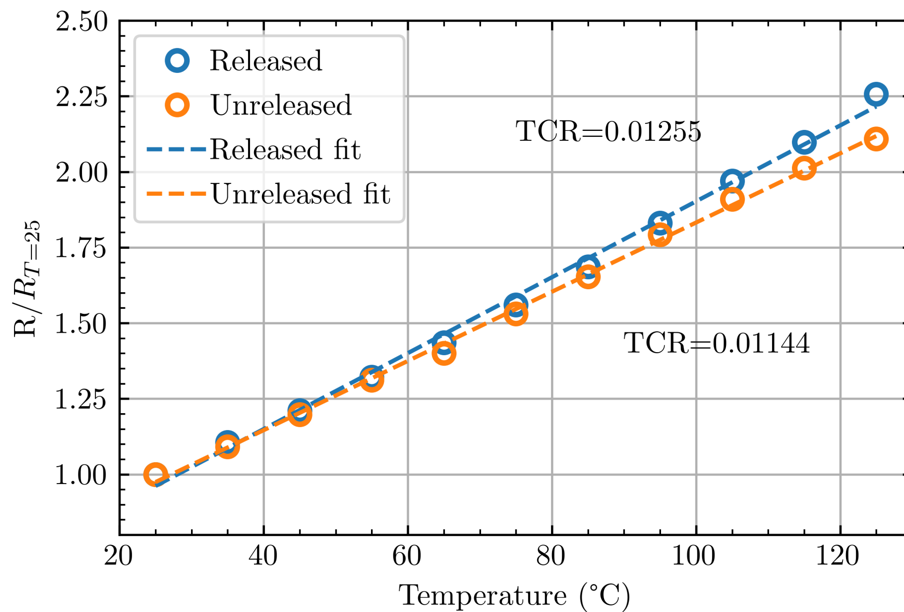

Figure 4.14: TCR extraction (Resistance at hot-chuck temperature)

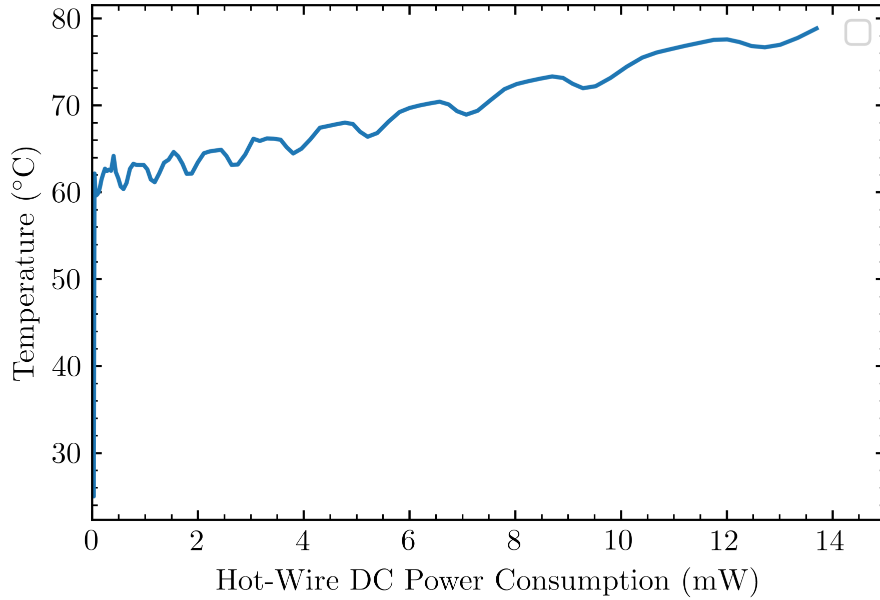

Figure 4.15: Power vs Temperature of the 2DEG hot-wire. Note the self-heating effect causing a fluctuation in the power consumption.

consumption. The gradient of this is the electrothermal efficiency of the 2DEG hot-wire. For the membrane device, this was measured to be 0.9843 K/mW and 0.1663 K/mW. For the membrane device, the electrothermal efficiency is around 5.4% less than that of the gold hot-wire although the bulk device is 20.5% lower, indicating that the 2DEG hot-wire has greater heat lost into the bulk silicon than the gold. This is likely due to the heat source itself being within the layers of the GaN stack as opposed to on the surface.

Calibration

The diced sensor chips were packaged in the PCB and the 3D printed lid with flow channel fixed on top. The experiment set-up uses an Alicat mass flow controller to control the flow into the chamber and a meter at the outlet to detect leakage. The hot wire was driven with a Keithley 2600 series SMU in a DC constant current mode, with the voltage measured in a 4-wire configuration. The maximum current tested was limited by the maximum voltage

output of the SMU (40V), which is around 700 µA. This corresponds to a hot-wire temperature of approximately 80 °C. The flow and the SMU were controlled by a Raspberry Pi using custom control software written in python. The flow rates were increased in steps of 0.1 SLPM from 0 to 4 SLPM, and allowed to settle for 200 s. This is longer than the gold hot-wire device given the additional thermal time constant of the 2DEG hot-wire, due to it being embedded into the thermal mass of the GaN stack. Data were acquired continuously at a sampling rate of 5 Hz then average values during flow steps were obtained in post processing. The flow experiment was repeated for hot-wire drive currents between 0 and 700 µA in steps of 100 µA. The sensor output is presented for each case at the voltage difference between V_0 at zero flow and V at the flow rate.

4.2.4 Discussion

In this section the feasibility and performance of a 2DEG heterojunction channel as a hot-wire for an anemometric flow sensor were investigated. Theoretically, given the increased TCR meaning that the resistance is more sensitive to temperature, this device should have a higher peak sensitivity then the gold hot-wire. The sensor output is higher than that of the gold, meaning that output circuitry should be simpler to implement.

Figure 4.16 shows the output voltage of the device vs flow rate for 6 different hot-wire driving currents. The absolute sensor output voltage is higher than that of the gold. While the mV range that the gold device outputs is high enough to be picked up by standard circuitry, in mechanically harsh environments, where signal noise can be caused by extreme vibrations, the higher absolute output voltage of the 2DEG may have a superior signal to noise ratio. Increasing the current increases the output signal, at the expense of DC power consumption and longevity. This figure also shows the same artefact at 1.7 SLPM as the gold sensor did, supporting the conclusion that this is a fluidic artefact rather than the device itself. Evidently, more investigation needs to be done into the flow channel design before this can be commercially viable.

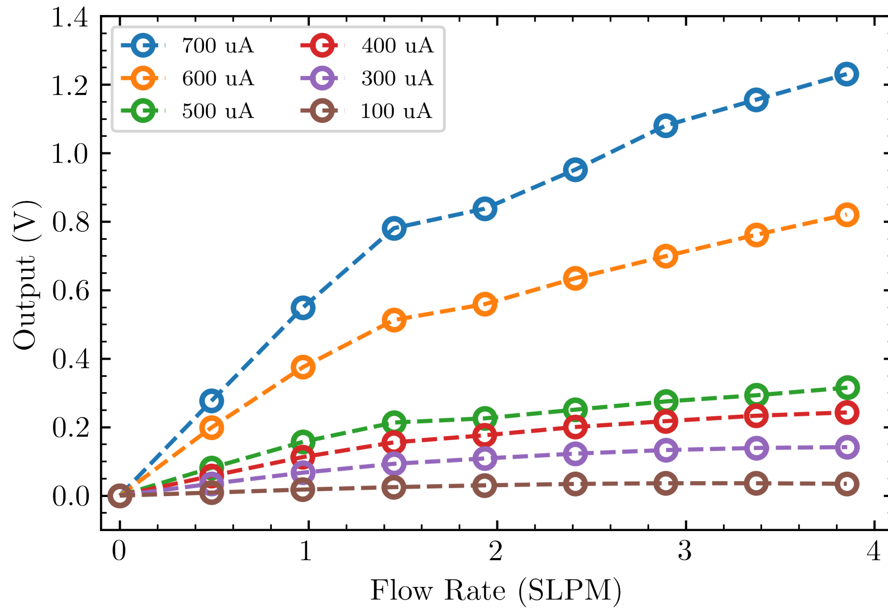

Figure 4.16: Sensor output vs flow rate up to 4 SLPM at various hot-wire currents.

Figure 4.17 shows the sensitivity of the device vs flow rate for the drive currents tested. The peak sensitivity is 569 mV/SLPM for the device operating at 700 µA. There is a substantial jump in sensitivity between 500 µA and 600 µA. For 500 µA and below there is little change with the drive current. Of course, the additional sensitivity needs to be considered in conjunction with increase in DC power consumption, and the problems that come with that.

Figure 4.18 shows the peak sensitivity vs the DC power consumption. This figure supports the conclusions from figure 4.17 in that there is a jump in sensitivity at a certain heater power. When considering the device physics of the 2DEG channel, one can determine that the device is operating in the linear region at the lower powers and then in saturation mode past 500 µA. Thus it is possible to make the claim that the sensitivity of the 2DEG hot-wire to flow is greater in the saturation region than in the linear.

Figure 4.19 shows the output of the 2DEG flow sensor vs flow rate under a low flow regime (0-1 SLPM, steps of 0.1 SLPM). For the higher drive currents

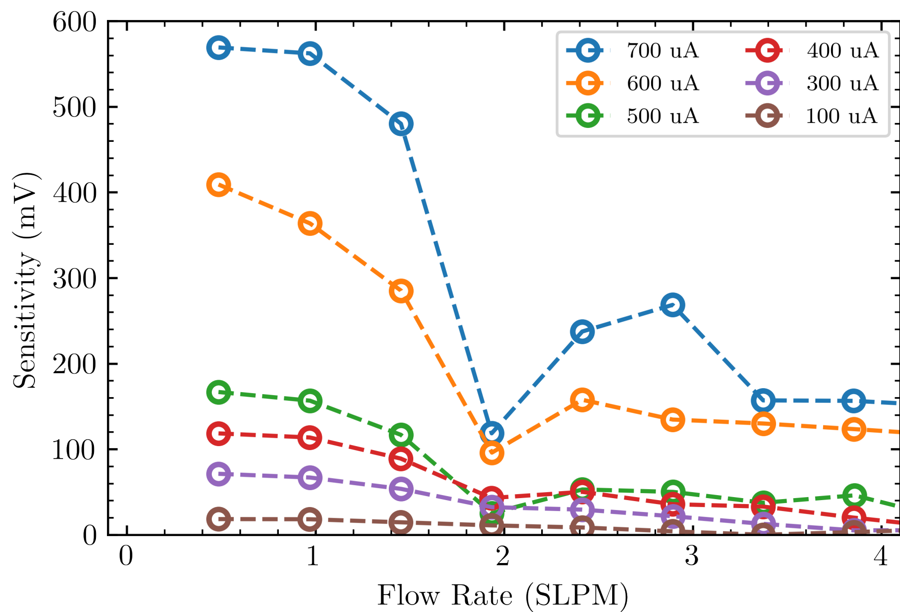

Figure 4.17: Sensor sensitivity vs flow rate up to 4 SLPM at various hot-wire currents.

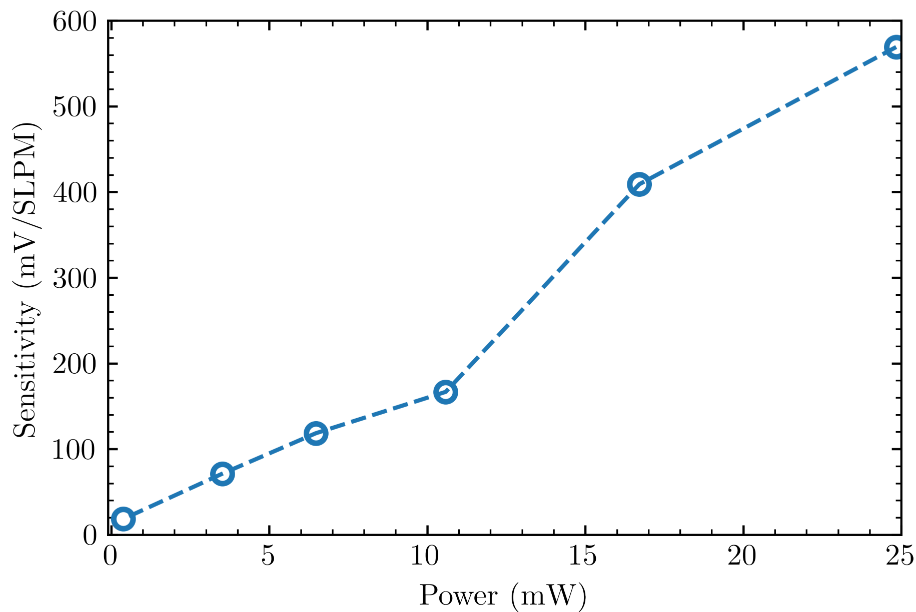

Figure 4.18: Hot-wire DC power consumption vs sensitivity.

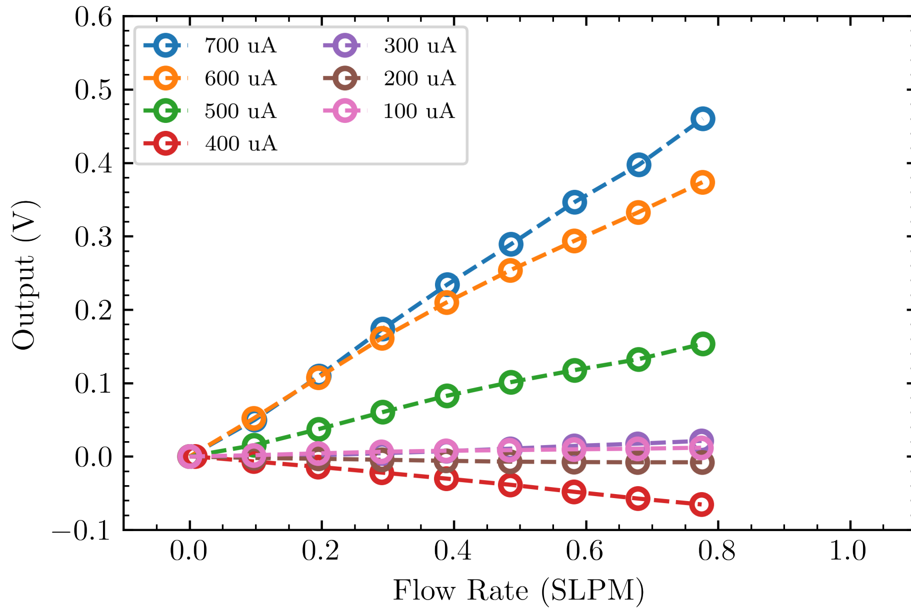

Figure 4.19: Sensor output vs flow rate up to 1 SLPM at various hot-wire currents.

(500 µA, 600 µA and 700 µA), this shows agreement with outputs recorded in the high flow. This is not true for the lower currents. For the forced convection to be effective, the temperature of the heated body, in this case the 2DEG hot wire, need to be above the temperature of the fluid in which the heat is transferring into. At these low currents, the hot-wire temperature is not sufficiently high enough for the effects of forced convection to be detected at the lower flow rates. This figure does show that the 2DEG hot-wire is capable of detecting flow rates as low as 0.1 SLPM.

4.2.5 Conclusions

In this subsection, a GaN-on-Si anemotetric flow sensor was reported that uses a 2DEG formed at the heterojunction between GaN and AlGaN layers as a hot-wire, suspended on a GaN membrane. Suspending the 2DEG hot-wire on a membrane formed of the GaN stack offered an electrothermal efficiency of 0.9843 K/mW. This is compared to an efficiency of 0.1663 K/mW for the

unreleased device.

The TCR of the 2DEG was measured experimentally to be 0.0114 %/K. This is a 275% increase in sensitivity compared to that of the gold hot-wire reported earlier in this chapter.

The limiting factor in determining the maximum operating temperature of the device was the power supply instrument. Due to the high absolute resistance (50 kΩ), the maximum temperature that was tested (72 °C), was limited by the maximum voltage output of the SMU (40 V). This temperature could be pushed higher although this requires some practical considerations about drive circuitry, which would limit the application of the device. Despite this limitation, the device was calibrated and showed a peak sensitivity of 569 mV/SLPM with a DC power consumption of 25 mW. The device was also calibrated in a low flow regime, which shows a resolution of 0.1 SLPM. Though this is not a limit and could be tested further.

Compared to a gold hot-wire, the section has shown that a 2DEG as a hot-wire results in an increased sensitivity to flow at a lower DC power consumption. Driving the heater at a higher temperature would be possible and would increase sensitivity although the high voltage required to do so would make the device less practical.

4.3 Comparison between devices

The electro thermal characterisation showed that both the gold and 2DEG devices have a similar electrothermal efficiency and a similar advantage between an unreleased and released membrane. The benefit of the 2DEG is shown in the TCR extraction, where the 2DEG's 0.0114 %/K makes the change in resistance due to temperature 275% more sensitive than the gold device.

In the operation of the respective devices, the additional sensitivity of the 2DEG resistance to temperature is translated into better sensitivity to fluid flow. The peak sensitivity of the 2DEG device is 417% higher than that of the gold device (100 mA heater current), with power consumption 81% lower.

Comparisons between devices in literature are difficult since often sensitivity is not reported in absolute values and where these are reported, the reported units are non standard. There is a device reported by Sabate [165], which demonstrates a calorimetric flow sensor operating at different flow rate ranges. In the 0-0.1 SLPM range, they achieved a mean sensitivity of 40 mV/SLPM, while in a comparable range to the devices presented here (0.1-2.0 SLPM), their device showed a mean sensitivity of 2.1 mV/SLPM. Between 0 and 1 SLPM, the gold hot-wire device has a mean sensitivity of 48.8 mV/SLPM at 200 °C and 28.3 mV/SLPM at 150 °C. This shows that the least sensitive device reported in this thesis is more than ten times as sensitive as this reported in literature.

The lack of power consumption reported by Sabate makes it difficult to compare the proportionality of the benefit. As table 2.4 shows, the power consumption of thermal flow sensors can vary considerably. Despite this, it can be said that of the devices presented in this chapter, the peak power consumption is at the lower end of the range.

The SOI device presented by De Luca et al. in [179] shows a thermoelectonic flow sensor that uses a diode as a temperature sensor with a hot-wire at 150°C. The sensitivity of this diode is -1.3 mV/°C with a power consumption of 17.99 mW. After converting the sensitivity of the work in this thesis into mV/°C, the mean sensitivity of the 2DEG device, measured between zero and 1 SLPM, is 434mV/°C with a DC power consumption of 25 mW. Despite this being superior to the SOI device, one has to consider the higher biasing voltage required for this (40 V), which may make it difficult to integrate into a system. This comparison is significant since SOI is a contender for high temperature applications up to 300 °C. This proves that the GaN devices are capable of providing the same sensing performance at high temperature as existing devices in this space. While the sensor response is sufficient, the relatively immature scale fabrication processes drive the cost of GaN high compared to CMOS and SOI, and the wafer yields are not as high.

4.4 Conclusions

This chapter has demonstrated for the first time a GaN-on-Si flow sensor. Two types of GaN-on-Si flow sensor are presented here. The first uses a gold hot-wire which showed a sensitivity comparable and superior to that of existing MEMS sensors. In addition, the temperature dependent resistance of a 2DEG can be used to create a thermal flow sensor that is more sensitive than the gold device with much lower power consumption. This device offers higher sensitivity at a lower power consumption than some of the devices previously reported in silicon.

Chapter 5

GaN HEMT Pressure Sensor - Fabrication and Testing

This section discusses a pressure sensor which utilises the strong piezoelectric dependence of the sheet carrier concentration of the 2DEG region of a HEMT. This uses a Circular HEMT (C-HEMT) design, where the HEMT is ring shaped and embedded in the edge of a membrane.

5.1 Introduction

Pressure sensors can be based on numerous different transduction mechanisms. Here, an AlGaN/GaN ring-HEMT membrane based pressure sensor is presented. As discussed earlier in this thesis, the carrier concentration in the 2DEG of AlGaN/GaN HEMT devices have a strong dependency on both the spontaneous and piezoelectric polarisation. The piezoelectric component of the polarisation is dependent on the strain at the interface between the GaN and the AlGaN layers. The device presented here exploits this relationship. When a pressure is applied to the top of the device, the membrane deforms which induces strain into the structure. A HEMT implanted into this membrane is able to detect this induced strain.

5.2 Design & Packaging

The 2DEG channel of the HEMT is embedded into the edge of a membrane that is 500 µm in radius. The gate is located in the centre of the 2DEG channel with the source and drain either side. As the distance between the gate and the source is equal to the distance from the gate to the drain, both sides are interchangeable. For consistency, this thesis will refer to the membrane side as the drain and the one closest to the bulk as the source.

The HEMT gate length is 20 µm, which is the annulus radius of the ring HEMT, and the device width is just shorter than the circumference of the membrane, at 2.52 mm.The 2DEG channel extends for 50 µm from the edge of the membrane. This is where the effects of the pressure induced strain are greatest and thus where pressure will have the greatest impact on the carrier concentration of the 2DEG. The modelling presented in chapter 3 was used to determine this placement. Figure 5.1 shows a schematic with these dimensions.

The GaN structure was fabricated on top of the silicon substrate using MOCVD. DRIE was used to release the membrane. This enabled near vertical walls to be formed, which is good for structural integrity of the membrane and helps in minimising the chip area. Figure 5.2 shows the cross section of the device, with an axis of rotation on the right hand side (not to scale). The contacts and tracks were formed using gold metallization. The 2" square wafers were diced in a commercial dicing house before being packaged into the same PCB as the flow sensor. An important feature of the PCB for the pressure sensor is a hole located underneath the sensor chip in the cavity. This acts to fix the reference pressure of the sensor to atmospheric pressure. It would theoretically be possible to package the chip in a gauge pressure configuration by sealing the hole and controlling the pressure below the sensor during the packaging process. This does bring its own problems by increasing the likelihood of the membrane breaking during packaging. The same chamber as described in the previous chapter was used as the pressure chamber attached to the top of the PCB.

In general, the fabrication was successful, however there were some instances of poor mask alignment, the result of which is that the 2DEG is not

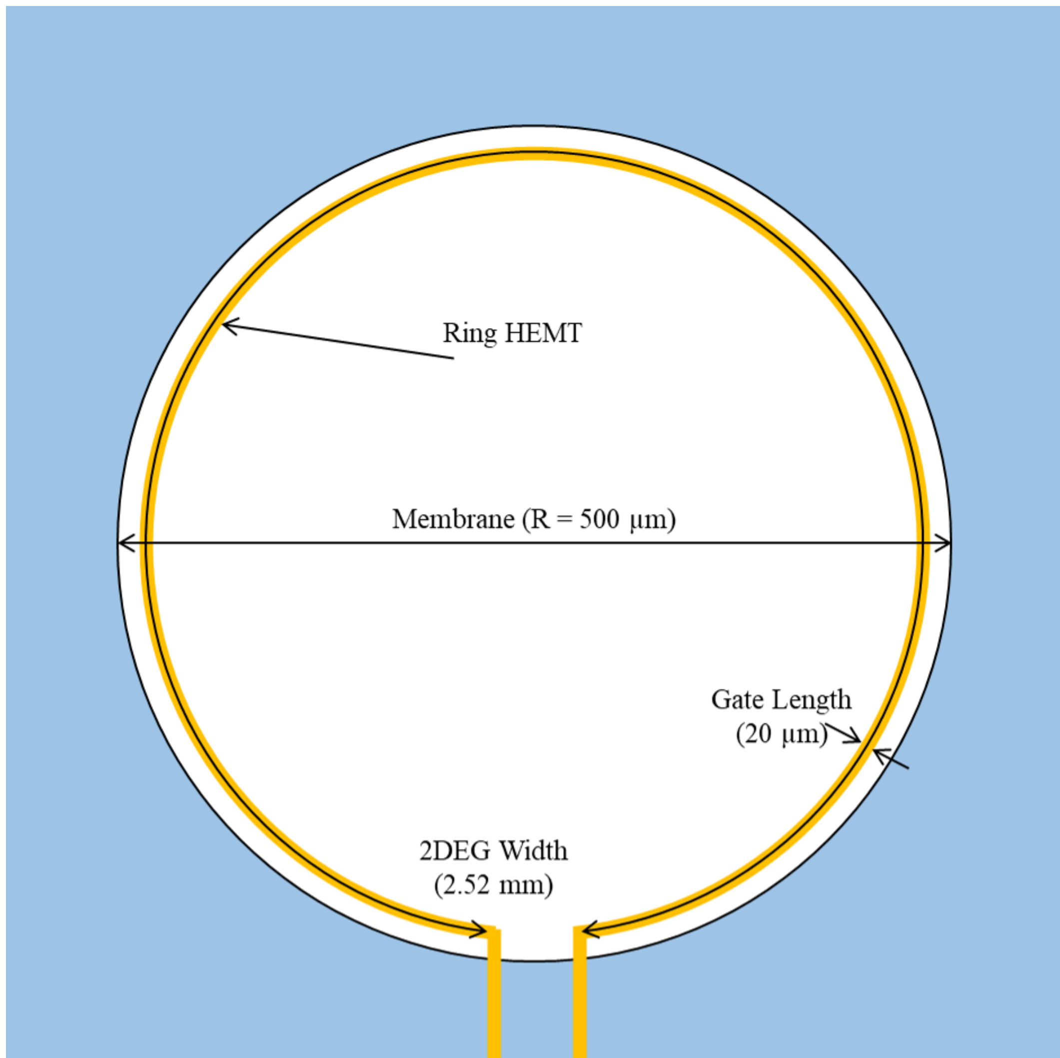

Figure 5.1: Top down schematic of the ring HEMT pressure sensor showing dimensions.

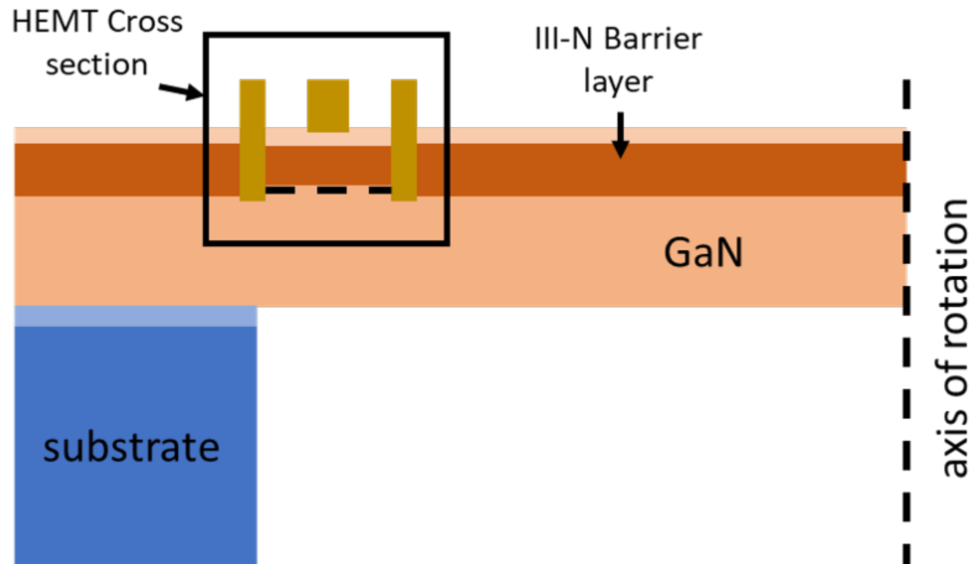

Figure 5.2: Device cross-section with HEMT structure highlighted.

on the membrane at some places around the circumference and thus will not detect any strain. See figure 5.3 that shows this.

5.3 Experimental

The sensor dies were characterised on a Cascode Microtech probe station using two Keithley 2651A SMUs. The purpose of this was to determine the electrical performance of the devices at ambient pressure. An automated test program was created within the Keithley software with 5 individual characterisation tests, as detailed in table 5.1.

Electrical Characterisation

Figure 5.4 shows the transfer characteristics of the ring HEMT, that is, the drain and gate currents vs the gate voltage. The HEMT performs as one would expect over the gate voltage range, where the device has a threshold voltage of $-2.3\,\mathrm{V}$ and the transconductance remains stable in the on region. Generally, the devices characterised have the same characteristics, although there is variance in the peak transconductance. This is shown on the figure by

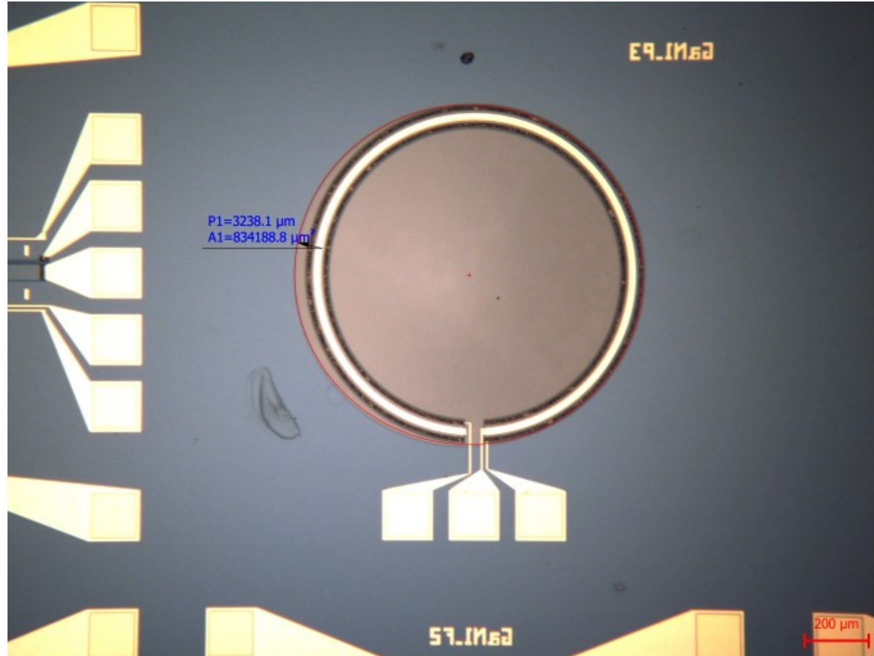

Figure 5.3: Poor alignment on ring-HEMT device.

the shaded areas around the mean measurement. The gate leakage is negligible up to around $V_{GS} = 1\,\mathrm{V}$. After this point, the leakage increases rapidly, which is due to the turn on of the Schottky diode at the Schottky contact.

Figure 5.5 shows the output characteristics of drain current vs drain voltage at 3 different gate voltages. In the linear region, the three curves match closely. After approximately 1.3 V, all three curves enter the saturation region. The output values here closely match the expected outputs taken from the transfer function.

Figure 5.6 show the characteristics of the device in a gate diode configuration. That is, it shows the diode I-V characteristics of the Schottky contact at the gate where the gate terminal is connected to a voltage source, and both the source and drain terminals are connected to ground. This chart is consistent with the typical characteristics of a Schottky diode I-V curve.

In figures 5.4 and 5.6, the curve itself shows the average performance of the HEMT. The shaded area either side shows the distribution of the curves as measured from duplicated devices, where non typical devices have been removed. Out of a total of 16 ring-HEMT structures, this distribution contains

the 7 devices which showed a typical characteristic.

Table 5.1: HEMT Characterisation tests

Test	Output	Description
Output 5 V	3x I-V curves with V_{ds} from 0-5 V	Sweeps V_{ds} from 0-5 V. This is done once for each of 3 V_g values (+1 V, 0 V, -1 V)
Transfer Function	I-V plot of I_d vs V_{GS}	Sweeps V_{GS} from -7 V to +2 V with V_{DS} fixed at 1 V
Gate Diode	I-V plot of I_d and I_g vs V_{GS}	Similar to transfer function but with HEMT configured as a diode.
Hyst 3 V	I_s vs V_{DS} plot	Sweeps V_{DS} from -3 V to +3 V with a floating gate. HEMT configured as a resistor.
Output 5 V Repeatability	3x I-V curves of V_{DS} from 0-5 V	Sweeps V_{DS} from 0-5V with V_{GS} kept constant

Calibration

The packaged devices were attached to a gas rig that uses mass flow controller (MFC) to control the flow of zero-air through the chamber. A flow restrictor was placed at the outlet of the rig in order to allow the pressure to build up in the rig. The MFCs were configured to use pressure as the set point instead of flow. The devices were tested in a relatively low pressure regime from 0 to 100 kPa (gauge) in steps of 10 kPa.

Custom circuitry was used to measure the drain current of the HEMT while running in a drain-source voltage mode. The custom circuitry was interfaced using National Instruments Lab-view v17 and the NI-6368-USB data acquisition unit at a 5 Hz sampling rate. The experiment was repeated for 3 different gate voltage values (-1 V, 0 V and 1 V) and at 3 different drain-source voltages (1 V, 3 V and 5 V). These drain voltage values cover device operation in the linear and saturation region.

The output data were processed so that the output voltage is the change in mean signal over the settling period compared to the signal at 100 kPa.

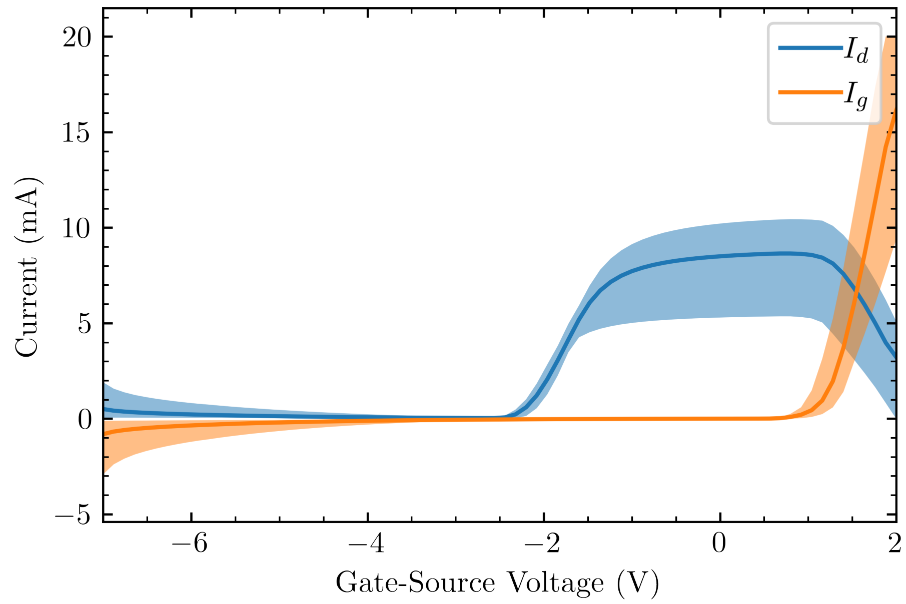

Figure 5.4: Transfer characteristics of the ring HEMT where the shading represents the range of the response of the devices tested.

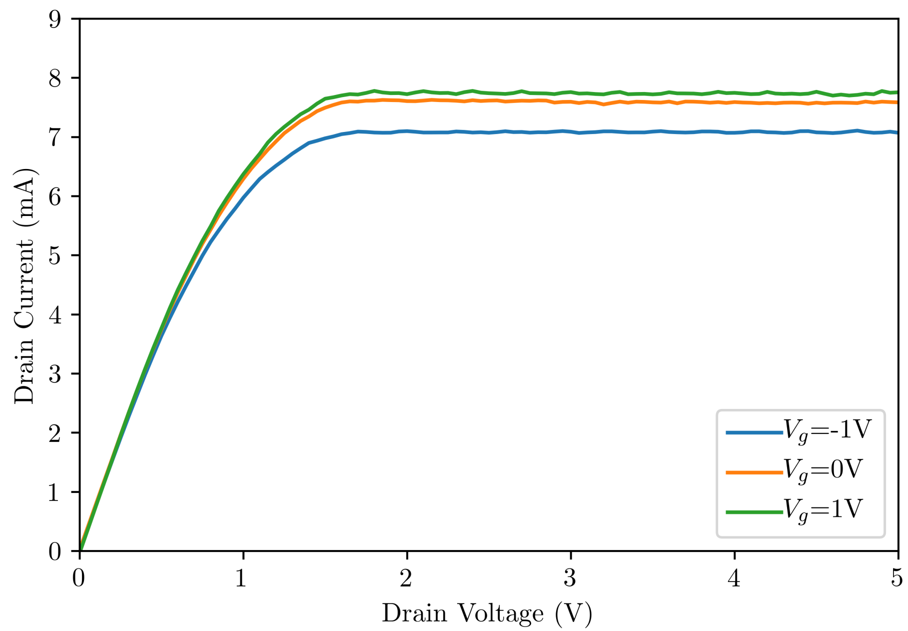

Figure 5.5: Output characteristics of the ring HEMT.

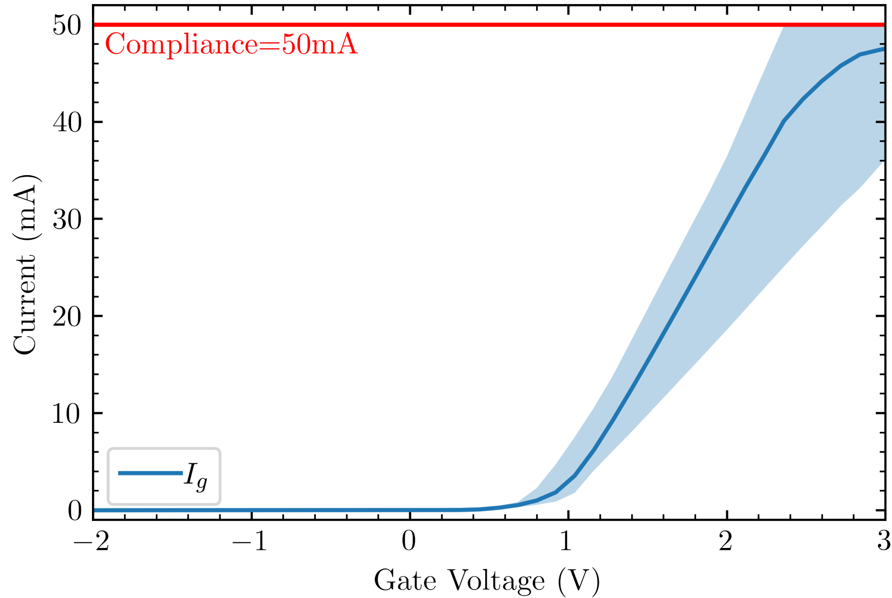

Figure 5.6: Gate Diode I-V characteristics of the ring HEMT where the shading represents the range of the response of the devices tested.

5.3.1 Discussion

Figure 5.7 shows the output and sensitivity of the sensor vs pressure at various V_{DS} values. As was seen from the transfer function, at $V_{GS} = 0$ V the HEMT is fully on. At $V_{DS} = 5$ V, which is the saturation region of the HEMT, the peak sensitivity is about 25 µA/kPa. This is substantially higher than the peak sensitivity in the linear region ($V_{DS} = 1$ V), which is less than 1 µA/kPa, and would present challenges in designing higher gain readout circuitry. The peak sensitivity when $V_{DS} = 3$ V is 8 µA/kPa, which is around a third of the sensitivity at $V_{DS} = 5$ V. This does however, lower the DC power consumption of the sensor.

Figure 5.9 shows the sensor output and sensitivity vs pressure at different levels of V_{DS} when the gate voltage is 1 V. From looking at the transfer function in figure 5.4, the transistor has a slightly higher transconductance than at $V_{GS} = 0V$ meaning that the sensitivity to pressure will be increased. This is confirmed by the observations here, where the peak sensi-

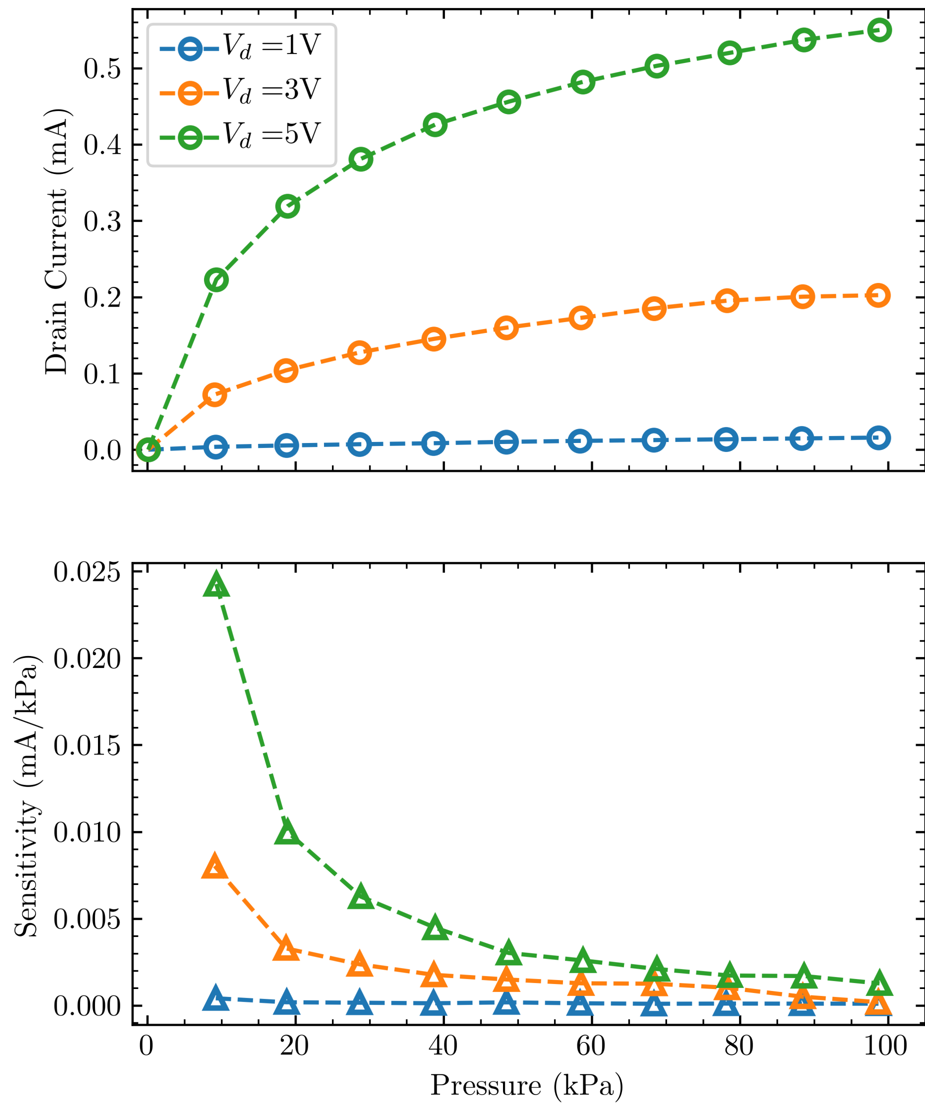

Figure 5.7: Current vs Pressure where $V_{GS} = 0V$ and V_{DS} set to various levels

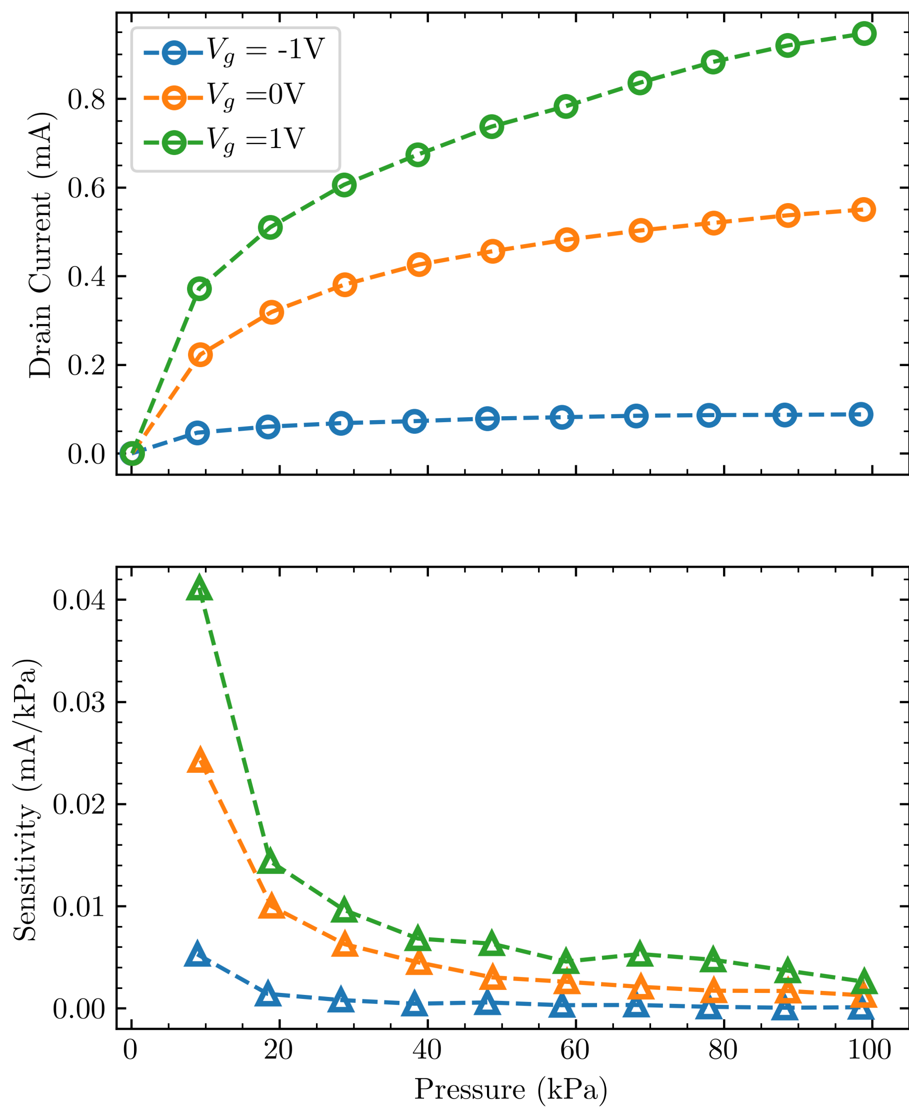

Figure 5.8: Current vs Pressure where V_{DS} =+5V (saturation) and V_{GS} set to different levels

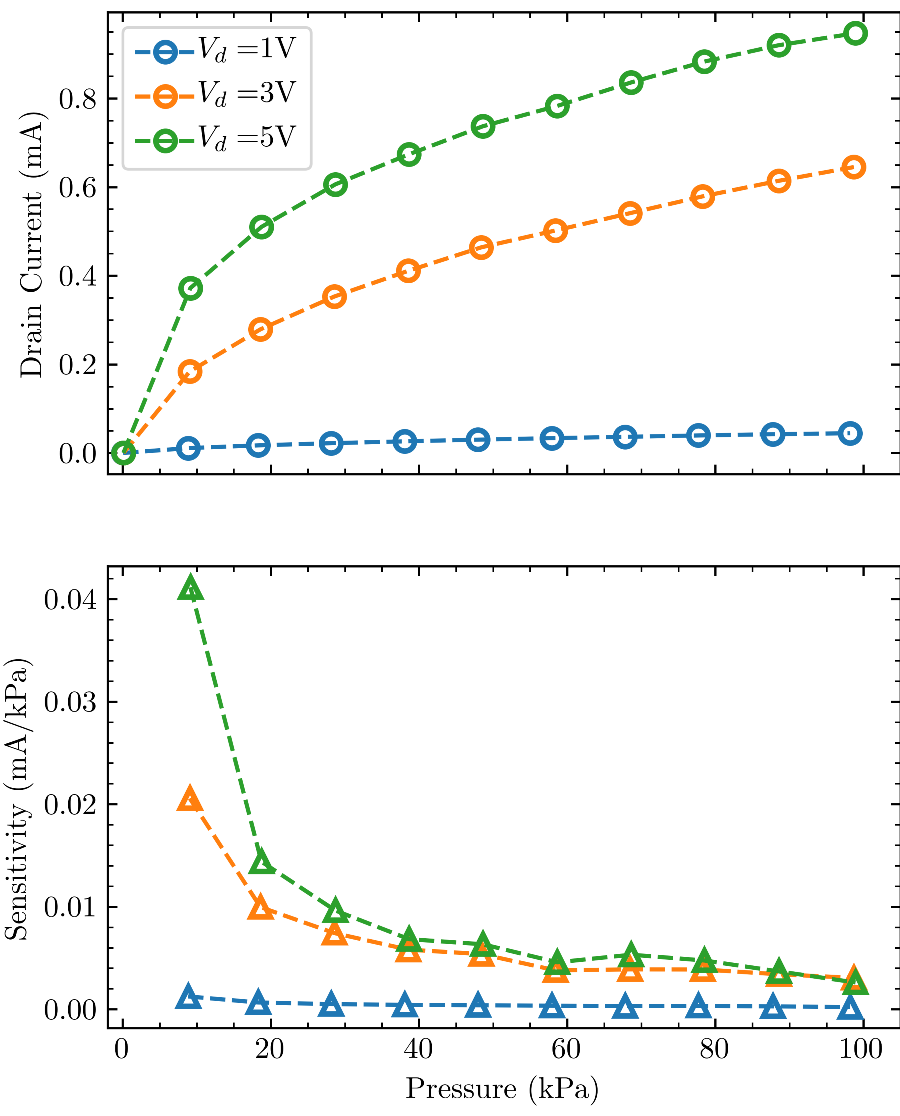

Figure 5.9: Current vs Pressure where V_{GS} =+1 V and V_{DS} set to different levels

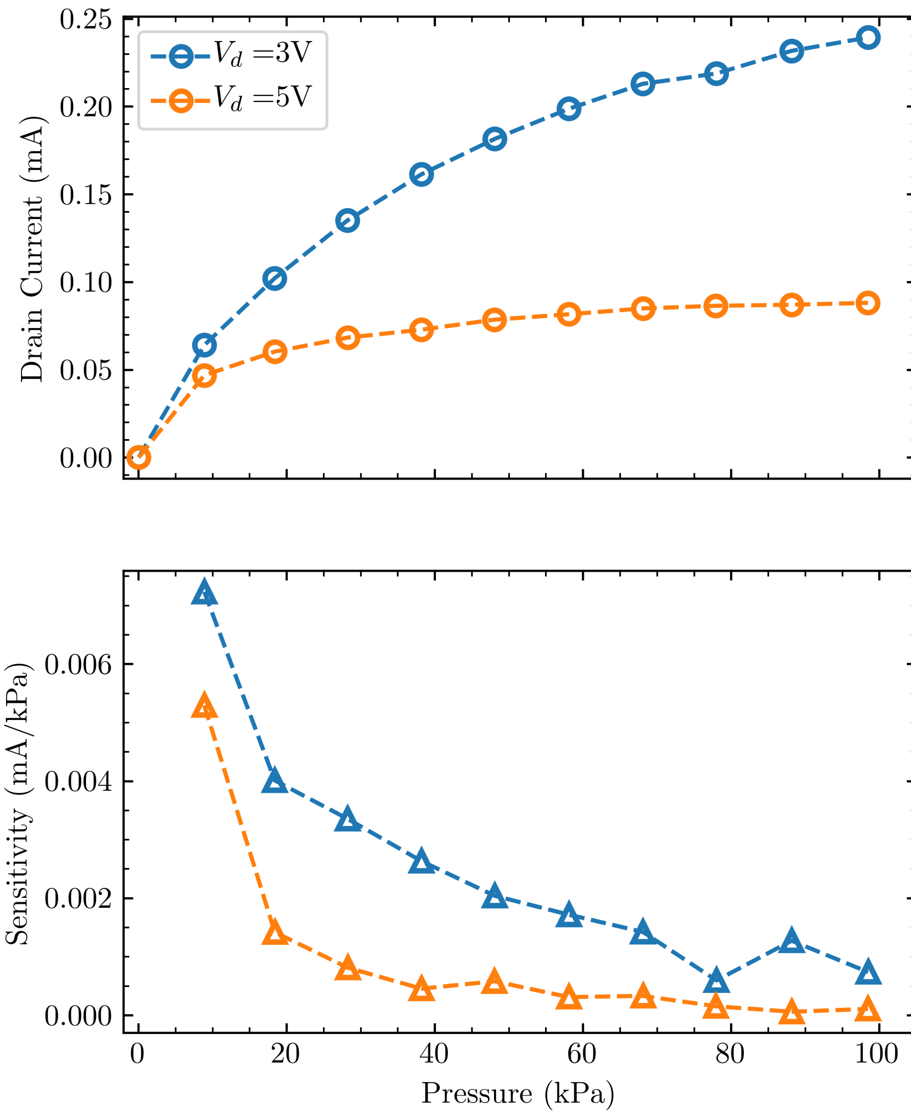

Figure 5.10: Current vs Pressure where V_{GS} =-1 V and V_{DS} set to different levels

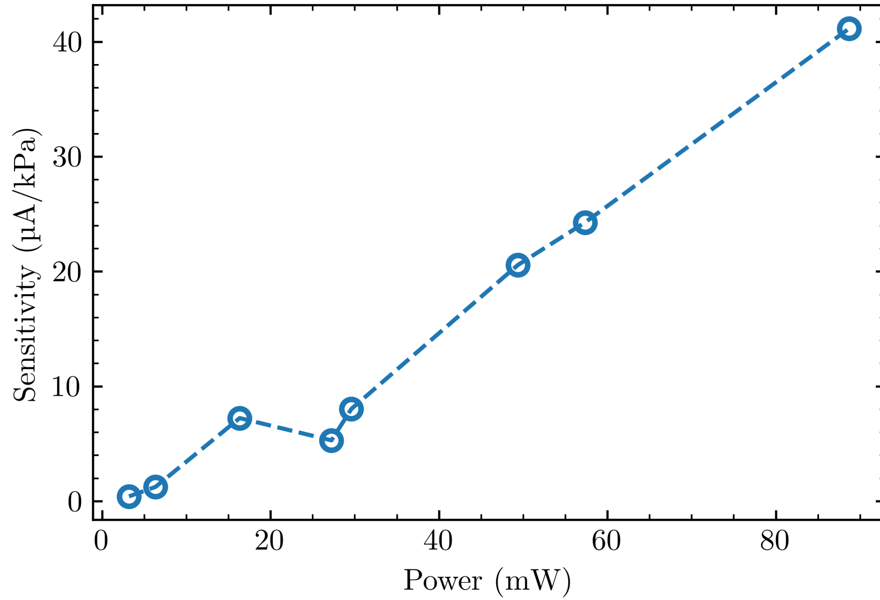

Figure 5.11: Sensors output peak sensitivity vs DC power consumption

tivity is 41 µA/kPa, which is over double the sensitivity with a gate voltage of 0 V. This does come with a penalty of increased DC power consumption of 89 mW, which is 54% higher. This figure also shows that the sensitivity in the linear region is low.

Figure 5.10 shows the sensor output and sensitivity where $V_{GS} = -1$ V. The output in this case is relatively poor compared to the previous two cases and its stability is poor. For the case of $V_{DS} = 1$ V, a reasonable signal could not be obtained to be plotted. The peak sensitivity is 7.2 µA/kPa with $V_{DS} = +3$ V and 5.3 µA/kPa for $V_{DS} = 5$ V. This would suggest that operating the sensor in this configuration will yield inaccurate results.

Figure 5.8 presents some of the data in the previous figures where $V_{DS} =$ 5 V and each trace represents the gate voltage. This figure clearly shows the relationship between gate voltage and sensitivity.

Overall the sensitivity of the output current to pressure relates to both the gate voltage and the drain voltage. When the HEMT is run in the linear region, the change in carrier concentration due to stress is lower when com-

pared to the change in the device while operating in saturation. The higher drain voltage increases sensitivity but with the penalty of increased power consumption. This higher peak sensitivity is down to the amplification effects of the HEMT, which increases the overall magnitude of the signal. As the pressure increases, the sensitivity decreases. Where the gate voltage is constant and the drain voltage varied, the sensitivity curves tend towards towards each other as the effect of the signal amplification diminishes, leading to a similar sensitivity at a lower power consumption form approximately 40 kPa.

When $V_{GS} = 0$ V, the increase of drain voltage from 3 V to 5 V results in a doubling of peak sensitivity with a 93% increase in power consumption. Similarly, when $V_{GS} = +1$ V, the increase in drain voltage results in in a doubling of the peak sensitivity and an 80% increase in DC power consumption. The gains in sensitivity and increase in DC power consumption are similar when varying the gate voltage and keeping the drain voltage constant. Power consumption was at its lowest when operating in the linear region, however any advantages of this may be nullified by increased complexity in the readout circuitry. Figure 5.11 shows the peak sensitivity of the pressure sensor vs peak DC power consumption. These data are also displayed in table 5.2 which includes the different operating modes relating to the power-sensitivity pairs.

The applied piezoelectric polarisation with regard to pressure remains constant and independent of the gate and drain voltage. Hence the percentage change in current with respect to pressure increases as the amount of current, controlled by both V_{DS} and V_{GS}, decreases. Hence the HEMT is at its most sensitive in percentage terms at pinch off. The low absolute current at this point presents challenges in detecting the current itself. Work by Boulbar *et al.* [91] studies the operation of a Ring-HEMT pressure sensor at various gate voltages below 0 V which confirms this, however the drain-source voltage is kept constant and hence the effect of this is not reported.

Trends in operation similar to those identified here, exist in literature from devices using a ring-HEMT approach or otherwise, and in both AlGaN/GaN and InAlN/GaN HEMTs. Work by Chapin *et al.* [102] demonstrated an InAlN/GaN pressure sensor at 300°C and room temperature. This work shows the sensitivity increasing with drain voltage. This work shows the

sensitivity, expressed as percentage change in current per psisg, increases as the gate voltage decreases to -5 V but when expressed in mA/psi, this decreases as the gate voltage gets more negative. This work quotes a sensitivity of 0.64 %/psig (0.093 %/kPa) tested from 0 to 206 kPa. By comparison, the sensitivity of the work in this thesis is 0.24 %/kPa where V_{GS} = 1 V and V_{DS} = 5 V. While this may look contradictory, it does makes sense as the device is essentially operating as a amplifier at this point, hence the effect of strain on the carrier concentration is amplified. Looking at the operation of this device at $V_{GS} = -1$ V, which is closer to the pinch off, the percentage change in current increases from 0.09 %/kPa where $V_{DS} = 5$ V to 0.13 %/kPa at $V_{DS} = 3$ V. Further investigation into the performance of the device in the sub-threshold region could be done..

Work by Dzuba *et al.* [101] present an AlGaN/GaN based pressure sensor with different ring-HEMT gate designs. This work reports sensitivity in pC/kPa. The sensitivity between 0 and 36 kPa of the most sensitive design was 4.4 pC/kPa.

The main take away here is that the AlGaN/GaN pressure sensor presented here is as sensitive or more so as those presented in literature. Further investigation of the performance of this device at elevated temperature would indicate further if this device can maintain a sensitivity advantage over the InAlN/GaN device.

Table 5.2: Sensitivity and Power Consumption of the ring HEMT pressure sensor at various operational modes.

V_{GS}	V_{DS}	Power (mW)	Sensitivity ($\mu A/Pa$)
0	1	3.20	0.4180
0	3	29.61	8.0333
0	5	57.36	24.2655
1	1	6.35	1.2429
1	3	49.37	20.5587
1	5	88.73	41.1504
-1	3	16.34	7.2316
-1	5	27.23	5.2941

5.3.2 Conclusions

This section has presented a AlGaN/GaN on silicon pressure sensor, utilising a ring-HEMT design. Discussed was the design and fabrication, electrical characterisation, and calibration of the device. The electrical characterisation shows that the HEMT is behaving as expected, where the transfer function shows and a normally on device, with a threshold voltage of −2.3 V. Looking at the output curves, the HEMT enters the saturation region at around 1.3 V for the gate voltages tested, which match the transfer function.

The sensors were calibrated between 0 kPa and 100 kPa with the HEMT operating in both the linear and saturation region. The work here showed a peak sensitivity of 41.15 µA/kPa when $V_{GS} = 1$ V and $V_{DS} = 5$ V with a DC power consumption of 88.73 mW. The sensitivity increases drastically between the linear region and saturation (1.24 µA/kPa to 20.56 µA/kPa at $V_{GS} = 1$ V).

Chapter 6

Gas Detection with Calorimetric Flow Sensor

6.1 Introduction

This chapter presents a novel GaN-on-Si calorimetric thermal conductivity sensor that enables the simultaneous measuring of the concentration of a calibrated gas and the flow rate of said gas. The sensor device uses a calorimetric flow sensor, that consists of one hot-wire in the centre of the membrane and two thermopiles, one upstream and one downstream of the hot-wire to detect the temperature profile of the gas. The principle of operation is similar to the thermoresistive anemometer presented in chapter 4, however with the addition of the up-stream and down-stream temperature sensors, it is possible to obtain more detail on the thermal profile of the fluid over the sensor. The idea of using the calorimetric principal to simultaneously decouple flow rate and thermal conductivity is presented in [180], where varying the frequency of the current delivered to a heater and other resistive elements is used ti differentiate between the properties. This work will operate the heater in a DC mode along with the thermopiles. Using the information from the outputs of the three sensing elements, this chapter will explore linear methods simultaneously predicting the flow rate and gas concentration. Further, this work presents a neural network that is used to predict the fluid properties.

The primary objectives of this experiment was to determine:

1. Sensitivity to gas concentration - specifically, Hydrogen.
2. Sensitivity to flow rates from 0 to 250 SCCM.
3. The ability of statistical methods to reliably simultaneously predict the flow rate and gas concentration.

Several gases could be considered of interest for this experiment for various applications. Carbon monoxide or dioxide detection would be useful in boiler applications as well as hydrogen. Figure 6.1 shows the fitting of the 1D equation, where the y axis is the heating power required to keep the heater at 200 °C above the fluid temperature for a flow velocity from 0 m/s to 22 m/s:

$$P = \frac{NukA_H\Delta T}{L} \tag{6.1}$$

defined in chapter 2 of this thesis. For this application, the value of k which represents the thermal conductivity of the fluid, and Nu the Nusselt number, which is made up of the Reynolds number, representing flow rate, and the Prandtl number, representing the specific heat capacity and thermal conductivity, vary according to the gas selection. Helium and hydrogen are the gases with the highest thermal conductivity and thus the sensor would be most sensitive to. This is compared to the worst of those included, which is carbon dioxide. For this reason, and for its easy availability, hydrogen was chosen as the mixture gas for these experiments. It would be of interest to study the performance of the same device to carbon dioxide in further work.

Nitrogen, oxygen, and air have an almost identical response in the model. Suggesting that measurements with nitrogen as the carrier gas could be comparable to measurements with one of the others. Thus, the performance of the device to a hydrogen-nitrogen mix could be inductive of the performance to a oxygen-hydrogen mix. One of the key benefits of GaN devices over silicon based equivalents are their performance in harsh environments, and oxygen-hydrogen gas mixtures are used in many space applications, thus providing a potential application. Nitrogen was chosen over oxygen in this work as for cost and safety reasons, since pure oxygen is highly reactive.

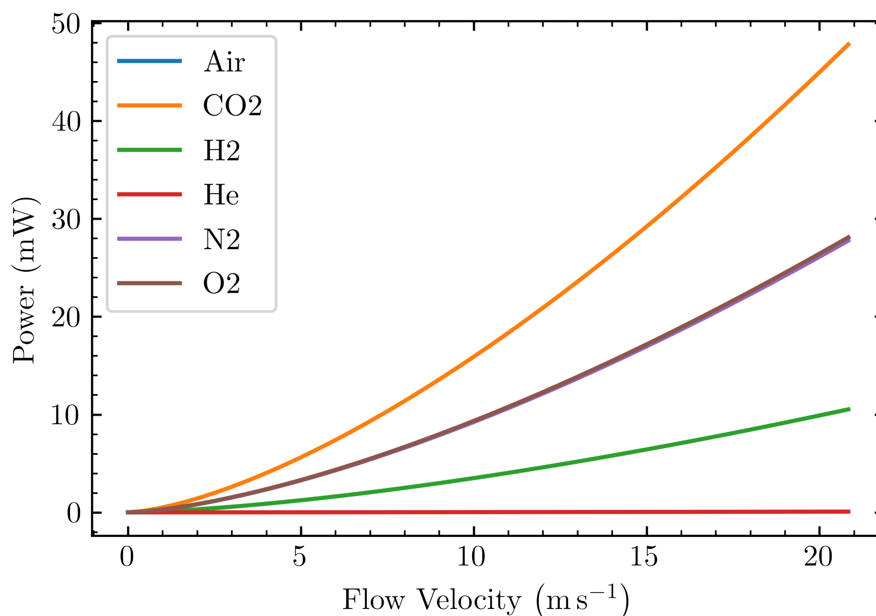

Figure 6.1: Heater DC power consumption vs flow velocity for various gases as per equation 6.1.

6.2 Design & Fabrication

The calorimetric device presented and tested here is the same device design as presented in chapter 3. In this chapter, the embedded thermopiles are used as upstream and downstream temperature sensors to complement the hot-wire in the middle.

Figure 6.2 shows the top down view of the sensor with some key dimensions. Figure 6.3 shows the cross-sectional view of the device to show the thermocouples. Each thermopile consists of 5 thermocouples connected in the series. These thermocouples consist of a length of gold track, running from the side of the membrane to a distance of 300 um into the membrane. At this point, an ohmic contact connects the gold track to the 2DEG below. This point here forms the hot junction of the thermocouple. The 2DEG channel then runs in parallel to the gold track, offset by 15 um, back onto the unreleased part of the chip die. Here another ohmic contact connects the 2DEG region to the gold track of the next thermocouple. This represents the cold

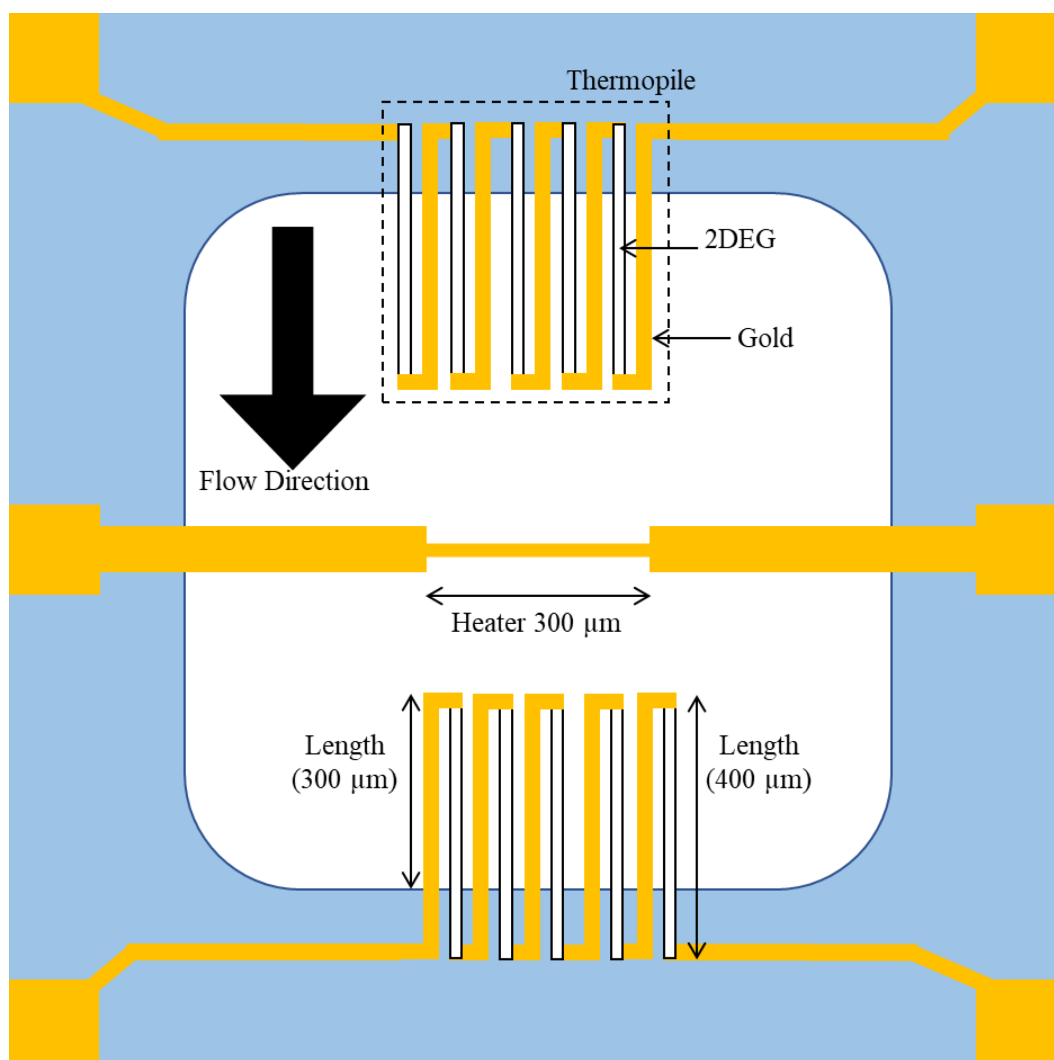

Figure 6.2: Top down schematic view of the sensor die showing the thermopiles and heater structure.

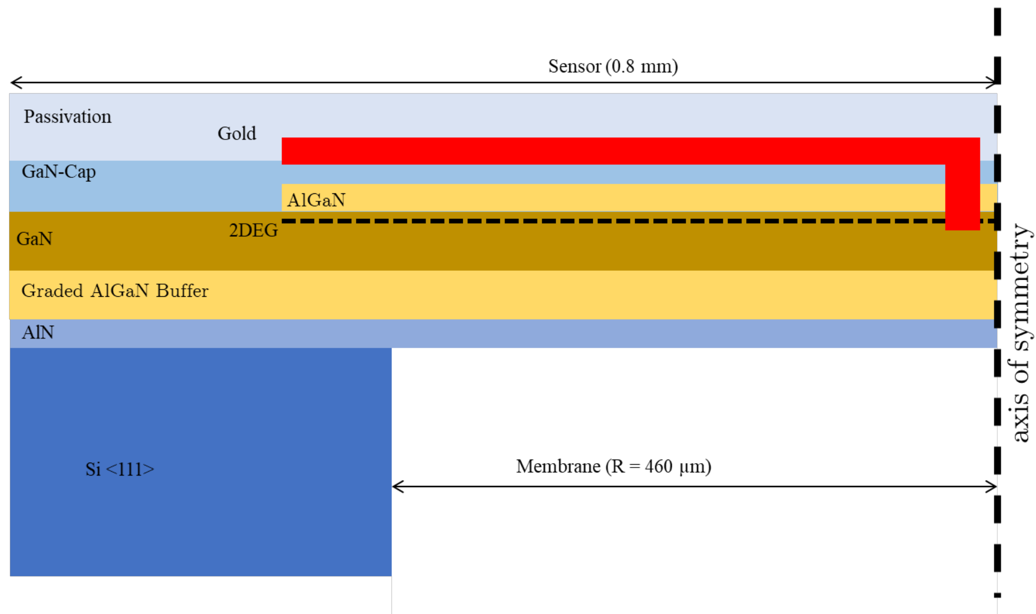

Figure 6.3: Cross section view of a Au/2DEG thermocouple.

junction of the thermocouple.

The junction at the ohmic contact between the gold track and the 2DEG is where the Seebeck effect occurs. This is the electro motive force (emf) that develops between the two points of a material, where there is a temperature gradient between them. By connecting the 5 thermocouples in series, the emf of each thermocouple is combined so that the differential voltage of the whole thermopile is five times that of the one thermocouple.

The hot junction of the thermocouples are 150 um up and down-stream of the heater. This means that when the heater is on, the hot-junctions of the thermopiles are within the heated area around the heater. Therefore the thermopile output voltage needs to be calibrated based on the temperature of the hot-wire in zero flow conditions.

By design, the upstream and downstream thermopiles should be symmetric around the hot-wire. This would ensure uniformity of the response Due to poor mask alignment in the fabrication process, this is not the case and there is a slight offset on the fabricated devices.

6.3 Automated Testing Station

In order to test the response of the sensor to various gases, a custom automated test rig was developed. The test rig can deliver gas mixtures at controlled concentrations and can control atmospheric conditions such as humidity and flow rate.Figure 6.4 shows a schematic representation of the rig. There are 3 MFCs controlling the input gas. One is used for the mixer gas (Hydrogen in the case of this work) and the other two for the carrier gas (Nitrogen). One of the carrier MFCs feeds into a bubbler filter which can create humidity in the gas lines over the sensor. In addition to the gas controllers, there are the measurement and control instruments, which consist of a Keithley 2600 series SMU to drive the hot-wire and two differential 16-bit ADCs with programmable gain to measure the thermopile voltage. The 'brain' of the system is a Raspberry Pi 3 running custom software in python that enabled the rig to be controlled remotely over the internet.

6.3.1 Hardware

Gases are supplied from either mains lines or gas cylinders with either premixed or pure gases. The gases can be diluted with zero-air, supplied from a zero-air generator, or Nitrogen.

The rig consists of 3 gas lines each controlled by an Alicat MCV series Mass Flow Controller. One is used for the gas of interest and another for the mixer gas. This allows the rig to deliver gas mixes of specific concentrations to the sensor. The 3rd is used to control an air bubbler which can introduce humidity in the system.

The mixer gases (refers to a combination of the wet and dry lines) are mixed with the gas-of-interest at two separate T-joints where the mix gas is introduced at a 90 degree angle to the gas-of-interest. This causes turbulence in the system that allow the gases to mix.

The mixed gas is connected to the 3D printed flow chamber, where the DUT is located. The outlet of this chamber leads to a flow meter, which is used to monitor leakages. Leading up to the chamber, the geometry of the

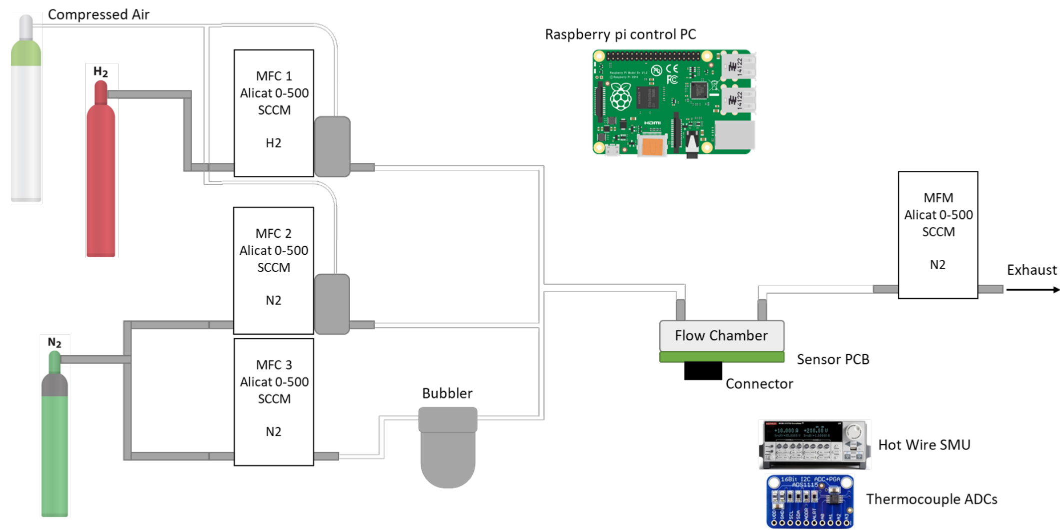

Figure 6.4: Schematic of the gas rig

pipe work is such that the flow gets laminarised so that the Reynolds number of the mixed gas flow is in the laminar region when it enters the flow chamber. This ensures a consistent boundary layer over the DUT.

A Keithley 2600 series SMU was used to drive the hot-wire. Using the python script, the SMU can drive the hot-wire in constant current mode while simultaneously measuring the voltage drop. For the thermopiles, the two ADS1115 differential 16-bit ADCs measure the voltage difference between the terminals of each thermopile. These communicate with the Raspberry Pi 3 Model B+ over an I2C protocol.

6.3.2 Control Software

A Raspberry Pi was used to control the gas rig MFCs, the SMU, and the thermopile ADC's. This control was implemented using a python 3 based flask server which provides a web based GUI that can be run in any browser.

The back-end of the web server contains all the functions necessary for automated operation of the gas rig, including; independent threading for continuous measurement of attached instrumentation, methods for setting MFC parameters, methods for saving experiment outputs.

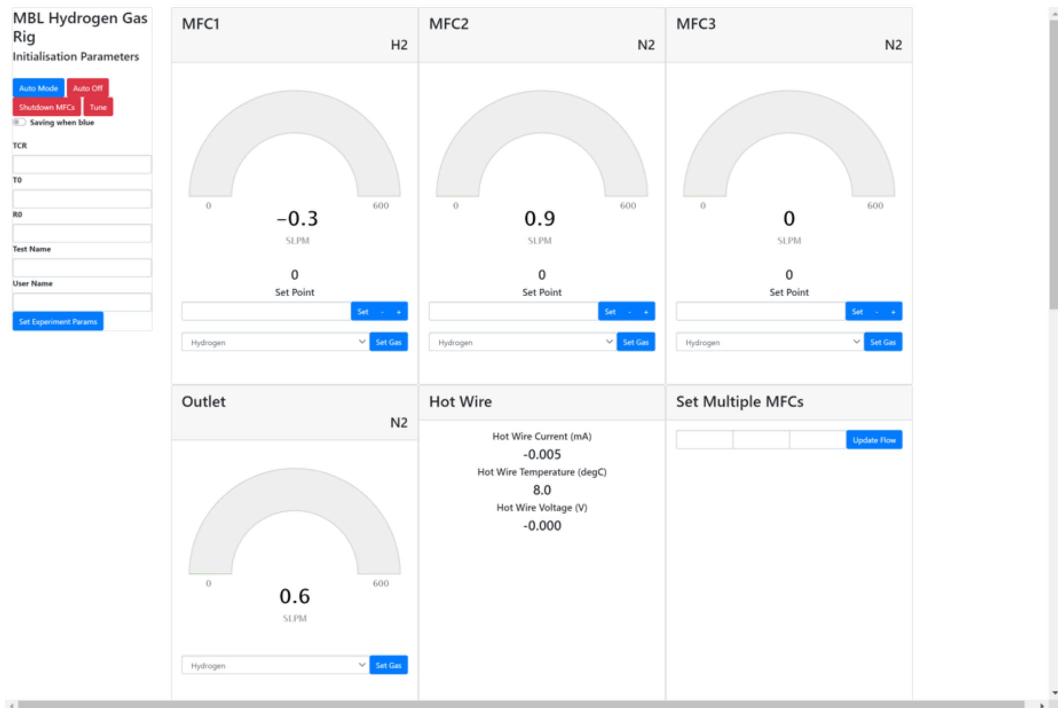

Figure 6.5: Gas Rig GUI for rig controls (Microsoft Edge browser)

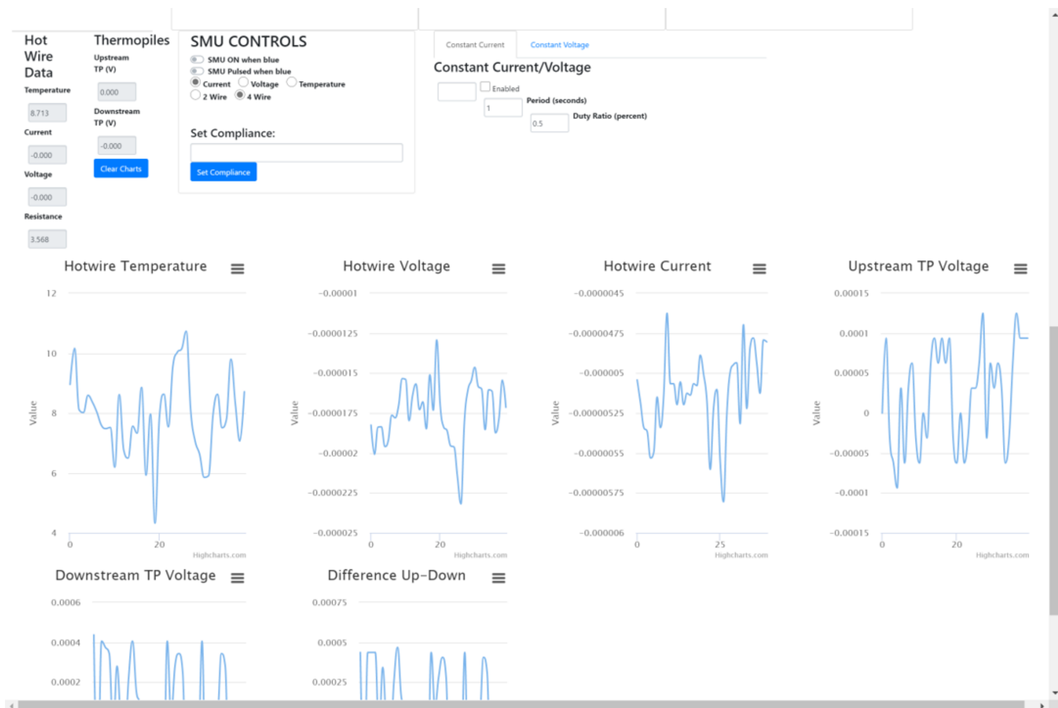

Figure 6.6: Gas Rig GUI for rig data display (Microsoft Edge browser)

A basic graphical user interface was implemented that shows the flow rates of the MFCs in real time, as well as the hot-wire power consumption. The interface allows manual control of individual MFCs and the hot wire SMU. For automatic operation, an input file which contains flow rates, gas concentration, and test times is uploaded and the data converted into mass flow rates. The software automatically steps through the test data rows and record outputs to a csv file.

The front end interface was created using HTML and JavaScript for the visualisations. The interface uses the Highcharts API to generate the gauges and complex charts. This is shown in figures 6.5 and 6.6.

6.4 Experimental

The experiment was conducted using a nitrogen-hydrogen mix. Flow rates from 0 to 250 SCCM were selected at various hydrogen concentrations from 0% to 100%.

The electro-thermal characterisation was done using the Cascode Microtech probestation using a Keithley 2600 series source meter unit for data acquisition. This gold heater is identical to the one discussed in chapter 5, and so the results of this characterisation are presented there.

Following this, the measurements were conducted to characterise the performance of the devices in the presence of flow and H_2. Flow, and gas concentration was controlled using the gas rig developed and described in the previous section. The test was conducted with the hot-wire operating at a constant current of 94 mA which corresponds to a hot-wire temperature of approximately 200 °C with stagnant nitrogen. A sweep of flow rates was done from zero to 250 SCCM at a specific hydrogen concentration, then repeated for another concentration. Between flow sweeps, the test chamber was purged with the next gas mix so that the sensor performance at zero flow was captured. This was done for the hydrogen concentrations of 0%, 20%, 40%, 60%, 80% and 100%. The sensor output was calibrated so that the output voltage is the voltage relative to the voltage at zero flow in pure nitrogen for the hot-wire

and both thermopiles. HW, TP_D and TP_U refer to the Hot-Wire, downstream thermopile, and upstream thermopile respectively, and the outputs labelled as V_{HW}, V_D, and V_U respectively.

During the experiment, there were occasions where the thermopiles needed breaking and re-breaking in due to diodes forming at the ohmic contacts at the junction between the gold and the 2DEG, thus causing the devices to stop behaving like thermopiles. This was done by applying a voltage bias sweep from 0 V to 30 V. The exact cause of this phenomena is currently unknown. Further investigation is needed into the device level physics to determine the cause of this.

6.4.1 Data Pre-processing

Before using the prediction methods the data were processed to account for variations in the three inputs so that the prediction would yield appropriate results. Two pre-processing methods are used in this work.

1. Input pre-processing. The input voltage values were processed into a range from -1 to +1 so that a larger input would not have a disproportionately large weighting on the outputs of the prediction. This was done by the equation $[2(V - V_{min})/(V_{max} - V_{min}) - 1]$.
2. Output processing. This standardises the outputs between 0 and +1. The outputs of the prediction function must be converted back into their original values. This was done by O/O_{max} where O is the output of either flow rate or gas concentration.

6.4.2 Linear Prediction

The use of two linear prediction techniques, PCR and PLSR, were explored to establish a predictive model from a set of independent variables (the temperature sensors) onto another set of continuous variables (targets). Both methods can model a response variable with several input variables where the variables are highly correlated or collinear. PLSR and PCR both construct

new predictor variables, known as components, as linear combinations of the original predictor variables. The construction of these components are different for each method, the key difference being that PCR does not consider the response variables where as PLSR does. This means that a PLSR model may be able to fit the response with fewer components. Although, this does not always lead to a better fitting model [181].

PCR uses Principal Components Analysis (PCA) to decompose independent variables into principle components, then selects a subset of those components as variables to predict an output. PCA finds a low dimensional representation of the data set that contains as much as possible of the variation. The first principal component is essentially a linear best fit line, that in most linear relationships capture most of the variance. Additional principal components are then obtained based on the variance remaining after accounting for the previous components. It is desirable to select the least number of components that can sufficiently explain the variance in the data. The PCR is then constructed using these principle components as the predictors in a linear regression model. The core concept of a PCR is that a small number of components are sufficient to explain most of the variance in a higher order data set, and hence the relationship between the input variables and the response [182] [183].

PLSR is similar to PCR in that it applies a dimensionality reduction to the input samples, however this reduction is supervised by the known response of the input variables [184]. This produces a technique that can separate sample noise in order to make linear combination in the dependent concentration matrix [185]. The PLSR algorithm finds the directions of maximum correlation between the sensor responses and the output features of the repose [186]. PLSR is considered the best technique in chemometric applications due to its ability to handle collinear data and reduce the number of required calibration samples [187]. Further usage of PLSR in sensor applications are given in [188] [189] [190]. This, however, may not always be the case. Both algorithms were implemented using the Scikit library for python.

6.4.3 Artificial Neural Network

An Artificial Neural Network (ANN) is a web of adaptive non-linear elements connected in parallel. This resembles the physiological system of neurons and synaptic links. This work makes use of an ANN to decouple the flow rate and thermal conductivity parameters to give a prediction of each of these parameters based on the individual sensor inputs. Figure 6.8 shows the network diagram of the neural network used here. This network includes 3 layers, one of which is hidden, with 3 nodes in the first input layer, 2 in the output layer, and 8 nodes in the hidden layer.

Modern smart sensors and sensor systems involve an array of several different sensors, where it is difficult, if not practically impossible to develop a hard analytical model relating all the different parameters. ANNs are powerful non-linear algorithms that can be used to perform data discrimination and pattern recognition in a variety of fields with different data types. The ability of ANNs to solve multi-variable non-linear functions has led to their widespread use in applications involving sensor arrays, such as in electronic noses.

Following the attempt at fitting done with the linear statistical methods, the work in this chapter implements an ANN to discriminate between flow rate and thermal conductivity of a fluid in an attempt to improve the performance of the linear methods. The inputs to the ANN are taken from the 3 devices on the flow sensor chip. The ANN was implemented using the Keras API of the Tensor Flow AI package from Google in Python.

The process steps are as follows:

1. Organise data set. The test data collected and processed in the method outlined earlier in the chapter was organised into 3 input columns and 2 target columns.

2. Preprocess Inputs Features. As above to scale from -1 to +1.

3. Build Model . The model was built with 3 layers. The first with 3 nodes being the input, the next is the hidden layer consisting of 8 nodes and the output layer with 2 nodes for the 2 outputs.

4. Model training. The model was then trained using the same training dataset as was used for the linear techniques.

5. Model is ready to be used for prediction

The raw data (voltages) of the hot-wire and two thermopiles is preprocessed so that the weighting applied to each input is not skewed by the different sensitivity of the devices. As in previous chapters, the first step involves calibrating the data so that a 0V output corresponds to the voltage of the devices where the flow is stagnant. In this chapter, it is important to specify that the stagnant air is an atmosphere of 100% nitrogen, achieved by purging the gas lines with pure nitrogen before testing. Next, the input data was auto ranged between -1 and +1 to remove any tenancy for the ANN to apply unwanted bias to higher absolute values. Additionally, the sigmoid activation function used in the nodes tends to infinity or minus infinity the further the input is from zero. The output values used to feed into the ANN during training were ranged between the 0 and 1, where 1 represents a 250 SCCM flow rate and a 100% hydrogen atmosphere.

With the training data ready, the sequential model was developed. This network makes use of 3 layers in total. The input layer with 3 nodes, the output layer of 2 nodes, and a singular hidden layer with 8 nodes. Each of the 3 input nodes are connected to each of the 8 nodes in the hidden layer. The nodes make use of a sigmoid function activation.

The model was then trained using the backward propagation method using the Adam optimization algorithm and a mean squared error function. These were chosen as they are standard used methods. The Adams algorithm is computationally efficient, low on memory usage, and requires no previous knowledge of the network. The mean squared error method is used in regression based NN problems, such as the one presented here. Figure 6.7 shows the progression of the neural network training, where the Mean Squared Error (MSE) improves with each epoch. The figure shows a large reduction in the MSE occurs after approximately 32,000 epochs. The rate of improvement decreases after this, up to 50,000 epochs; the stop limit chosen for the training algorithm. As the figure shows, the improvement still occurs after this

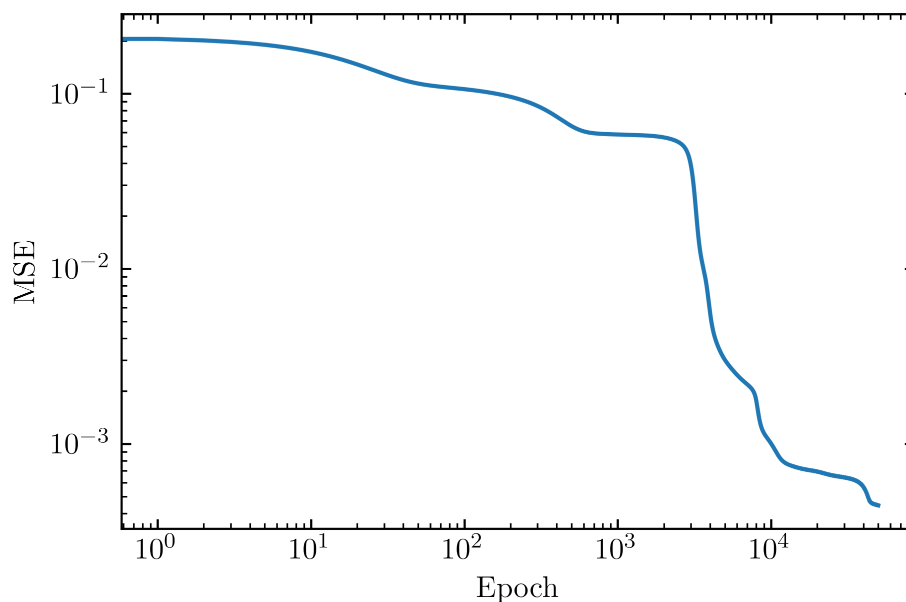

Figure 6.7: Figure showing the mean squared error of the neural network versus the epoch number, up to 50,000

point, however the error at this point was determined (and is proven later in the chapter) to be sufficient for accurate predictions without needing the time investment to train further.

6.4.4 Post Processing

Experiential data was post-processed using a python script. The time series data were passed through a change detection algorithm to find the points in the experiment where the concentration changed. In order to account for the periods when the MFCs are updating, the first and final 15 data samples of every section are deleted. Then, the mean for each column in each segment is calculated. Finally, the data set is normalised to account for any variance by device by calculating the output relative to the values at zero flow, with an atmosphere of 100% N_2.

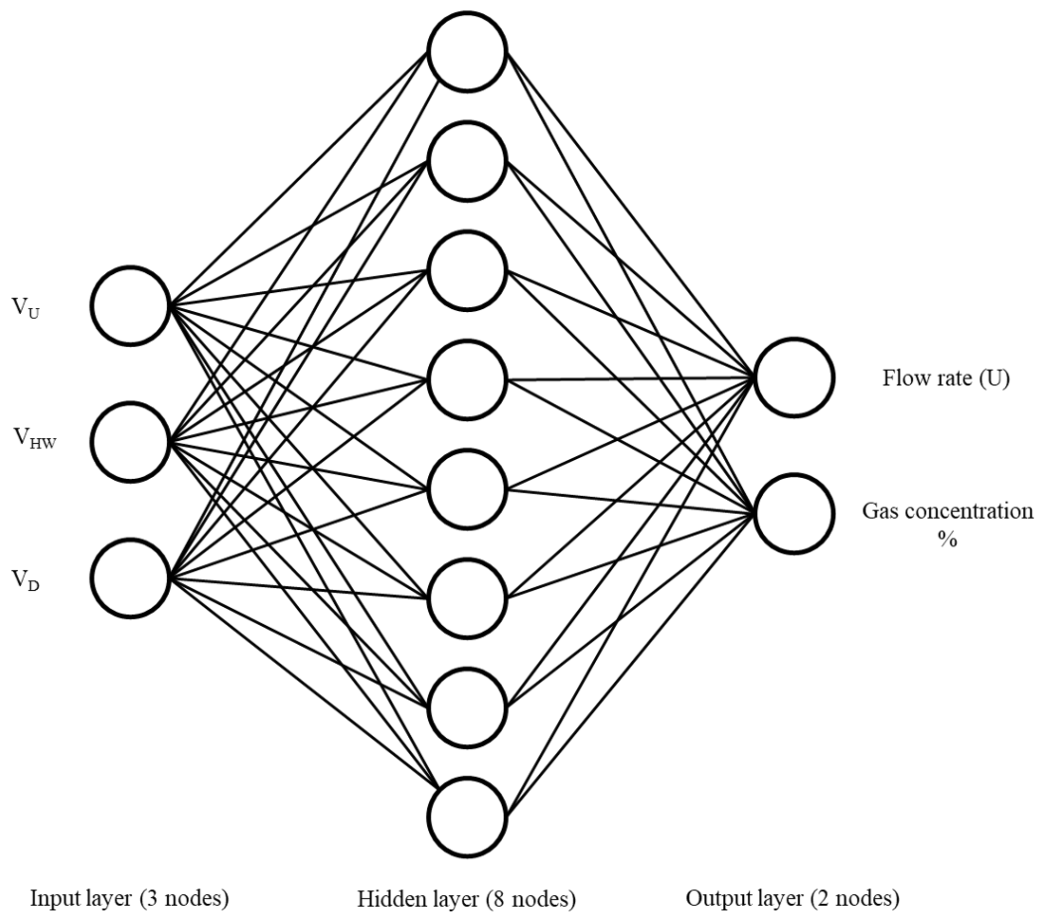

Figure 6.8: Neural Network Diagram with two processing layers

6.5 Discussion

6.5.1 Sensor Output & Thermal Conductivity

Figure 6.9 (a) shows the hot-wire voltage against flow rate at different concentrations of hydrogen. Given that H_2 typically has a thermal conductivity of 186 mW/mK compared to 26 mW/mK for N_2 [1], it is expected that more heat transfer occurs as the hydrogen concentration increases, thus lowering the voltage drop across the hot wire. The figure shows that this device is in agreement with this. Further, the figure shows that the thermal conductivity of the fluid dominates the heat transfer compared to the forced convection.

Sub-figure (b) and (c) of figure 6.9 shows the output of the thermopiles to the fluid, where (b) is the upstream sensor, and (c) being the downstream. As with the hot-wire, the thermopiles are most responsive to the change in thermal conductivity than they are to the flow rate. The downstream thermopile shows a grater response to flow rate than the upstream. This is of-course due to there elevated temperature of the fluid after the heat transfer from the hot-wire. As all three outputs respond to the fluid differently, it is thus possible to extract information about the fluid characteristics from this data.

In the extreme cases where the atmospheres are pure, the hot-wire alone is enough to differentiate between gases and flow at the flow rates tested, since the maximum voltage drop at 100% N_2 and 250 SCCL flow is lower than that of 100% H_2 and 0 SCCM flow. However, to increase the resolution of the gas detection, the thermopiles need to be used in conjunction with the hot-wire.

Figire 6.11 shows the same data as 6.9 but with the voltage plotted against gas concentration. This figure shows that the response to thermal conductivity is generally linear with only a slight increase in output voltage as the flow rate increases for the same gas concentration.

The sensitivity of the sensing elements to flow and hydrogen concentration are mostly decoupled from the other, especially as the flow rate or hydrogen concentration increases as seem in figures 6.12 and 6.10 respectively.

[1] at 300K and 100 kPa (1bar)

The sensitivity to flow is over a relatively short range in comparison to the analysis done in chapter 4, and so the chart does not show the sensitivity tending towards zero in the same way. Some of the sensitivity flow rates are present in this experiment and in the one in chapter 4, there is a large degree of agreeance between the result, although there is some variation. For example, at the 200 SCCM point in chapter 4, the sensitivity is around 62 mV/SLPM, and for the same point in this experiment, the value is 59.5 mV/SLPM. This difference can be accounted for in the variation of room temperature, and thus the current required to reach the 200°C specified, and the slight difference in thermal conductivity of air and pure N_2. Within the pure H_2 atmosphere, the sensitivity at 200 SCCM is 69.2 mV/SLPM. Here the difference in the sensitivity can be attributed to the increase in heat transfer into the more thermally conductive H_2.

The sensitivity of the hot-wire to the change in H_2 concentration increases with the increase in thermal conductivity, and this is the case at each flow rate. At zero flow, the average sensitivity of the hot-wire to the H_2 is 0.59 mV/%, with a max of 0.72 mV/% between 80% and 100%. This average sensitivity becomes 0.62 mV/% at 250 SLPM, with a peak of 0.79 mV/%.

The sensitivity of the thermopiles is less stable than that of the hot-wire. The upstream device shows fluctuations in the sensitivity at different flow rates. This is attributed to the fact that the fluid at this point is not heated and it's temperature is influenced by outside sources, and so may not be completely consistent. The downstream sensor is more stable with flow rate. The zero flow condition fluctuates as with the hot wire, which can be explained by the natural convection happening above the sensor surface in the chamber, while there is no horizontal force. At peak flow (250 SCCM), the average sensitivity of the upstream sensor is 50 µV/% and down stream is 54 µV/%, which is similar to he sensitivity at zero flow (53.5 µV/% and 50.5 µV/% respectively).

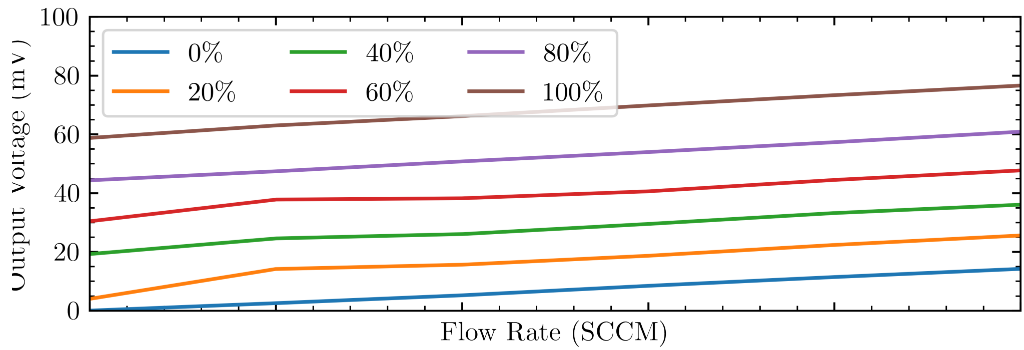

(a)

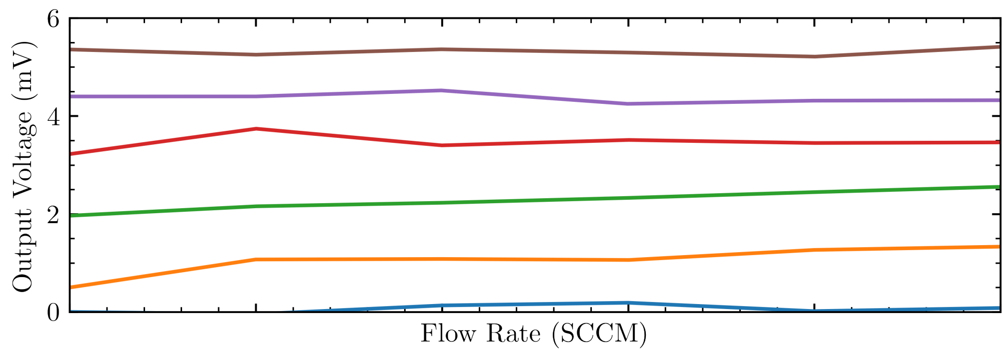

(b)

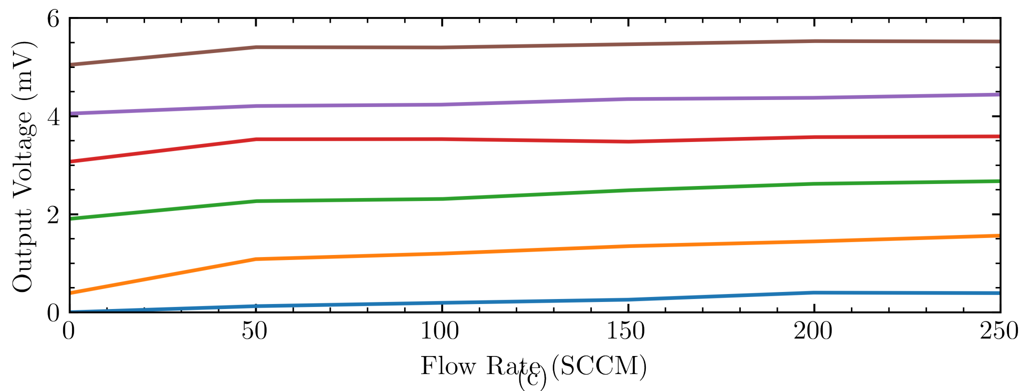

(c)

Figure 6.9: Sensor output voltage vs flow rate at different gas concentrations. (a) is the Hot-Wire output, and (b) and (c) show the upstream and downstream thermopile response (respectively). The fluid is a N_2-H_2 mixture, from 0% H_2 to 100%.

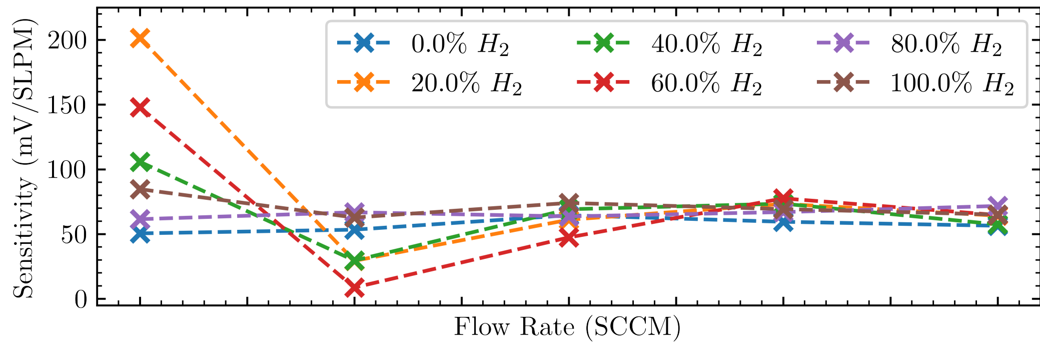

(a)

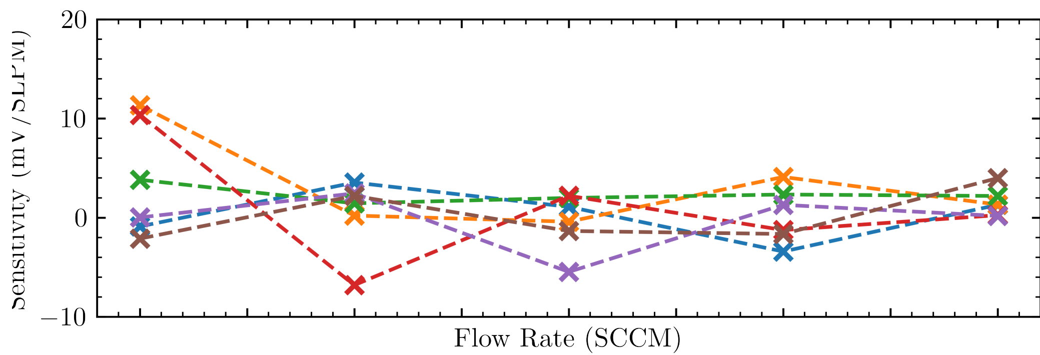

(b)

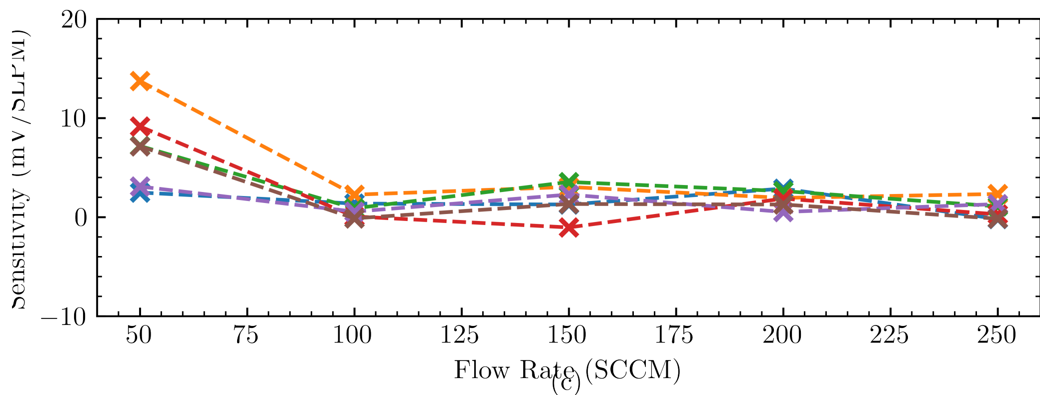

(c)

Figure 6.10: Sensor output voltage vs flow rate at different gas concentrations. (a) is the Hot-Wire output, and (b) and (c) show the upstream and downstream thermopile response (respectively). The fluid is a N_2-H_2 mixture, from 0% H_2 to 100%.

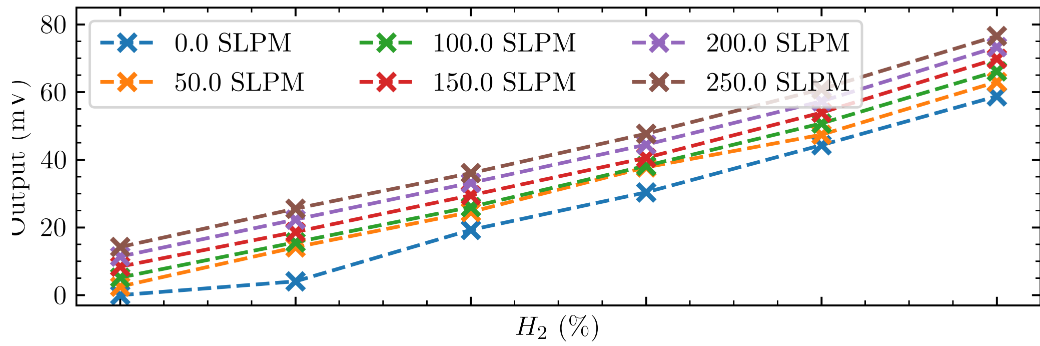

(a)

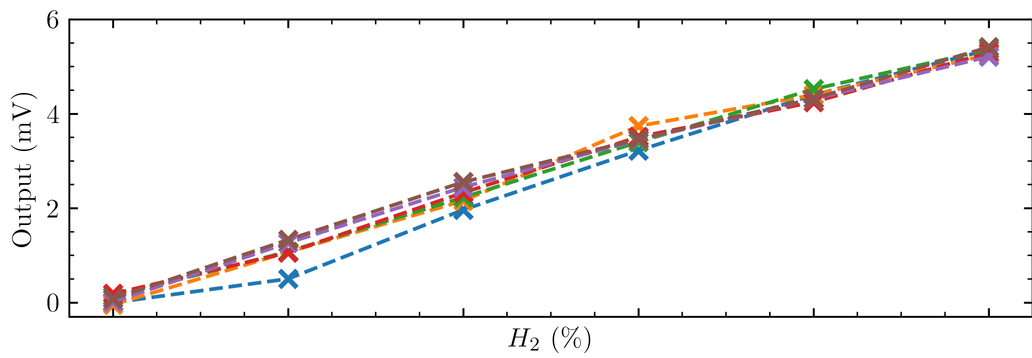

(b)

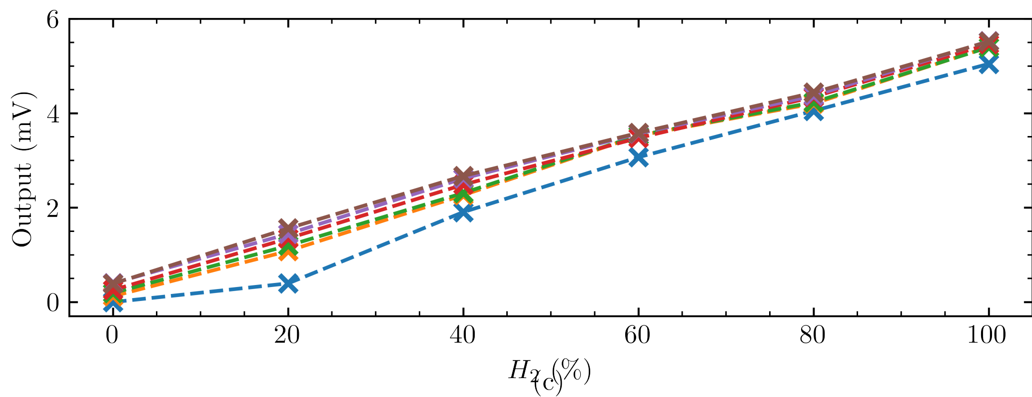

(c)

Figure 6.11: Sensor output voltage vs H_2 concentration (%) at different flow rates. (a) is the Hot-Wire output, and (b) and (c) show the upstream and downstream thermopile response (respectively). The fluid is a N_2-H_2 mixture, from 0% H_2 to 100%.

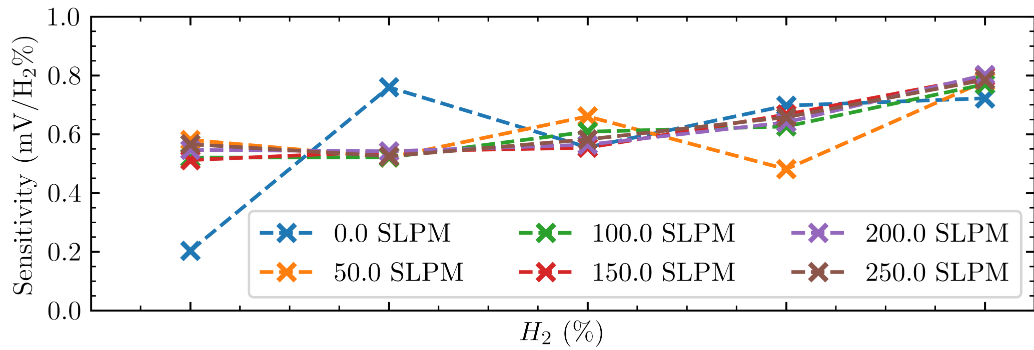

(a)

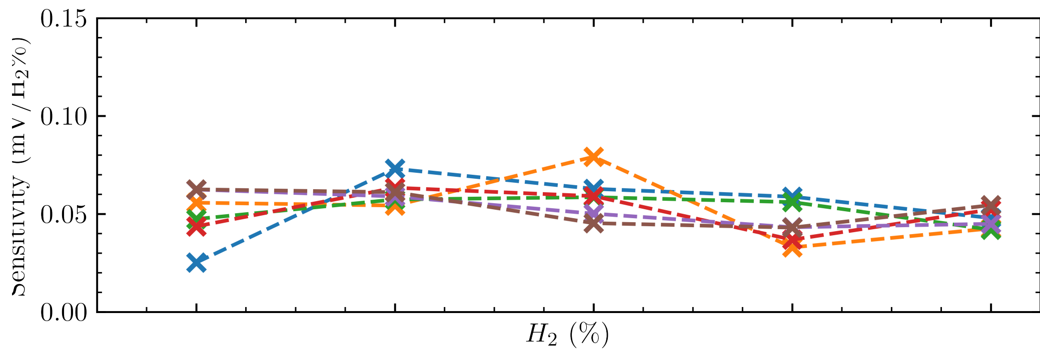

(b)

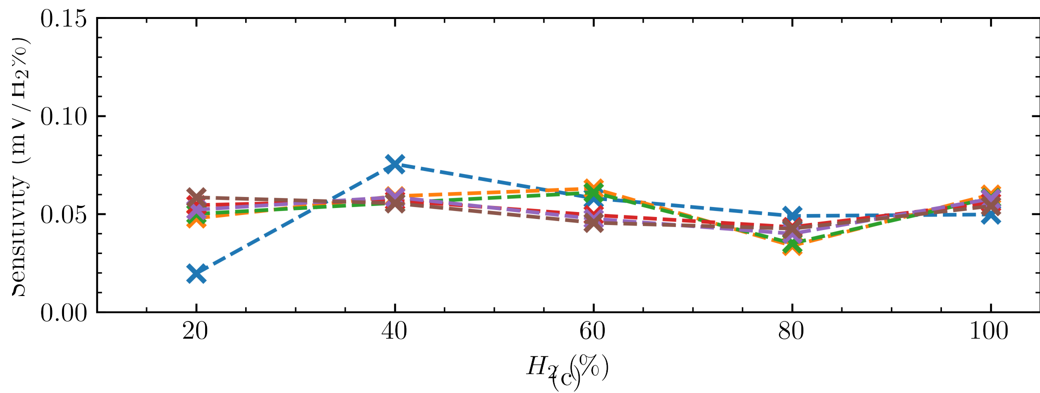

(c)

Figure 6.12: Sensor output voltage vs flow rate at different gas concentrations. (a) is the Hot-Wire output, and (b) and (c) show the upstream and downstream thermopile response (respectively). The fluid is a N_2-H_2 mixture, from 0% H_2 to 100%.

6.5.2 Linear Statistical Model

Using the python SciKit-Learn library, PCR and PLSR models were created to predict the response of the sensors to thermal conductivity (gas concentration) and flow rate. The first step in the PCR was to determine the number of components to use to make the prediction. This was done by calculating the MSE of the prediction versus the number of components used. A lower MSE indicates a better prediction. For 2 components, there is a large increase in accuracy compared to using just 1, and the improvement from 2 to 3 components is negligible, thus 2 was chosen. This was done for both the PCR and PLSR. The dataset of the experiment outputs was split randomly into a training and a testing data set. The same training set was used to train both models and the same testing data to test them.

The thermal conductivity prediction is shown in figure 6.13 vs the actual gas concentration of the fluid for both the PCR (orange diamond) and the PLSR (blue circle). The line represents the ideal fit which is $y = x$. This shows the predicted gas concentration versus the actual value. Visually from the figure, it can be seen that the variance between each point in the same prediction method is small and the overall fit it closer than that of the flow rate, showing that the linear methods are effective at predicting the thermal conductivity of the fluid. The R^2 values of for the gas concentration are 0.9892 and 0.9477 for the PCR and PLSR respectively. Interestingly, the PLSR tends to consistently under predict the hydrogen concentration, while there is no such trend in the PCR.

Figure 6.14 shows the prediction of the flow rate vs the actual rate for both the PCR and the PLSR. It is difficult to determine any trend from this data set, for the prediction of the flow rate, which suggests that there is highly non-linear relationship between the three input variables and the output. The PCR is a better predictor than the PLSR with an R^2 of 0.5721 and 0.0985 respectively. Closer inspection of the thermopile output voltage shows some instability in the signal, meaning that the relationship with flow rate is not entirely linear. The effectiveness of these linear statistical techniques drop considerably where an input value is not linear. This means further investigation is needed with the ANN approach to better map this output. In work

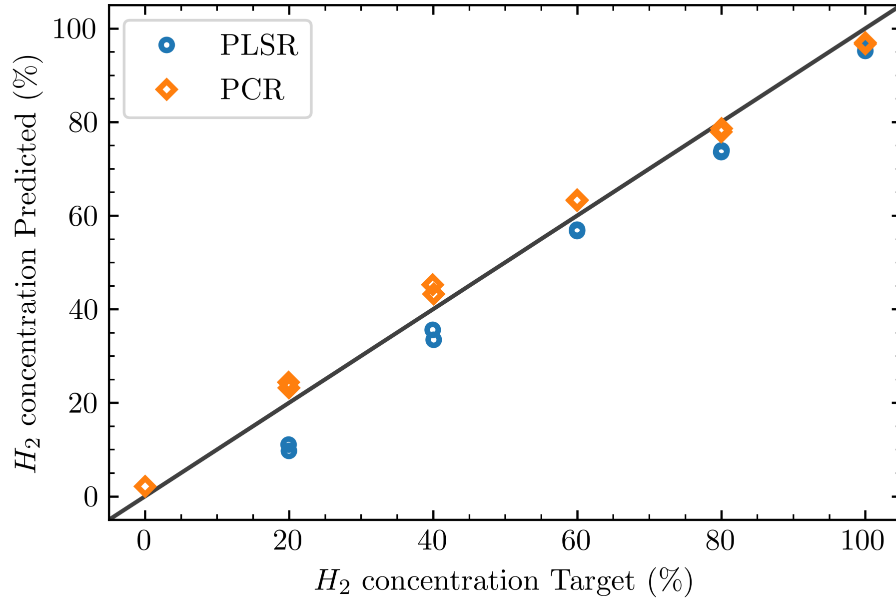

Figure 6.13: Sensor response compared with fitted response for both PLSR and PCR analysis for hydrogen concentration.

by Gardner *et al.* [191] studying a similar phenomenon with a CMOS device with 2 resistors rather than thermopiles as the temperature sensor, the linear methods predict the flow rate to a similar accuracy as the gas concentration is predicted here, and the gas concentration as poorly as the flow rate is predicted in this work. A further review of the literature would be useful to see if this difference between thermoresistive and thermoelectric sensing is common.

6.5.3 Neural Network

Figure 6.15 shows the predicted H_2 concentration against the actual concentration. As with the regression predictions, the ANN is able to predict the gas concentrations with a high level of accuracy. Where multiple points are tested, the variance is low (see 20% concentration) and are generally within the same data point on the chart. The R^2 for the ANN is 0.9956. This is also a a 5.05% improvement, compared to the PLSR.

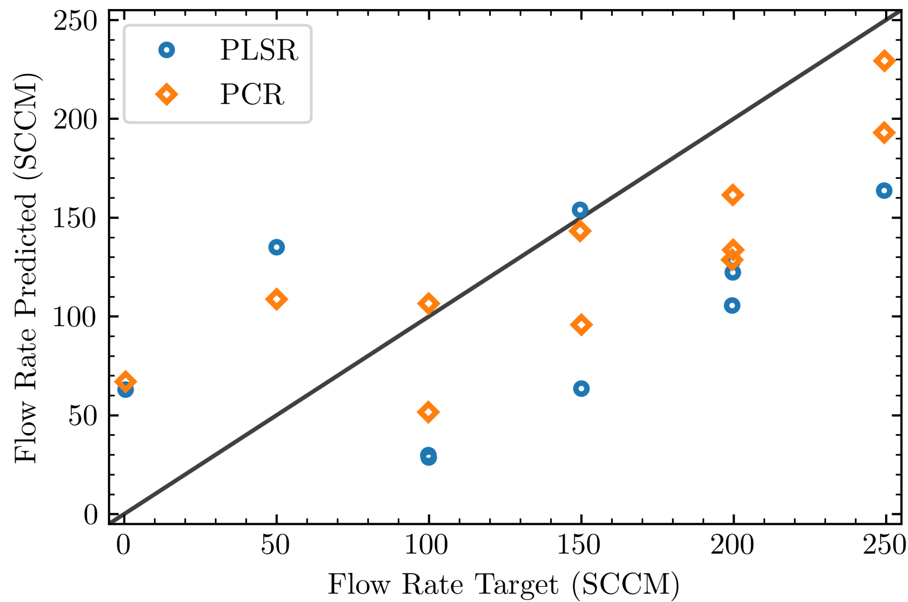

Figure 6.14: Sensor predicted flow rate with fitted response for both PLSR and PCR analysis against target flow rate.

Figure 6.16 shows the flow rate prediction of the ANN compared to the actual value. Visually, there is an immediate improvement compared to the linear methods. The R^2 for this prediction is 0.9444, this is higher than that of the PLSR and the PCR, at 0.0985 and 0.5721, respectively. Some variance does exist where the same flow rate is predicted twice, suggesting that the model could be improved further, however this is low enough to be compensated for in a real life application.

The average full scale error of the prediction is 2.99% for the flow rate and 1.51% for the gas concentration. In the devices reported by Gardner *et al.* [191], the first device presented has a full scale error of 2.9% for the flow prediction and 2% for the gas concentration. This means the ANN prediction using this novel GaN sensor is as good as the basic CMOS device for flow prediction and even better for the thermal conductivity. Although, the device presented here is not as good as the advanced sensor shown in that work. The advanced device incorporates holes in the membrane which improves thermal isolation and thus increases sensitivity. With this second device, they achieved

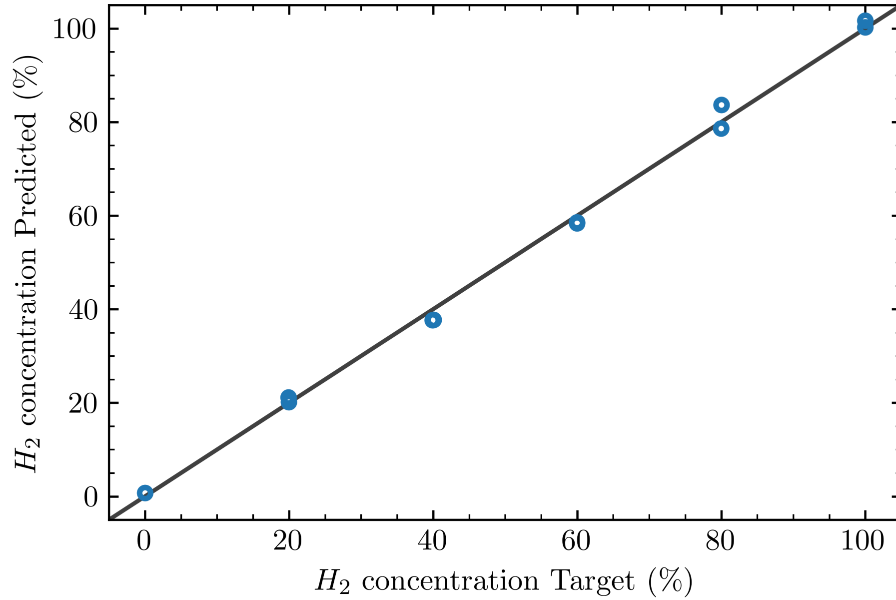

Figure 6.15: Sensor response compared with fitted response from the trained neural network for hydrogen concentration.

full scale errors of 0.24% and 0.98% for flow and thermal conductivity respectively. Anemometric theory says that improving thermal isolation increases the sensitivity of the device to fluid flow, as more heat is transferred via forced convection rather than conductively through the substrate. Given the comparable performance with the standard CMOS device, an avenue to explore to improve the GaN device would be to improve the thermal isolation of the membrane, which may lead to an enhanced performance such as seen with the CMOS device. Of course, improving thermal isolation by removing substance in the membrane does impact the structural integrity of the membrane.

Implementing an ANN has been shown above to be an effective method of simultaneously measuring the thermal conductivity and flow rate of a fluid.

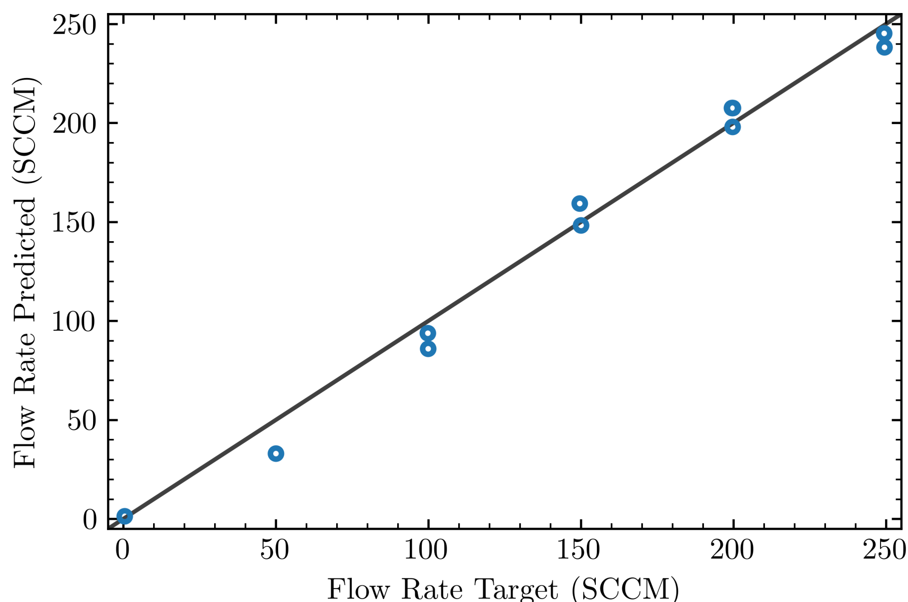

Figure 6.16: Sensor predicted flow rate compared with fitted response from the trained neural network against target flow rate.

6.5.4 Comparison between techniques

Tables 6.1 through to table 6.3 show some of the predictions and errors of the testing dataset. Note that the individual data points shown in the tables are a random subset of the full test set, the averages shown are calculated from the full dataset and so differ from the average of the 6 data points shown. The error calculated is the percentage full scale error. A full scale error is useful for contextualising the prediction errors in for practical applications.

Table 6.1 shows that the average error for the flow rate prediction is 26.08% which is the highest error of all models, the lowest being the ANN at 2.99%. For the gas concentration, the PLSR prediction is again the highest at 6% and the ANN the lowest at 1.51%. There is no clear correlation between the magnitude of the flow property and the level of error. This is something that could be explored further with a larger data set.

Table 6.1: PLSR result

Output		Prediction		Error	
Flow	$H_2\%$	Flow	$H_2\%$	Flow	$H_2\%$
50	100	135	96.3	33.99	3.71
100	60	29.8	57.0	27.99	2.91
0	100	63.5	95.2	25.04	4.74
199	60	128.5	56.7	28.50	3.24
150	40	63.5	33.5	34.62	6.54
250	80	259	74	3.81	6.02
			Average[1]	26.08	6.52

Table 6.2: PCR result

Output		Prediction		Error	
Flow	$H_2\%$	Flow	$H_2\%$	Flow	$H_2\%$
50	100	108.7	97	23.5	2.94
100	60	51.6	63	19.3	3.31
0	100	67.1	97	26.7	3.24
199	60	133.8	63	26.4	3.41
150	40	95.9	43	21.6	3.24
250	80	229.3	49	8	1.4
			Average	17.9	3.17

Table 6.3: ANN result

Output		Prediction		Error	
Flow	$H_2\%$	Flow	$H_2\%$	Flow	$H_2\%$
50	100	33	102	6.77	1.71
200	40	208	38	3.28	2.24
0	100	1.45	100	0.44	0.25
150	40	148	38	0.69	2.32
200	20	198	20	0.6	0.21
			Average	2.99	1.51

6.6 Conclusions

This chapter has presented a GaN-on-Si calorimetric flow sensor that can simultaneously measure the thermal conductivity and the flow rate of a fluid.

Both the use of linear multi-variate methods and machine learning techniques to differentiate between the two fluid properties have been discussed and critiqued for their suitability in this application. This chapter shows that hydrogen concentration can be predicted by both conventional linear methods and with ANN models. The flow rate on the other hand cannot be accurately determined by the linear methods.

The sensor consists of one gold hot-wire, as presented in chapter 4, and two thermopiles consisting of 5x Au/2DEG thermocouples connected in series, each placed with the hot junction on the GaN membrane and the reference junction on the substrate. In addition to showing a similar flow performance as in chapter 4, the sensor showed a clear response to the change in hydrogen concentration in the hydrogen-nitrogen gas mixture.

Two linear multi-variate methods were used to predict the gas concentration and flow rate. Both the PCR and PLSR methods were used with 2 components, and both were able to accurately predict the concentration of hydrogen in the fluid mix (R^2 of 0.9892 and 0.9477 respectively). Neither method could accurately predict the hydrogen concentration of the fluid, which would suggest that some non-linearity exists. It is on this basis that the ANN was created.

The ANN, using 3 layers, one hidden with 8 nodes with an input and output layer or 3 and 2 nodes respectively, was created and trained. The neural network was able to accurately predict the hydrogen concentration and flow rate using the three input variables from the upstream & downstream thermopiles, and the gold hot-wire, operating at 200 °C, with an R^2 of 0.9444 and 0.9956 for the flow rate and gas concentration respectively.

The ANN prediction had the lowest full scale percentage error of the prediction methods discussed. The mean error for flow rate was 2.99% for the ANN, and 17.9% and 26.08% for the PCR and PLSR methods. The errors of all three methods were lower for hydrogen concentration at 1.51%, 3.17%, and 6.52%, respectively.

The use of the ANN to decouple flow and thermal conductivity using a GaN based calorimetric has been shown to be as accurate as some existing

CMOS devices employing a similar technique.

Chapter 7

Conclusions & Further Work

This thesis has presented original work on the development of GaN-on-Si sensors, working towards a platform to develop thermal sensors for harsh environments.

7.1 Summary

Chapter 1 highlighted the motivation and applications for these types of devices. On overview of the current state of the market was given, followed by a discussion of opportunities in certain application spaces that could be exploited. This chapter discussed the need and desire for specifically flow and thermal conductivity sensors for these applications. The challenges faced by conventional materials were highlighted and the ability of GaN based devices to overcome these challenges was presented.

Chapter 2 gives the theoretical grounding for the research undertaken here. This chapter discusses the physical phenomena at play in thermal flow sensors, and presents the equations describing the fluid, heat transfer, and electronic characteristics. In this chapter the 3 main thermal flow sensor configurations and operational modes were presented, along with the relative advantages and disadvantages of each one. The chapter then discussed the existing literature on these devices. The literature contained only one flow sensor that was made in a GaN process, which was published in 2019 and

based on a hot-wire configuration rather than the hot-film and calorimetric types presented in this work. Various technologies were discussed for their implementation of pressure and flow sensors. The benefits of GaN over other materials was discussed, and the operation and device physics of GaN devices discussed.

Chapter 3 presents modelling work carried out to simulate the devices discussed. FEM modelling was shown for the flow sensors channel. The aim of this model was to optimise the length of the flow channel to ensure a laminar flow over the sensor, while at the same time minimising the length to meet the minimisation objectives of the MEMS devices. The model simulated 3 different channel lengths from 20 mm to 120 mm, for flow rates from 0.1 SLPM to 2 SLPM. The modelling showed that the flow was laminar in the 20 mm up to around 1 SLPM, where the boundary layer was beginning to show signs of turbulence. The 120 mm channel showed laminar performance up to 2 SLPM. It was decided to use the smallest channel to meet the minimisation criteria of the device, and test experimentally to find the flow rate where the boundary ceased to be laminar.

This chapter then presented a model of the ring-HEMT pressure sensor. This model comprised of two parts. First was the FEM based 3D strain model of the membrane, done in COMSOL Multiphysics, which was based on the elastic constants of the material, and showed the displacement and strain in the membrane. This model was used to determine the point in the membrane where the strain peaked, which was approximately 24 µm from the edge of the membrane. This corresponds to approximately the location of the centre of the gate of the ring-HEMT embedded in the membrane. The FEM model was simulated for over a pressure range from 0-1 MPa. This is a much larger range than the devices will be tested in. The average vertical displacement of the membrane was 6.8 µm at 1 MPa. The strain data from the FEM model were fed into an analytical equation based mode, that included additional strains such as the lattice mismatch strain, to determine the percentage change in the piezoelectric charge over pressure, and thus the response of the carrier concentration to pressure. Over a smaller pressure range, the model showed that the total polarisation at the AlGaN/GaN interface increased by 3.5%

with an applied pressure of 100 kPa.

Chapter 4 presents the two AlGaN/GaN, GaN-on-Si flow sensor designs. This first is the gold hot-wire device, the second is the 2DEG hot-wire design. Electrothermal characterisation of the gold hot-wire showed a TCR of 0.00302 %/K, and an electrothermal efficiency of 1.04 K/mW and 0.21 K/mW for the released membrane device and unreleased devices, respectively. This gave a peak sensitivity of 110 mV/SLPM at a hot-wire temperature of 250°C. The electrothermal efficiency of the 2DEG devices were presented both with a released membrane and unreleased, and showed an electrothermal efficiency of 0.9843 K/mW for the released membrane versus 0.1663 K/mW for the bulk device. The TCR of the 2DEG based heater device was measured as 0.0114 %/K, which is a 275% improvement compared to gold. The device presented had a peak sensitivity of 569 mV/SLPM, with a DC power consumption of 25 mW. Showing an improved sensitivity at a lower DC power consumption than the gold device.

Chapter 5 presents a ring-HEMT pressure sensor fabricated in this specific AlGaN/GaN process. The HEMT was characterised various characteristics extracted. Firstly, the threshold voltage measured to be -2.3 V, and secondly, the AlGaN/GaN barrier breakdown occurred at V_g = 1 V. After measuring the output characteristics, the device was found to be entering the saturation region. The sensors were characterised between 0 and 100 kPa, with the HEMT operating in both the linear and saturation region. The device has a peak sensitivity of 41.15 µA/kPa with a DC power consumption of 88.73 mW when V_g =1 V and V_d = 5 V.

Chapter 6 uses the flow sensors described in chapter 4, and implements them in a calorimetric configuration with Au/2DEG thermopiles, as a thermal conductivity sensor. This chapter describe the development of a gas testing rig to perform the experiment and the results obtained. The flow sensor is tested with a flow of varying gas concentration, between different concentrations of hydrogen and nitrogen. Using the 3 sensors on the device, various post processing methods are used to simultaneously measure flow rate and gas concentration. PCR and PLSR were used first. These methods were able to accurately determine the hydrogen concentration of the fluid, but not the flow

rate, with a full scale error of 17.9% and 26.08%, respectively, for the flow rate and 3.17% and 6.52% for the gas concentration. This response was improved through the use of an ANN. Using an ANN of 1 hidden layer, it was possible to predict both the flow rate and the gas concentration, with a full scale error of 2.99% and 1.51%, respectively.

7.2 Conclusions

The main achievement of this work is that it is the first demonstration of a flow sensor, and a thermal conductivity sensor fabricated in a GaN fabrication process of any kind.

Chapter 4 shows the first demonstration of a flow sensor fabricated in GaN. The first device presented here uses a gold hot-wire to realise a thermal flow sensor. The performance of this gold how-wire device is comparable to the existing state-of-the-art devices made of silicon reported in literature. Integrating this device with a custom flow chamber makes the measurements valid up to 1.7 SLPM.

The first demonstration of a 2DEG used as a resistive heater for detecting flow has been reported. This 2DEG is formed from an AlGaN/GaN heterostructure. The electrothermal characterisation of this shows the temperature coefficient of resistance exceeds that of most metals typically used as heater for flow sensors. The response of this device to fluid flow shows that its sensitivity exceeds that of so me of the devices reported in literature, with a lower DC power consumption.

The limitation placed on the maximum flow rate of the devices presented is the flow chamber dimensions. The modelling in this work, coupled with the experimental results, show that the brake in King's law present in the flow sensor response is due to the presence of turbulence in the chamber at approximately 1.7 SLPM. This indicates that the maximum flow rate that the devices can detect is much higher than 1.7 SLPM, which can be achieved by focusing efforts on re-designing the flow chamber geometry.

The pressure sensor in chapter 5 shows that the AlGaN/GaN ring-

HEMT design fabricated in this process operates comparably with state-of-the-art devices. This paves the way to incorporate a pressure sensors such as this in a combo chip configuration with the flow and thermal conductivity sensors.

Chapter 6 demonstrates the first calorimetric flow sensor fabricated in a GaN process. This sensor is presented as both a flow sensor and as a thermal conductivity sensor, that uses a thermopile comprising of five 2DEG/Gold thermocouples as upstream and downstream temperature sensors. Using an ANN to process the outputs of these three sensing elements, it was demonstrated that the effect of the flow rate can be decoupled from the thermal conductivity of the fluid. This method was able to predict the flow rate and gas concentration of a N_2/H_2 mix better than some CMOS based devices using a similar technique.

This work overall proves that it is possible to fabricate these gas sensors in a GaN process, with comparable or, in some cases, better performance than mass produced silicon equivalents. While at room temperature these devices are comparable to silicon in terms of performance, price wise, the mass produced silicon based devices will be cheaper. This work provides the platform to build upon to leverage the harsh environment benefits afforded by GaN.

7.3 Further Work

There are several ways to extend the work done in this thesis. This thesis has presented a proof of concept for developing these devices on a GaN-on-Si platform. More work can be done to exploit the specific benefits of GaN.

- Thermoelectronic flow sensor. While the designs for the flow sensors presented in this work contain mini-HEMTs as thermoelectronic sensing elements for calorimetric configured operation, issues in the fabrication meant they could not be characterised and tested. The design of these devices could be revised in an attempt to overcome the issues.

- Combo chip. With all 3 different sensors proven, it would now be possible to explore combining them onto one chip die to act as a combined pressure, flow, thermal conductivity, and temperature sensor. A combo chip would be able to gather as much information about a flow with a smaller overall package than having the devices as individuals.

- High temperature testing. Theoretically, the devices presented in this work could be operational up to 600 °C. No high temperature testing was presented here due to the technical barriers that would need to be overcome. Standard FR4 PCBs, such as the ones used in the packaging here, are only rated to 130°C. Packaging high temperature electronics is still a major obstacle in the large scale adoption.

- Radiation testing. The change in electronic characteristics with respect to radiation could be investigated. A Cobalt-60 source is typically used in radiation testing, with the sample exposed over a period of time (days and months) to simulate long term exposure.

- Thermal conductivity sensor. This work presented the response of the thermal conductivity sensor in response to a hydrogen nitrogen mix, because of hydrogen's relatively high thermal conductivity. Other gases of interest, such as CO, CO_2, or NH_3, all of which are present in some combustion applications, could be tested.

Bibliography

[1] V. Cimalla, J. Pezoldt, and O. Ambacher, "Group III nitride and SiC based MEMS and NEMS: materials properties, technology and applications," *Journal of Physics D: Applied Physics*, vol. 40, pp. 6386,.

[2] O. Ambacher, J. Majewski, C. Miskys, A. Link, M. Hermann, M. Eickhoff, M. Stutzmann, F. Bernardini, V. Fiorentini, V. Tilak *et al.*, "Pyroelectric properties of Al(In)GaN/GaN hetero-and quantum well structures," *Journal of physics: condensed matter*, vol. 14, no. 13, p. 3399, 2002.

[3] N. Nguyen, "Micromachined flow sensors—a review," *Flow measurement and Instrumentation*, vol. 8, no. 1, pp. 7–16, 1997.

[4] N. Svedin, E. Stemme, and G. Stemme, "A new bi-directional gas-flow sensor based on lift force," in *Proceedings of International Solid State Sensors and Actuators Conference (Transducers' 97)*, vol. 1. IEEE, 1997, pp. 145–148.

[5] Y. Yang, N. Chen, C. Tucker, J. Engel, S. Pandya, and C. Liu, "From artificial hair cell sensor to artificial lateral line system: development and application," in *2007 IEEE 20th International Conference on Micro Electro Mechanical Systems (MEMS)*. IEEE, 2007, pp. 577–580.

[6] A. Kottapalli, M. Asadnia, J. Miao, and M. Triantafyllou, "Harbor seal whisker inspired flow sensors to reduce vortex-induced vibrations," in *2015 28th IEEE International Conference on Micro Electro Mechanical Systems (MEMS)*. IEEE, 2015, pp. 889–892.

[7] R. Kumar, "Sensor market by type, technology, and end user: Global opportunity analysis and industry forecast, 2012-2025," *Technical Report.*

[8] P. G. Neudeck, R. S. Okojie, and L.-Y. Chen, "High-temperature electronics-a role for wide bandgap semiconductors?" *Proceedings of the IEEE*, vol. 90, no. 6, pp. 1065–1076, 2002.

[9] H. A. Mantooth, M. D. Glover, and P. Shepherd, "Wide bandgap technologies and their implications on miniaturizing power electronic systems," *IEEE Journal of emerging and selected topics in Power Electronics*, vol. 2, no. 3, pp. 374–385, 2014.

[10] H. Morkoc, S. Strite, G. Gao, M. Lin, B. Sverdlov, and M. Burns, "Large-band-gap SiC, III-V nitride, and II-VI ZnSe-based semiconductor device technologies," *Journal of Applied physics*, vol. 76, no. 3, pp. 1363–1398, 1994.

[11] D. Maier, M. Alomari, N. Grandjean, J.-F. Carlin, M.-A. Diforte-Poisson, C. Dua, S. Delage, and E. Kohn, "InAlN/GaN HEMTs for operation in the 1000°C regime: A first experiment," *IEEE Electron Device Letters*, vol. 33, no. 7, pp. 985–987, 2012.

[12] F. Medjdoub, J. Carlin, C. Gaquiere, N. Grandjean, and E. Kohn, "Status of the emerging InAlN/GaN power HEMT technology," *The Open Electrical & Electronic Engineering Journal*, vol. 2, no. 1, 2008.

[13] J. Grant, R. Bates, W. Cunningham, A. Blue, J. Melone, F. McEwan, J. Vaitkus, E. Gaubas, and V. O'Shea, "GaN as a radiation hard particle detector," *Nuclear Instruments and Methods in Physics Research Section A: Accelerators, Spectrometers, Detectors and Associated Equipment*, vol. 576, no. 1, pp. 60–65, 2007.

[14] P. Hazdra and S. Popelka, "Radiation resistance of wide-bandgap semiconductor power transistors," *Physica status solidi (a)*, vol. 214, no. 4, p. 1600447, 2017.

[15] A. Abderrahmane, P. J. Ko, H. Okada, S.-I. Sato, T. Ohshima, and A. Sandhu, "Proton irradiation enhancement of low-field negative magnetoresistance sensitivity of AlGaN/GaN-based magnetic sensor at cryogenic temperature," *IEEE Electron Device Letters*, vol. 35, no. 11, pp. 1130–1132, 2014.

[16] P. Chyurlia, F. Semond, T. Lester, J. Bardwell, S. Rolfe, H. Tang, and N. Tarr, "Monolithic integration of AlGaN/GaN HFET with MOS on silicon (111) substrates," *Electronics letters*, vol. 46, pp. 253–254,.

[17] N. Tyler, "Demand for automotive sensors is booming," Decmber 2016. [Online]. Available: https://www.newelectronics.co.uk/electronics-technology/automotive-sensors-market-is-booming/149323/

[18] M. Kraft and N. M. White, "MEMS for automotive and aerospace applications," 2013.

[19] A. T. Basilevsky and J. W. Head, "The surface of venus," *Reports on Progress in Physics*, vol. 66, no. 10, p. 1699, 2003.

[20] T. S. Balint, J. A. Cutts, E. A. Kolawa, and C. E. Peterson, "Extreme environment technologies for space and terrestrial applications," in *Space Exploration Technologies*, vol. 6960. International Society for Optics and Photonics, 2008, p. 696006.

[21] S. Amor, N. André, V. Kilchytska, F. Tounsi, B. Mezghani, P. Gérard, Z. Ali, F. Udrea, D. Flandre, and L. Francis, "In-situ thermal annealing of on-membrane silicon-on-insulator semiconductor-based devices after high gamma dose irradiation," *Nanotechnology*, vol. 28, no. 18, p. 184001, 2017.

[22] K.-a. Son, A. Liao, G. Lung, M. Gallegos, T. Hatake, R. D. Harris, L. Z. Scheick, and W. D. Smythe, "GaN-based high temperature and radiation-hard electronics for harsh environments," *Nanoscience and Nanotechnology Letters*, vol. 2, no. 2, pp. 89–95, 2010.

[23] M. P. Petkov, "The effects of space environments on electronic components," 2003.

[24] Y. Su, A. Evans, A. Brunnschweiler, and G. Ensell, “Characterization of a highly sensitive ultra-thin piezoresistive silicon cantilever probe and its application in gas flow velocity sensing,” *Journal of Micromechanics and Microengineering*, vol. 12, no. 6, p. 780, 2002.

[25] Q. Zhang, W. Ruan, H. Wang, Y. Zhou, Z. Wang, and L. Liu, “A self-bended piezoresistive microcantilever flow sensor for low flow rate measurement,” *Sensors and Actuators A: Physical*, vol. 158, no. 2, pp. 273–279, 2010.

[26] B. Tian, H. Li, N. Yang, H. Liu, and Y. Zhao, “A MEMS-based flow sensor with membrane cantilever beam array structure,” in *2017 IEEE 12th International Conference on Nano/Micro Engineered and Molecular Systems (NEMS)*. IEEE, 2017, pp. 185–189.

[27] A. K. Dhonkal, V. Agarwal, and K. Sengar, “Sensitivity of the mems based piezoresistive wind speed sensor with comparative study of different shapes of paddles,” *Int. Res. J. Eng. Technol.*, vol. 4, no. 2, pp. 1693–1697, 2017.

[28] Y. Su, A. Evans, and A. Brunnschweiler, “Micromachined silicon cantilever paddles with piezoresistive readout for flow sensing,” *Journal of Micromechanics and Microengineering*, vol. 6, no. 1, p. 69, 1996.

[29] S. Peleshanko, M. D. Julian, M. Ornatska, M. E. McConney, M. C. LeMieux, N. Chen, C. Tucker, Y. Yang, C. Liu, J. A. Humphrey *et al.*, “Hydrogel-encapsulated microfabricated haircells mimicking fish cupula neuromast,” *Advanced materials*, vol. 19, no. 19, pp. 2903–2909, 2007.

[30] N. Chen, C. Tucker, J. M. Engel, Y. Yang, S. Pandya, and C. Liu, “Design and characterization of artificial haircell sensor for flow sensing with ultrahigh velocity and angular sensitivity,” *Journal of microelectromechanical systems*, vol. 16, no. 5, pp. 999–1014, 2007.

[31] D. Moser, R. Lenggenhager, and H. Baltes, “Silicon gas flow sensors using industrial CMOS and bipolar IC technology,” *Sensors and Actuators A: Physical*, vol. 27, no. 1-3, pp. 577–581, 1991.

[32] R. Mathew and A. R. Sankar, "A review on surface stress-based miniaturized piezoresistive SU-8 polymeric cantilever sensors," *Nano-micro Letters*, vol. 10, no. 2, pp. 1–41, 2018.

[33] A. Kottapalli, C. Tan, M. Olfatnia, J. Miao, G. Barbastathis, and M. Triantafyllou, "A liquid crystal polymer membrane MEMS sensor for flow rate and flow direction sensing applications," *Journal of Micromechanics and Microengineering*, vol. 21, no. 8, p. 085006, 2011.

[34] R. Hagihghi, A. Razmjou, Y. Orooji, M. E. Warkiani, and M. Asadnia, "A miniaturized piezoresistive flow sensor for real-time monitoring of intravenous infusion," *Journal of Biomedical Materials Research Part B: Applied Biomaterials*, vol. 108, no. 2, pp. 568–576, 2020.

[35] H. Herzog, A. Klein, H. Bleckmann, P. Holik, S. Schmitz, G. Siebke, S. Tätzner, M. Lacher, and S. Steltenkamp, "μ-biomimetic flow-sensors—introducing light-guiding PDMS structures into MEMS," *Bioinspiration & Biomimetics*, vol. 10, no. 3, p. 036001, 2015.

[36] D. Celentano, D. Wimmer, L. Colabella, and A. P. Cisilino, "Viscoelastic mechanical characterization of a short-fiber reinforced polyethylene tube: Experiments and modelling," *International Journal of Pressure Vessels and Piping*, vol. 134, pp. 82–91, 2015.

[37] J. Chen, J. Engel, and C. Liu, "Development of polymer-based artificial haircell using surface micromachining and 3D assembly," in *TRANSDUCERS'03. 12th International Conference on Solid-State Sensors, Actuators and Microsystems. Digest of Technical Papers (Cat. No. 03TH8664)*, vol. 2. IEEE, 2003, pp. 1035–1038.

[38] A. G. P. Kottapalli, M. Asadnia, J. Miao, and M. Triantafyllou, "Soft polymer membrane micro-sensor arrays inspired by the mechanosensory lateral line on the blind cavefish," *Journal of Intelligent Material Systems and Structures*, vol. 26, no. 1, pp. 38–46, 2015.

[39] A. G. P. Kottapalli, M. Bora, M. Asadnia, J. Miao, S. S. Venkatraman, and M. Triantafyllou, "Nanofibril scaffold assisted MEMS artificial hy-

drogel neuromasts for enhanced sensitivity flow sensing," *Scientific Reports*, vol. 6, no. 1, pp. 1–12, 2016.

[40] M. Asadnia, A. Kottapalli, J. Miao, A. Randles, A. Sabbagh, P. Kropelnicki, and J. Tsai, "High temperature characterization of PZT (0.52/0.48) thin-film pressure sensors," *Journal of Micromechanics and Microengineering*, vol. 24, no. 1, p. 015017, 2013.

[41] H. Khan, A. Razmjou, M. Ebrahimi Warkiani, A. Kottapalli, and M. Asadnia, "Sensitive and flexible polymeric strain sensor for accurate human motion monitoring," *Sensors*, vol. 18, no. 2, p. 418, 2018.

[42] D. Sengupta, A. Kottapalli, S. Chen, J. Miao, C. Kwok, M. Triantafyllou, M. Warkiani, and M. Asadnia, "Characterization of single polyvinylidene fluoride (PVDF) nanofiber for flow sensing applications," *AIP Advances*, vol. 7, no. 10, p. 105205, 2017.

[43] S. R. Anton and H. A. Sodano, "A review of power harvesting using piezoelectric materials (2003–2006)," *Smart materials and Structures*, vol. 16, no. 3, p. R1, 2007.

[44] T. Sharma, S.-S. Je, B. Gill, and J. X. Zhang, "Patterning piezoelectric thin film PVDF–TrFE based pressure sensor for catheter application," *Sensors and Actuators A: physical*, vol. 177, pp. 87–92, 2012.

[45] M. Asadnia, A. G. P. Kottapalli, J. Miao, M. E. Warkiani, and M. S. Triantafyllou, "Artificial fish skin of self-powered micro-electromechanical systems hair cells for sensing hydrodynamic flow phenomena," *Journal of the Royal Society Interface*, vol. 12, no. 111, p. 20150322, 2015.

[46] A. Kottapalli, M. Asadnia, H. Hans, J. Miao, and M. Triantafyllou, "Harbor seal inspired MEMS artificial micro-whisker sensor," in *2014 IEEE 27th International Conference on Micro Electro Mechanical Systems (MEMS)*. IEEE, 2014, pp. 741–744.

[47] F. Ejeian, S. Azadi, A. Razmjou, Y. Orooji, A. Kottapalli, M. E. Warkiani, and M. Asadnia, "Design and applications of MEMS flow

sensors: A review," *Sensors and Actuators A: Physical*, vol. 295, pp. 483–502, 2019.

[48] M. Raman, T. Kifle, E. Bhattacharya, and K. Bhat, "Physical model for the resistivity and temperature coefficient of resistivity in heavily doped polysilicon," *IEEE Transactions on Electron Devices*, vol. 53, no. 8, pp. 1885–1892, 2006.

[49] D. Dittmann, R. Ahrens, Z. Rummler, K. Schlote-Holubek, and W. K. Schomburg, "Low-cost flow transducer fabricated with the amanda-process," in *Transducers' 01 Eurosensors XV*. Springer, 2001, pp. 1444–1447.

[50] E. Meng, *Biomedical microsystems*. CRC Press, 2011.

[51] K. G. Kreider and F. DiMeo, "Platinum/palladium thin-film thermocouples for temperature measurements on silicon wafers," *Sensors and Actuators A: Physical*, vol. 69, no. 1, pp. 46–52, 1998.

[52] F. Mailly, A. Giani, R. Bonnot, P. Temple-Boyer, F. Pascal-Delannoy, A. Foucaran, and A. Boyer, "Anemometer with hot platinum thin film," *Sensors and Actuators A: Physical*, vol. 94, no. 1-2, pp. 32–38, 2001.

[53] J. Van Honschoten, J. Van Baar, H. De Bree, T. Lammerink, G. Krijnen, and M. Elwenspoek, "Application of a microflown as a low-cost level sensor," *Journal of micromechanics and microengineering*, vol. 10, no. 2, p. 250, 2000.

[54] J. T. Kuo, L. Yu, and E. Meng, "Micromachined thermal flow sensors—a review," *Micromachines*, vol. 3, no. 3, pp. 550–573, 2012.

[55] C. Liu, J.-B. Huang, Z. Zhu, F. Jiang, S. Tung, Y.-C. Tai, and C.-M. Ho, "A micromachined flow shear-stress sensor based on thermal transfer principles," *Journal of Microelectromechanical Systems*, vol. 8, no. 1, pp. 90–99, 1999.

[56] A. De Luca, C. Falco, E. L. Gardner, J. D. Coull, and F. Udrea, "Diode-based CMOS MEMS thermal flow sensors," in *2017 19th Inter-*

national Conference on Solid-State Sensors, Actuators and Microsystems (TRANSDUCERS). IEEE, 2017, pp. 2211–2214.

[57] F. M. White, "Fluid Mechanics, McGraw-Hill," *New York*, pp. 560–561, 1986.

[58] N.-T. Nguyen, S. T. Wereley, and S. A. M. Shaegh, *Fundamentals and applications of microfluidics*. Artech house, 2019.

[59] C.-H. Wu, D. Kang, P.-H. Chen, and Y.-C. Tai, "MEMS thermal flow sensors," *Sensors and Actuators A: Physical*, vol. 241, pp. 135–144, 2016.

[60] A. A. Cabrita, R. Mendes, and D. A. Quintela, "Thermistor based, low velocity isothermal, air flow sensor," *Measurement Science and Technology*, vol. 27, no. 3, p. 035307, 2016.

[61] B. Van Oudheusden, "Silicon thermal flow sensors," *Sensors and Actuators A: Physical*, vol. 30, no. 1-2, pp. 5–26, 1992.

[62] H.-M. Chuang, K.-B. Thei, S.-F. Tsai, and W.-C. Liu, "Temperature-dependent characteristics of polysilicon and diffused resistors," *IEEE Transactions on Electron Devices*, vol. 50, no. 5, pp. 1413–1415, 2003.

[63] E. Yoon and K. D. Wise, "An integrated mass flow sensor with on-chip CMOS interface circuitry," *IEEE Transactions on Electron Devices*, vol. 39, no. 6, pp. 1376–1386, 1992.

[64] G. Kaltsas and A. Nassiopoulou, "Novel C-MOS compatible monolithic silicon gas flow sensor with porous silicon thermal isolation," *Sensors and Actuators A: Physical*, vol. 76, no. 1-3, pp. 133–138, 1999.

[65] A. Van der Wiel, C. Linder, N. De Rooij, and A. Bezinge, "A liquid velocity sensor based on the hot-wire principle," *Sensors and Actuators A: Physical*, vol. 37, pp. 693–697, 1993.

[66] R. Kersjes, J. Eichholz, A. Langerbein, Y. Manoli, and W. Mokwa, "An integrated sensor for invasive blood-velocity measurement," *Sensors and Actuators A: Physical*, vol. 37, pp. 674–678, 1993.

[67] T. Dinh, H.-P. Phan, A. Qamar, P. Woodfield, N.-T. Nguyen, and D. V. Dao, "Thermoresistive effect for advanced thermal sensors: Fundamentals, design considerations, and applications," *Journal of Microelectromechanical Systems*, vol. 26, no. 5, pp. 966–986, 2017.

[68] E. F.-C. Meng, "MEMS technology and devices for a micro fluid dosing system," Ph.D. dissertation, California Institute of Technology, 2003.

[69] E. L. Gardner, A. De Luca, T. Vincent, R. G. Jones, J. W. Gardner, and F. Udrea, "Thermal conductivity sensor with isolating membrane holes," in *2019 IEEE SENSORS*. IEEE, 2019, pp. 1–4.

[70] W. Xu, B. Gao, S. Ma, A. Zhang, Y. Chiu, and Y.-K. Lee, "Low-cost temperature-compensated thermoresistive micro calorimetric flow sensor by using 0.35 μm CMOS MEMS technology," in *2016 IEEE 29th International Conference on Micro Electro Mechanical Systems (MEMS)*. IEEE, 2016, pp. 189–192.

[71] P. Bruschi and M. Piotto, "Determination of the wind speed and direction by means of fluidic-domain signal processing," *IEEE Sensors Journal*, vol. 18, no. 3, pp. 985–994, 2017.

[72] M. Dijkstra, M. J. de Boer, J. W. Berenschot, T. S. Lammerink, R. J. Wiegerink, and M. Elwenspoek, "Miniaturized thermal flow sensor with planar-integrated sensor structures on semicircular surface channels," *Sensors and Actuators A: Physical*, vol. 143, no. 1, pp. 1–6, 2008.

[73] J. Weiss, E. Jondeau, A. Giani, B. Charlot, and P. Combette, "Static and dynamic calibration of a MEMS calorimetric shear-stress sensor," *Sensors and Actuators A: Physical*, vol. 265, pp. 211–216, 2017.

[74] G.-H. Ding, B.-H. Ma, J.-J. Deng, W.-Z. Yuan, and K. Liu, "Accurate measurements of wall shear stress on a plate with elliptic leading edge," *Sensors*, vol. 18, no. 8, p. 2682, 2018.

[75] H. Sturm and W. Lang, "Membrane-based thermal flow sensors on flexible substrates," *Sensors and Actuators A: Physical*, vol. 195, pp. 113–122, 2013.

[76] V. Balakrishnan, H.-P. Phan, T. Dinh, D. V. Dao, and N.-T. Nguyen, "Thermal flow sensors for harsh environments," *Sensors*, vol. 17, no. 9, p. 2061, 2017.

[77] H. Muhammad, C. Oddo, L. Beccai, C. Recchiuto, C. Anthony, M. Adams, M. Carrozza, D. Hukins, and M. Ward, "Development of a bioinspired MEMS based capacitive tactile sensor for a robotic finger," *Sensors and Actuators A: Physical*, vol. 165, no. 2, pp. 221–229, 2011.

[78] Y. Hijikata, *Physics and technology of silicon carbide devices.* BoD–Books on Demand, 2012.

[79] J. Sanchez, "Semiconductor strain-gauge pressure sensors," *Instruments and Control Systems*, vol. 74, pp. 117–120, 1963.

[80] P. Song, Z. Ma, J. Ma, L. Yang, J. Wei, Y. Zhao, M. Zhang, F. Yang, and X. Wang, "Recent progress of miniature MEMS pressure sensors," *Micromachines*, vol. 11, no. 1, p. 56, 2020.

[81] K. B. Albaugh, "Electrode phenomena during anodic bonding of silicon to sodium borosilicate glass," *Journal of the Electrochemical Society*, vol. 138, no. 10, p. 3089, 1991.

[82] D. Sparks, G. Queen, R. Weston, G. Woodward, M. Putty, L. Jordan, S. Zarabadi, and K. Jayakar, "Wafer-to-wafer bonding of nonplanarized MEMS surfaces using solder," *Journal of Micromechanics and Microengineering*, vol. 11, no. 6, p. 630, 2001.

[83] M. A. Schmidt, "Wafer-to-wafer bonding for microstructure formation," *Proceedings of the IEEE*, vol. 86, no. 8, pp. 1575–1585, 1998.

[84] S. Guo, H. Eriksen, K. Childress, A. Fink, and M. Hoffman, "High temperature smart-cut SOI pressure sensor," *Sensors and Actuators A: Physical*, vol. 154, no. 2, pp. 255–260, 2009.

[85] R. S. Okojie, D. Lukco, V. Nguyen, and E. Savrun, "4H-SiC piezoresistive pressure sensors at 800°C with observed sensitivity recovery," *IEEE Electron Device Letters*, vol. 36, no. 2, pp. 174–176, 2014.

[86] T. P. Chow, "Wide bandgap semiconductor power devices for energy efficient systems," in *2015 IEEE 3rd Workshop on Wide Bandgap Power Devices and Applications (WiPDA).* IEEE, 2015, pp. 402–405.

[87] U. K. Mishra, L. Shen, T. E. Kazior, and Y.-F. Wu, "GaN-based RF power devices and amplifiers," *Proceedings of the IEEE*, vol. 96, no. 2, pp. 287–305, 2008.

[88] N. Kaminski and O. Hilt, "SiC and GaN devices–wide bandgap is not all the same," *IET Circuits, Devices & Systems*, vol. 8, no. 3, pp. 227–236, 2014.

[89] J. Milligan, S. Sheppard, W. Pribble, Y.-F. Wu, G. Muller, and J. Palmour, "SiC and GaN wide bandgap device technology overview," in *2007 IEEE Radar Conference.* IEEE, 2007, pp. 960–964.

[90] B. Kang, S. Kim, F. Ren, J. Johnson, R. Therrien, P. Rajagopal, J. Roberts, E. Piner, K. Linthicum, S. Chu *et al.*, "Pressure-induced changes in the conductivity of AlGaN/ GaN high-electron mobility-transistor membranes," *Applied Physics Letters*, vol. 85, no. 14, pp. 2962–2964, 2004.

[91] E. D. Le Boulbar, M. J. Edwards, S. Vittoz, G. Vanko, K. Brinkfeldt, L. Rufer, P. Johander, T. Lalinskỳ, C. R. Bowen, and D. W. Allsopp, "Effect of bias conditions on pressure sensors based on AlGaN/GaN high electron mobility transistor," *Sensors and Actuators A: Physical*, vol. 194, pp. 247–251, 2013.

[92] M. J. Edwards, E. D. Le Boulbar, S. Vittoz, G. Vanko, K. Brinkfeldt, L. Rufer, P. Johander, T. Lalinskỳ, C. R. Bowen, and D. W. Allsopp, "Pressure and temperature dependence of AlGaN/GaN high electron mobility transistor based sensors on a sapphire membrane," *Physica Status Solidi c*, vol. 9, no. 3-4, pp. 960–963, 2012.

[93] M. Eickhoff, O. Ambacher, G. Krötz, and M. Stutzmann, "Piezoresistivity of $Al_xGa_{1-x}N$ layers and $Al_xGa_{1-x}N$/GaN heterostructures," *Journal of Applied Physics*, vol. 90, no. 7, pp. 3383–3386, 2001.

[94] B. Kang, S. Kim, J. Kim, F. Ren, K. Baik, S. Pearton, B. Gila, C. Abernathy, C.-C. Pan, G.-T. Chen *et al.*, "Effect of external strain on the conductivity of AlGaN/GaN high-electron-mobility transistors," *Applied Physics Letters*, vol. 83, no. 23, pp. 4845–4847, 2003.

[95] A. D. Koehler, A. Gupta, M. Chu, S. Parthasarathy, K. J. Linthicum, J. W. Johnson, T. Nishida, and S. E. Thompson, "Extraction of AlGaN/GaN hemt gauge factor in the presence of traps," *IEEE Electron device letters*, vol. 31, no. 7, pp. 665–667, 2010.

[96] K. Yao, S. Khandelwal, F. Sammoura, A. Kazama, C. Hu, and L. Lin, "Piezoelectricity-induced schottky barrier height variations in AlGaN/GaN high electron mobility transistors," *IEEE Electron Device Letters*, vol. 36, no. 9, pp. 902–904, 2015.

[97] S. Chu, F. Ren, S. Pearton, B. Kang, S. Kim, B. Gila, C. Abernathy, J.-I. Chyi, W. Johnson, and J. Lin, "Piezoelectric polarization-induced two dimensional electron gases in AlGaN/GaN heteroepitaxial structures: Application for micro-pressure sensors," *Materials Science and Engineering: A*, vol. 409, no. 1-2, pp. 340–347, 2005.

[98] A. S. Yalamarthy and D. G. Senesky, "Strain-and temperature-induced effects in AlGaN/GaN high electron mobility transistors," *Semiconductor Science and Technology*, vol. 31, no. 3, p. 035024, 2016.

[99] T. Lalinskỳ, M. Držík, G. Vanko, M. Vallo, V. Kutiš, J. Bruncko, Š. Haščík, J. Jakovenko, and M. Husák, "Piezoelectric response of AlGaN/GaN-based circular-HEMT structures," *Microelectronic engineering*, vol. 88, no. 8, pp. 2424–2426, 2011.

[100] G. Vanko, M. Držík, M. Vallo, T. Lalinskỳ, V. Kutiš, S. Stančík, I. Rỳger, and A. Benčurová, "AlGaN/GaN c-hemt structures for dynamic stress detection," *Sensors and Actuators A: Physical*, vol. 172, no. 1, pp. 98–102, 2011.

[101] J. Dzuba, G. Vanko, M. Držík, I. Rỳger, V. Kutiš, J. Zehetner, and T. Lalinskỳ, "AlGaN/GaN diaphragm-based pressure sensor with di-

rect high performance piezoelectric transduction mechanism," *Applied Physics Letters*, vol. 107, no. 12, p. 122102, 2015.

[102] C. A. Chapin, R. A. Miller, K. M. Dowling, R. Chen, and D. G. Senesky, "InAlN/GaN high electron mobility micro-pressure sensors for high-temperature environments," *Sensors and Actuators A: Physical*, vol. 263, pp. 216–223, 2017.

[103] A. H. Zahmani, A. Nishijima, Y. Morimoto, H. Wang, J.-F. Li, and A. Sandhu, "Temperature dependence of the resistance of AlGaN/GaN heterostructures and their applications as temperature sensors," *Japanese Journal of Applied Physics*, vol. 49, no. 4S, p. 04DF14, 2010.

[104] O. Ambacher, J. Smart, J. Shealy, N. Weimann, K. Chu, M. Murphy, W. Schaff, L. Eastman, R. Dimitrov, L. Wittmer *et al.*, "Two-dimensional electron gases induced by spontaneous and piezoelectric polarization charges in N-and Ga-face AlGaN/GaN heterostructures," *Journal of applied physics*, vol. 85, no. 6, pp. 3222–3233, 1999.

[105] J. R. Hook and H. E. Hall, *Solid State Physics*, 2nd ed. London: John Wiley & Sons, 1991.

[106] J. Schalwig, G. Müller, U. Karrer, M. Eickhoff, O. Ambacher, M. Stutzmann, L. Görgens, and G. Dollinger, "Hydrogen response mechanism of Pt–GaN schottky diodes," *Applied Physics Letters*, vol. 80, no. 7, pp. 1222–1224, 2002.

[107] J. Schalwig, G. Müller, M. Eickhoff, O. Ambacher, and M. Stutzmann, "Group III-nitride-based gas sensors for combustion monitoring," *Materials Science and Engineering: B*, vol. 93, no. 1-3, pp. 207–214, 2002.

[108] ——, "Gas sensitive GaN/AlGaN-heterostructures," *Sensors and Actuators B: Chemical*, vol. 87, no. 3, pp. 425–430, 2002.

[109] M. Stutzmann, G. Steinhoff, M. Eickhoff, O. Ambacher, C. Nebel, J. Schalwig, R. Neuberger, and G. Müller, "GaN-based heterostructures

for sensor applications," *Diamond and related materials*, vol. 11, no. 3-6, pp. 886–891, 2002.

[110] Z. Yang, R. Wang, D. Wang, B. Zhang, K. Lau, and K. Chen, "GaN-on-patterned-silicon (GPS) technique for fabrication of GaN-based MEMS," *Sensors and Actuators A: Physical*, vol. 130, pp. 371–378,.

[111] J. Lv, Z. Yang, G. Yan, W. Lin, Y. Cai, B. Zhang, and K. Chen, "Fabrication of large-area suspended MEMS structures using GaN-on-Si platform," *IEEE electron device letters*, vol. 30, pp. 1045–1047,.

[112] D. Zhuang and J. Edgar, "Wet etching of GaN, AlN, and SiC: a review," *Materials Science and Engineering: R: Reports*, vol. 48, no. 1, pp. 1–46, 2005.

[113] C.-H. Li, Y.-C. Jiang, H.-C. Tsai, Y.-N. Zhong, and Y. ming Hsin, "Device characteristics of AlGaN/GaN HEMTs with p-GaN cap layer," *ECS Journal of Solid State Science and Technology*, vol. 6, no. 11, pp. S3125–S3128, 2017. [Online]. Available: https://doi.org/10.1149/2.0281711jss

[114] M. Stutzmann, G. Steinhoff, M. Eickhoff, O. Ambacher, C. Nebel, J. Schalwig, R. Neuberger, and G. Müller, "GaN-based heterostructures for sensor applications," *Diamond and related materials*, vol. 11, pp. 886–891,.

[115] K. Kaasbjerg, K. S. Thygesen, and A.-P. Jauho, "Acoustic phonon limited mobility in two-dimensional semiconductors: Deformation potential and piezoelectric scattering in monolayer MoS 2 from first principles," *Physical Review B*, vol. 87, no. 23, p. 235312, 2013.

[116] L. Hsu and W. Walukiewicz, "Electron mobility in $Al_xGa_{1-x}N$/GaN heterostructures," *Physical Review B*, vol. 56, no. 3, p. 1520, 1997.

[117] S. Lisesivdin, A. Yildiz, N. Balkan, M. Kasap, S. Ozcelik, and E. Ozbay, "Scattering analysis of two-dimensional electrons in AlGaN/GaN with

bulk related parameters extracted by simple parallel conduction extraction method," *Journal of Applied Physics*, vol. 108, no. 1, p. 013712, 2010.

[118] B. Shen, T. Someya, and Y. Arakawa, "Influence of strain relaxation of the Al $_x$ Ga $_{1-x}$ N barrier on transport properties of the two-dimensional electron gas in modulation-doped Al_x Ga $_{1-x}$ N/GaN heterostructures," *Applied Physics Letters*, vol. 76, no. 19, pp. 2746–2748, 2000.

[119] I. Smorchkova, C. Elsass, J. Ibbetson, R. Vetury, B. Heying, P. Fini, E. Haus, S. DenBaars, J. Speck, and U. Mishra, "Polarization-induced charge and electron mobility in AlGaN/GaN heterostructures grown by plasma-assisted molecular-beam epitaxy," *Journal of applied physics*, vol. 86, no. 8, pp. 4520–4526, 1999.

[120] M. Horita and J. Suda, "Characterization of lightly-doped n-and p-type homoepitaxial GaN on free-standing substrates," in *2017 IEEE International Meeting for Future of Electron Devices, Kansai (IMFEDK)*, 2017, pp. 86–87.

[121] N. Maeda, K. Tsubaki, T. Saitoh, and N. Kobayashi, "High-temperature electron transport properties in AlGaN/GaN heterostructures," *Applied Physics Letters*, vol. 79, no. 11, pp. 1634–1636, 2001.

[122] M. Shur, B. Gelmont, and M. A. Khan, "Electron mobility in two-dimensional electron gas in AIGaN/GaN heterostructures and in bulk GaN," *Journal of electronic materials*, vol. 25, no. 5, pp. 777–785, 1996.

[123] B. Kang, H. Wang, F. Ren, B. Gila, C. Abernathy, S. Pearton, J. Johnson, P. Rajagopal, J. Roberts, E. Piner *et al.*, "pH sensor using AlGaN/GaN high electron mobility transistors with Sc_2 O_3 in the gate region," *Applied physics letters*, vol. 91, no. 1, p. 012110, 2007.

[124] Y. Dong, D.-h. Son, Q. Dai, J.-H. Lee, C.-H. Won, J.-G. Kim, S.-H. Kang, J.-H. Lee, D. Chen, H. Lu *et al.*, "AlGaN/GaN heterostructure pH sensor with multi-sensing segments," *Sensors and Actuators B: Chemical*, vol. 260, pp. 134–139, 2018.

[125] C.-T. Lee, Y.-S. Chiu, and X.-Q. Wang, "Performance enhancement mechanisms of passivated InN/GaN-heterostructured ion-selective field-effect-transistor pH sensors," *Sensors and Actuators B: Chemical*, vol. 181, pp. 810–815, 2013.

[126] M. S. Z. Abidin, A. M. Hashim, M. E. Sharifabad, S. F. A. Rahman, and T. Sadoh, "Open-gated pH sensor fabricated on an undoped-AlGaN/GaN hemt structure," *Sensors*, vol. 11, no. 3, pp. 3067–3077, 2011.

[127] B. H. Chu, B. Kang, C. Chang, F. Ren, A. Goh, A. Sciullo, W. Wu, J. Lin, B. Gila, S. J. Pearton *et al.*, "Wireless detection system for glucose and pH sensing in exhaled breath condensate using AlGaN/GaN high electron mobility transistors," *IEEE Sensors Journal*, vol. 10, no. 1, pp. 64–70, 2009.

[128] G. K. Kouassi, J. Irudayaraj, and G. McCarty, "Activity of glucose oxidase functionalized onto magnetic nanoparticles," *Biomagnetic research and technology*, vol. 3, no. 1, pp. 1–10, 2005.

[129] S. Pearton, B. Kang, S. Kim, F. Ren, B. Gila, C. Abernathy, J. Lin, and S. Chu, "GaN-based diodes and transistors for chemical, gas, biological and pressure sensing," *Journal of Physics: Condensed Matter*, vol. 16, pp. 961,.

[130] Y. Alifragis, A. Volosirakis, N. Chaniotakis, G. Konstantinidis, E. Iliopoulos, and A. Georgakilas, "AlGaN/GaN high electron mobility transistor sensor sensitive to ammonium ions," *physica status solidi (a)*, vol. 204, no. 6, pp. 2059–2063, 2007.

[131] H.-T. Wang, B. Kang, T. Chancellor Jr, T. Lele, Y. Tseng, F. Ren, S. Pearton, W. Johnson, P. Rajagopal, J. Roberts *et al.*, "Fast electrical detection of Hg (II) ions with AlGaN/GaN high electron mobility transistors," *Applied Physics Letters*, vol. 91, no. 4, p. 042114, 2007.

[132] B. Kang, H. Wang, F. Ren, and S. Pearton, "Electrical detection of biomaterials using AlGaN/GaN high electron mobility transistors," *Journal of applied physics*, vol. 104, no. 3, p. 8, 2008.

[133] B. Kang, H. Wang, T. Lele, Y. Tseng, F. Ren, S. Pearton, J. Johnson, P. Rajagopal, J. Roberts, E. Piner *et al.*, “Prostate specific antigen detection using al ga n/ ga n high electron mobility transistors,” *Applied physics letters*, vol. 91, no. 11, p. 112106, 2007.

[134] J.-d. Li, J.-j. Cheng, B. Miao, X.-w. Wei, J. Xie, J.-c. Zhang, Z.-q. Zhang, and D.-m. Wu, “Detection of prostate-specific antigen with biomolecule-gated AlGaN/GaN high electron mobility transistors,” *Journal of Micromechanics and Microengineering*, vol. 24, no. 7, p. 075023, 2014.

[135] S. Yang, L. Gu, X. Ding, B. Miao, Z. Gu, L. Yang, J. Li, and D. Wu, “Disposable gate AlGaN/GaN high-electron-mobility sensor for trace-level biological detection,” *IEEE Electron Device Letters*, vol. 39, no. 10, pp. 1592–1595, 2018.

[136] H. Wang, B. Kang, F. Ren, S. Pearton, J. Johnson, P. Rajagopal, J. Roberts, E. Piner, and K. Linthicum, “Electrical detection of kidney injury molecule-1 with AlGaN/GaN high electron mobility transistors,” *Applied Physics Letters*, vol. 91, no. 22, p. 222101, 2007.

[137] K. Chen, B. Kang, H. Wang, T. Lele, F. Ren, Y. Wang, C. Chang, S. Pearton, D. Dennis, J. Johnson *et al.*, “C-erbB-2 sensing using AlGaN/GaN high electron mobility transistors for breast cancer detection,” *Applied physics letters*, vol. 92, no. 19, p. 192103, 2008.

[138] G. Steinhoff, M. Hermann, W. Schaff, L. Eastman, M. Stutzmann, and M. Eickhoff, “pH response of GaN surfaces and its application for pH-sensitive field-effect transistors,” *Applied Physics Letters*, vol. 83, no. 1, pp. 177–179, 2003.

[139] M. Hou, A. Suria, A. Yalamarthy, H. So, and D. Senesky, “2DEG-heated AlGaN/GaN micro-hotplates for high-temperature chemical sensing microsystems,” in *Proc. Solid-State Sens. Actuators Microsyst. Workshop*, 2016, pp. 356–359.

[140] J. Jakovenko, T. Lalinsky, M. Drzik, M. Ivanova, G. Vanko, and M. Husak, “GaN, GaAs and silicon based micromechanical free standing hot plates for gas sensors,” *Procedia Chemistry*, vol. 1, pp. 804–807,.

[141] T. Boles, “GaN-on-silicon–present capabilities and future directions,” in *AIP Conference Proceedings*, vol. 1934, no. 1. AIP Publishing LLC, 2018, p. 020001.

[142] H. Lu, P. Sandvik, A. Vertiatchikh, J. Tucker, and A. Elasser, “High temperature hall effect sensors based on AlGaN/GaN heterojunctions,” *Journal of applied physics*, vol. 99, pp. 114 510,.

[143] T. Yamamura, D. Nakamura, M. Higashiwaki, T. Matsui, and A. Sandhu, “High sensitivity and quantitative magnetic field measurements at 600°C,” *Journal of applied physics*, vol. 99, pp. 08 302,.

[144] A. Abderrahmane, S. Koide, S.-I. Sato, T. Ohshima, A. Sandhu, and H. Okada, “Robust hall effect magnetic field sensors for operation at high temperatures and in harsh radiation environments,” *IEEE Transactions on Magnetics*, vol. 48, pp. 4421–4423,.

[145] L. Bouguen, S. Contreras, B. Jouault, L. Konczewicz, J. Camassel, Y. Cordier, M. Azize, S. Chenot, and N. Baron, “Investigation of AlGaN/AlN/GaN heterostructures for magnetic sensor application from liquid helium temperature to 300° c,” *Applied Physics Letters*, vol. 92, pp. 043 504,.

[146] B. Kang, J. Kim, S. Jang, F. Ren, J. Johnson, R. Therrien, P. Rajagopal, J. Roberts, E. Piner, and K. Linthicum, “Capacitance pressure sensor based on GaN high-electron-mobility transistor-on-Si membrane,” *Applied Physics Letters*, vol. 86, pp. 253 502,.

[147] “Stress investigation of the AlGaN/GaN micromachined circular diaphragms of a pressure sensor,” *Journal of Micromechanics and Microengineering*, vol. 25, pp. 015 001,.

[148] “AlGaN/GaN diaphragm-based pressure sensor with direct high performance piezoelectric transduction mechanism,” *Applied Physics Letters*, vol. 107, pp. 122 102,.

[149] A. Talukdar, M. Khan, D. Lee, S. Kim, T. Thundat, and G. Koley,

"Piezotransistive transduction of femtoscale displacement for photoacoustic spectroscopy," *Nature communications*, vol. 6.

[150] S. Hung, B. Chou, C. Chang, C. Lo, K. Chen, Y.-L. Wang, S. Pearton, A. Dabiran, P. Chow, and G. Chi, "Minipressure sensor using AlGaN/GaN high electron mobility transistors," *Applied Physics Letters*, vol. 94, pp. 043 903,.

[151] C. Chapin, R. Miller, K. Dowling, R. Chen, and D. Senesky, "InAlN/GaN high electron mobility micro-pressure sensors for high-temperature environments," *Sensors and Actuators A: Physical*.

[152] "AlGaN/GaN C-HEMT structures for dynamic stress detection," *Sensors and Actuators A: Physical*, vol. 172, pp. 98–102,.

[153] A. Zahmani, A. Nishijima, Y. Morimoto, H. Wang, J.-F. Li, and A. Sandhu, "Temperature dependence of the resistance of AlGaN/GaN heterostructures and their applications as temperature sensors," *Japanese Journal of Applied Physics*, vol. 49, pp. 04 14,.

[154] A. Kwan, Y. Guan, X. Liu, and K. Chen, "Integrated over-temperature protection circuit for GaN smart power ICs," *Japanese Journal of Applied Physics*, vol. 52, pp. 08 15,.

[155] H. Chiamori, M. Hou, C. Chapin, A. Shankar, and D. Senesky, "Characterization of gallium nitride microsystems within radiation and high-temperature environments," *SPIE MOEMS-MEMS*, p. 897507–897507–8.

[156] A. Kwan, Y. Guan, X. Liu, and K. Chen, "A highly linear integrated temperature sensor on a GaN smart power IC platform," *Electron Devices, IEEE Transactions on*, vol. 61, pp. 2970–2976,.

[157] Y.-H. Chang, Y.-S. Lu, Y.-L. Hong, S. Gwo, and J. Yeh, "Highly sensitive pH sensing using an indium nitride ion-sensitive field-effect transistor," *IEEE Sensors Journal*, vol. 11, pp. 1157–1161,.

[158] C.-T. Lee, Y.-S. Chiu, and X.-Q. Wang, "Performance enhancement mechanisms of passivated InN/GaN-heterostructured ion-selective field-effect-transistor pH sensors," *Sensors and Actuators B: Chemical*, vol. 181, pp. 810–815,.

[159] Y. Irokawa, "Hydrogen sensors using nitride-based semiconductor diodes: the role of metal/semiconductor interfaces," *Sensors*, vol. 11, pp. 674–695,.

[160] J. Song, W. Lu, J. Flynn, and G. Brandes, "AlGaN/GaN Schottky diode hydrogen sensor performance at high temperatures with different catalytic metals," *Solid-state Electronics*, vol. 49, pp. 1330–1334,.

[161] P. Offermans, A. Si-Ali, G. Brom-Verheyden, K. Geens, S. Lenci, M. Hove, S. Decoutere, and R. Schaijk, "Suspended AlGaN/GaN membrane devices with recessed open gate areas for ultra-low-power air quality monitoring," in *Electron Devices Meeting (IEDM), 2015.* IEEE International, p. 33 6 1–33 6 4.

[162] I. Jahangir, E. Quddus, and G. Koley, "Unique detection of organic vapors below their auto-ignition temperature using III–V Nitride based triangular microcantilever heater," *Sensors and Actuators B: Chemical*, vol. 222, pp. 459–467,.

[163] I. Jahangir and G. Koley, "Dual-channel microcantilever heaters for volatile organic compound detection and mixture analysis," *Scientific reports*, vol. 6.

[164] B. Chu, B. Kang, C. Chang, F. Ren, A. Goh, A. Sciullo, W. Wu, J. Lin, B. Gila, and S. Pearton, "Wireless detection system for glucose and pH sensing in exhaled breath condensate using AlGaN/GaN high electron mobility transistors," *IEEE Sensors Journal*, vol. 10, pp. 64–70,.

[165] N. Sabaté, J. Santander, L. Fonseca, I. Gràcia, and C. Cané, "Multi-range silicon micromachined flow sensor," *Sensors and Actuators A: Physical*, vol. 110, no. 1-3, pp. 282–288, 2004.

[166] R. J. Adamec and D. V. Thiel, "Self heated thermo-resistive element hot wire anemometer," *IEEE Sensors Journal*, vol. 10, no. 4, pp. 847–848, 2010.

[167] E. Meng, P.-Y. Li, and Y.-C. Tai, "A biocompatible parylene thermal flow sensing array," *Sensors and Actuators A: Physical*, vol. 144, no. 1, pp. 18–28, 2008.

[168] N. Nguyen and W. Dötzel, "Asymmetrical locations of heaters and sensors relative to each other using heater arrays: A novel method for designing multi-range electrocaloric mass-flow sensors," *Sensors and Actuators A: physical*, vol. 62, no. 1-3, pp. 506–512, 1997.

[169] M. Domínguez, V. Jiménez, J. Ricart, L. Kowalski, J. Torres, S. Navarro, J. Romeral, and L. Castañer, "A hot film anemometer for the martian atmosphere," *Planetary and Space Science*, vol. 56, no. 8, pp. 1169–1179, 2008.

[170] R. Ahrens and K. Schlote-Holubek, "A micro flow sensor from a polymer for gases and liquids," *Journal of Micromechanics and Microengineering*, vol. 19, no. 7, p. 074006, 2009.

[171] S.-T. Hung, S.-C. Wong, and W. Fang, "The development and application of microthermal sensors with a mesh-membrane supporting structure," *Sensors and Actuators A: Physical*, vol. 84, no. 1-2, pp. 70–75, 2000.

[172] A. S. Cubukcu, E. Zernickel, U. Buerklin, and G. A. Urban, "A 2d thermal flow sensor with sub-mw power consumption," *Sensors and Actuators A: Physical*, vol. 163, no. 2, pp. 449–456, 2010.

[173] P. Fürjes, G. Légrádi, C. Dücső, A. Aszódi, and I. Bársony, "Thermal characterisation of a direction dependent flow sensor," *Sensors and Actuators A: Physical*, vol. 115, no. 2-3, pp. 417–423, 2004.

[174] V. Lekholm, A. Persson, K. Palmer, F. Ericson, and G. Thornell, "High-temperature zirconia microthruster with an integrated flow sen-

sor," *Journal of Micromechanics and Microengineering*, vol. 23, no. 5, p. 055004, 2013.

[175] A. Mahdavifar, R. Aguilar, Z. Peng, P. J. Hesketh, M. Findlay, J. R. Stetter, and G. W. Hunter, "Simulation and fabrication of an ultra-low power miniature microbridge thermal conductivity gas sensor," *Journal of The Electrochemical Society*, vol. 161, no. 4, p. B55, 2014.

[176] P. Bruschi, A. Diligenti, D. Navarrini, and M. Piotto, "A double heater integrated gas flow sensor with thermal feedback," *Sensors and Actuators A: Physical*, vol. 123, pp. 210–215, 2005.

[177] A. De Luca, G. Longobardi, and F. Udrea, "Soi multidirectional thermoelectric flow sensor for harsh environment applications," in *2015 International Semiconductor Conference (CAS)*. IEEE, 2015, pp. 95–98.

[178] J. Laconte, C. Dupont, D. Flandre, and J.-P. Raskin, "Soi cmos compatible low-power microheater optimization for the fabrication of smart gas sensors," *IEEE Sensors Journal*, vol. 4, no. 5, pp. 670–680, 2004.

[179] A. De Luca and F. Udrea, "CMOS MEMS hot-film thermoelectronic flow sensor," *IEEE sensors letters*, vol. 1, no. 6, pp. 1–4, 2017.

[180] D. F. Reyes Romero, K. Kogan, A. S. Cubukcu, and G. A. Urban, "Simultaneous flow and thermal conductivity measurement of gases utilizing a calorimetric flow sensor," *Sensors and Actuators A: Physical*, vol. 203, pp. 225–233, 2013. [Online]. Available: https://www.sciencedirect.com/science/article/pii/S0924424713004093

[181] I. T. Jolliffe, "A note on the use of principal components in regression," *Journal of the Royal Statistical Society: Series C (Applied Statistics)*, vol. 31, no. 3, pp. 300–303, 1982.

[182] M. Tipping and C. Bishop, "Mixtures of probabilistic principal component analysers," *Neural Computation*, vol. 11, no. 2, pp. 443–482, Feb. 1999, copyright of the Massachusetts Institute of Technology Press (MIT Press).

[183] K. S. Ng, "A simple explanation of partial least squares," 2013.

[184] I. Jolliffe and Springer-Verlag, *Principal Component Analysis*, ser. Springer Series in Statistics. Springer, 2002. [Online]. Available: https://books.google.co.uk/books?id=_olByCrhjwIC

[185] T. Aguilera, J. Lozano, J. A. Paredes, F. J. Alvarez, and J. I. Suárez, "Electronic nose based on independent component analysis combined with partial least squares and artificial neural networks for wine prediction," *Sensors*, vol. 12, no. 6, pp. 8055–8072, 2012.

[186] F. Lindgren, P. Geladi, and S. Wold, "The kernel algorithm for PLS," *Journal of Chemometrics*, vol. 7, no. 1, pp. 45–59, 1993.

[187] P. Geladi and B. R. Kowalski, "Partial least-squares regression: a tutorial," *Analytica chimica acta*, vol. 185, pp. 1–17, 1986.

[188] W. P. Carey and S. S. Yee, "Calibration of nonlinear solid-state sensor arrays using multivariate regression techniques," *Sensors and Actuators B: Chemical*, vol. 9, no. 2, pp. 113–122, 1992.

[189] X. Wang, W. P. Carey, and S. S. Yee, "Monolithic thin-film metal-oxide gas-sensor arrays with application to monitoring of organic vapors," *Sensors and Actuators B: Chemical*, vol. 28, no. 1, pp. 63–70, 1995.

[190] A. Hierlemann, U. Weimar, G. Kraus, M. Schweizer-Berberich, and W. Göpel, "Polymer-based sensor arrays and multicomponent analysis for the detection of hazardous oragnic vapours in the environment," *Sensors and Actuators B: Chemical*, vol. 26, no. 1-3, pp. 126–134, 1995.

[191] E. L. Gardner, T. A. Vincent, A. De Luca, and F. Udrea, "Simultaneous flow and thermal conductivity sensing on a single chip using artificial neural networks," *IEEE Sensors Journal*, vol. 20, no. 9, pp. 4985–4991, 2020.